RESONANT OPTICAL TUNNELING EFFECT FOR REFRACTIVE INDEX SENSOR APPLICATIONS

JIAN AOQUN

Ph.D

The Hong Kong Polytechnic University

2013

The Hong Kong Polytechnic University
Department of Applied Physics

Resonant Optical Tunneling Effect for Refractive Index Sensor Applications

JIAN Aoqun

A thesis submitted in partial fulfillment of the requirements

for the degree of Doctor of Philosophy

June 2012

CERTIFICATE OF ORIGINALITY

I hereby declare that this thesis is my own work and that, to the best of my knowledge and belief, it reproduces no material previously published or written, nor material that has been accepted for the award of any other degree or diploma, except where due acknowledgement has been made in the text.

_____ (Signed)

Jian Aoqun (Name of student)

Abstract

This doctoral study focuses on the theoretical analysis of resonant optical tunneling effect (ROTE) and its potential application for ultrahigh-sensitivity refractive index sensing. More specifically, detailed studies have been conducted on the physical principles from the optics and quantum origins, two sensor device designs using the microfluidic chip and the angled fibers, the analyses of the structural parameters and performance, and the experimental results of the fabricated angled-fiber-based sensor.

In the theoretical study of this work, the physical mechanism of the ROTE is examined from two origins – nano-optics interpretation and quantum mechanism interpretation. Correspondingly, two theoretical models – the transfer matrix model (TMM) and the potential barrier model (PBM) are developed. In this study, the equivalence of the two models is first tested using simple tunneling structures (2 and 3 layers). It is found that they give almost identical results in computing the transmission and reflection properties. For more complicated structures like the 5-layer ROTE structure, the two models share the same period and overlap well after a shift to compensate the phase difference. Through detailed studies of the two models,

it is found that TMM is more convenient for simple structures whereas PBM works better for complicated structures.

In the sensor design, two types of ROTE refractometers have been proposed. One utilizes microfluidic chip and the other makes use of a pair of angled optical fibers. Theoretical study shows that the microfluidic chip design has extremely sharp transmission peak and achieves a detectivity of 85,000 RIU^{-1} about two orders of magnitude higher than the widely-used Fabry–Pérot (FP) etalons and the surface plasmon resonance (SPR) sensors. In case of the angled fiber-based design, the simulation results show that the intensity-based method could reach a detection limit of 10^{-7} RIU and the spectrum-based method promises a sensitivity of 81,000 nm/RIU, which are about 10 times larger than the SPR sensors and over 180 times larger than the FP etalons. As the FP and SPR sensors have already demonstrated a detection limit of 10^{-4} – 10^{-7} RIU, it is reasonable to expect the ROTE sensor offers a detection limit up to 10^{-6} – 10^{-9} RIU.

In the experimental studies, the angled fiber-based design is adopted due to its simple structure and easy implementation. For comparison, the refractive index sensor based on SPR effect has also been fabricated and obtained a sensitivity of

7,650 nm/RIU. As to the ROTE sensor, the ROTE sensor exhibits a series of peaks in the transmission spectrum. When the polarization state of the incident light is adjusted between the two polarization states, the intensity and position of the transmission peak can be varied significantly, agreeing well with the theoretical predictions. By slightly changing the fiber separation and then monitoring the peak wavelength shift, the sensor achieves an equivalent sensitivity of 3,500 nm/RIU.

This work is probably the first systematic study on the physics mechanism of the ROTE. The investigations based on both the nano-optics and the quantum mechanics interpretation not only bring deep insight into the physical understandings of the ROTE, but also reveal an interesting analogy between two distinct fields—optics and quantum theory. This work is also the first attempt to apply the ROTE for sensing applications. Particularly, the experimental studies, though far from perfect, have well demonstrated the great potential of the ROTE sensors in ultrahigh sensitive detection of refractive index. Equipped with such a new working principle, the ROTE sensors may find broad applications in biochemical analysis, food safety and water quality monitoring.

List of Publications

Journal papers

1. **Aoqun Jian** and Xuming Zhang, Resonant optical tunneling effect: recent progress in modeling and applications, *IEEE Journal of Selected Topics on Quantum Electronics*, (invited review, in press).
2. **Aoqun Jian**, Kai Zhang, Yu Wang, Shu Ping Lau, Yuen Hong Tsang, and Xuming Zhang, Microfluidic flow direction control using continuous-wave laser, *Sensors and Actuators A: Physical*, 188, 329-334 (2012).
3. **Aoqun Jian**, Xuming Zhang, Weiming Zhu and Aiqun Liu, Liquid refractive index sensors using resonant optical tunneling effect for ultra-high sensitivity, *Sensors and Actuators A: Physical*, 169(2), 347-351 (2011).
4. Kai Zhang, **Aoqun Jian**, Xuming Zhang, Yu Wang, Zhaohui Li, and Hwa-Yaw Tam, Laser-induced thermal bubbles for microfluidic applications, *Lab on a Chip*, 11, 1389 (2011).
5. **Aoqun Jian**, Xuming Zhang, Weiming Zhu, and Miao Yu, Optofluidic refractometer using resonant optical tunneling effect, *Biomicrofluidics*, 4, 043008 (2010).

Conference papers

1. **Aoqun Jian**, Ning Wang, Kai Zhang, Yu Wang, Yuen Hung Tsang and Xuming Zhang, Optofluidic manipulation using continuous-wave laser, *The 1st International Conference on Optofluidics (Optofluidics 2011)*, Xi'an, China, December 2011.
2. **Aoqun Jian**, Ning Wang, and Xuming Zhang, Micro-bubble generation using continuous-wave laser, *International Conference on Materials for Advanced Technologies (ICMAT) 2011*, Singapore, June 2011.
3. **Aoqun Jian**, Kai Zhang, Yu Wang, and Xuming Zhang, Laser induced micro-valves and micro-pumps, *The 16th International conference on solid state physics, actuators, and microsystems* (*Transducers 2011)*, Beijing, China, June 2011.
4. **Aoqun Jian**, Miao Yu and Xuming Zhang, Resonant optical tunneling effect for sensing applications, *The 6th International Conference on Nanophotonics (ICNP 2012)*, Beijing, China, May 2012.
5. Xuming Zhang, **Aoqun Jian**, Weiming Zhu, and Aiqun Liu, Microfluidic double optical barrier structure for liquid refractive index sensors with ultra-high sensitivity, *the 5th Asia-Pacific Conference on Transducers and Micro-Nano technology (APCOT 2010)*, Perth, Australia, July 2010.
6. Xuming Zhang, **Aoqun Jian**, Weiming Zhu, and Aiqun Liu, Liquid refractive index sensors using resonant optical tunneling effect, *The 2nd Asia-Pacific Optical Sensors Conference (APOS2010)*, Guangzhou, China, June 2010.

Academic award

1. Best Paper Award, The 1st International Conference on Optofluidics (Optofluidics 2011), December 2011, Xi'an, China, paper title: *Optofluidic manipulation using continuous-wave laser*, authors: **Aoqun Jian**, Ning Wang, Kai Zhang, Yu Wang, Yuen Hung Tsang and Xuming Zhang.

Acknowledgments

I am indebted to many individuals who have provided assistance and support during the period of this research. First and foremost, I would like especially to convey my appreciations to my supervisor, Dr. Zhang Xuming for all his valuable help and constant guidance throughout the period of my research. His advice and encouragements continuously inspire me to improve my research abilities in many aspects, and will be a precious treasure for my whole life.

I would also like to appreciate my co-supervisor Prof. S. P. Lau for his helpful guidance and discussions on my research and thesis, and express my appreciation to the academic members in our department: Prof. S. F. Yu, Dr. J. Y. Dai, Dr. J. H. Hao, Dr. F. Yan, Dr. Tsang, and Dr. Y. Wang for their insightful suggestions during my research.

Many thanks convey to Prof. Miao Yu of University of Maryland, College Park. Her strong support and valuable suggestions have been of great help to me. The completion of this PhD study would be impossible without her generous help in various aspects.

I would like to acknowledge the collaboration with Prof. Hwa-Yaw Tam Department of Electrical Engineering at The Hong Kong Polytechnic University, Dr. Zhaohui Li from Institute of Photonics Technology at Jinan University, Dr. Weiming Zhu and Prof. Ai-Qun Liu from School of Electrical and Electronic Engineering, Nanyang Technological University. They gave me useful assistance in experiments during the collaboration.

I wish to thank my colleagues and friends, Dr. Kai Zhang, Mr. Feng Cao, Mr. Tong Wei, Mr. Zhengjiang Shen, Mr. Han Wang, Mr. S.T.F. Lee, Dr. Lei Lei, Mr. Cheng Pang, Mr. Hyungdae Bae, Dr. Yuxiang Liu, Dr. Haijun Liu, Mr. Felix Steif, Dr. Ming Feng and Dr. Zhiqing Feng. We had wonderful time together.

Finally, this thesis is dedicated to my family for their unconditional support, patience and encouragement throughout the duration of this thesis.

Table of Contents

Chapter 5 Experimental Investigation and Results

Chapter 6 Conclusions and Future Work

List of Figures

List of Tables

Chapter 1 Introduction

1.1 Background

In optics, the index of refraction (n) is the ratio of the speed of light in a vacuum (c) to the speed of light in the medium (v): $n = c / v$. As refractive index (RI) of materials depends on the wavelength of transmission light, the typical RI values are measured at the yellow doublet sodium D-line (589nm). Generally speaking, most transparent media (solids and liquids) have refractive indices between 1.3 and 1.7.

As a fundamental physical property of a substance, the RI is well known for confirming the purity and measuring the concentration of specific solute in the transparent solvent, such as the concentrations of sugar (Brix) and salt (Salinity). Because light does not usually influence chemical reactions, the RI measurement will not actually affect the properties of the analyst compared with other testing methods and could provide a real-time and convenient diagnostic indication of the composition of solutions.

Moreover, recent research reveals that accurate measurement of RI of liquid samples is of great importance to many industrial processes and research studies. [1] The ultrahigh sensitivity promises a reliable and quantitative method to monitor the tiny change of the chemical constituents (e.g., 10^{-9} RIU corresponds to approximately 1 femto mol/L of salt in water), and thus more accurate variations in the chemical composition of the analyzed solutions could be detected. Furthermore, the RI of a live cell is a valuable parameter for quantifying cell physiology and pathology, certain molecules (e.g., DNAs, proteins) could be detected and traced by the variation of corresponding RI. [2, 3] This is particularly useful for drug screening and biomedical studies since the cells and other bio-particles could be monitored in real time and in their natural living states, without the need for any biochemical marking, labeling, immobilizing, amplifying or culturing processes. [3, 4] Therefore, the refractometry with ultrahigh sensitivity has great potential applications in the areas of environment protection, drinking water safety and biomedical discoveries.

Most commercial refractometers available nowadays stem from the Abbé refractometer, which is based on the total internal reflection phenomenon. The detection limit of portable handheld refractometers could reach 10^{-4} RIU. In case of

some bench-top analysis instruments, the detection limits are normally from 10^{-4} to 10^{-5} RIU. [5] For most liquid samples, the RI range is usually from 1.33 to 1.52 RIU. Besides the Abbé refractometer, many other refractometers have been developed and implemented. Most of them are based on the refraction, interference and near-field effects of light. And the detection limits of these novel refractometers are around 10^{-6} to recently 10^{-7} RIU. [6-70] However, because of the inevitable constraints of these physical mechanisms, 10^{-7} RIU has become a formidable barrier to the detection limit and none of the available methods could go beyond it. [12, 28, 64] To break the barrier, new physical effects should be explored for the sensor application. [71-84]

On the other hand, a physical mechanism, resonant optical tunneling effect (ROTE) may provide a feasible way to break the current sensitivity barrier. In 1988, the ROTE was first proposed by Pochi Yeh [85], and some other research [86-88] revealed that the ROTE has some unique advantages for the device applications. In 1999, Hayashi et al. first demonstrated the resonant optical tunneling (resonant photon tunneling) in experiment. [89] In 2004, Yamamoto et al. exploited the ROTE for optical switches. However, the great potential of the ROTE for the RI sensing applications has not been realized until this work. [90, 91]

1.2 Objectives of research

The aim of this work, which is to explore the ROTE for the RI sensors, covering both the theoretical analyses and experimental studies. Although the ROTE has already been investigated in literature, the theories of ROTE have not been well developed. The traditional approach to investigate the effect belongs mostly to the nano-optics interpretation, which is based on the Maxwell equations. Similar with the resonant tunneling of electrons, this effect can also be analyzed by the quantum mechanics interpretation, which is based on the Schrödinger equation. The quantum mechanics interpretation could deliver a better physical picture of the ROTE in more complicated structures. The equivalence and differences of these interpretations are the core part of the theoretical study of this PhD research.

Before experiments, two types of ROTE refractometers will be designed based on the microfluidic chip and the metal coated angled fiber, respectively. For each type, the performance analysis of sensor will be carried out.

The experimental study will be based on the angled fiber design due to the ease of fabrication and alignment. Important features of the ROTE will be examined,

and the RI sensitivity will be determined and compared with our own test of the surface plasmon resonance sensors.

In this thesis, the specific objectives of the project are:

- theoretical analysis of the ROTE using both the nano-optics interpretation and the quantum mechanics interpretation;
- sensor design based on the theoretical results and the investigation of sensing mechanism;
- experimental study of the RI sensors based on the ROTE and the surface plasmon resonance and comparison of their performances.

1.3 Outline of thesis

The chapters of this thesis are organized as follows:

Chapter 1 introduces the general background of refractometers and motivations of this work. It also includes the objectives and the outline of this thesis.

Chapter 2 reviews the RI sensors and the ROTE. In this chapter, the RI sensors based on different principles are presented in sequence. The results of theoretical study and the device applications of the ROTE are revealed.

Chapter 3 investigates the theory of the ROTE. The ROTE is analyzed in both nano-optics interpretation and quantum mechanics interpretation. And the results of these two methods are compared in the end of this chapter.

Chapter 4 presents the design and fabrication of RI sensors. In this chapter, an improved SPR sensors based on the tip reflection is designed firstly. Two types of ROTE sensor: microfluidic chip and metal coated angled fiber are proposed. The performances of sensors (sensitivities and detectivities) of the designed RI sensors are analyzed and compared.

Chapter 5 introduces the fabrication method of fiber sensors. The RI sensors based on the SPR and the ROTE are fabricated and tested, respectively, and the experimental results are presented and discussed.

Chapter 6 presents the conclusions of this thesis and proposes some suggestions for the future work.

Chapter 2 Overview of Refractive Index Sensors and Resonant Optical Tunneling Effect

In this chapter, we will review the evolution of RI sensing techniques. These sensors will be classified by their principles and will be presented in sequence. The principles and the representative sensitivities of these sensors will be listed in Table 2.1, and the advantages and limitations of each method will be discussed. In addition, the photon tunneling effect and the ROTE will be reviewed. The photon tunneling effect is the base of ROTE. And the ROTE review will cover its historic origin, theoretical studies and device applications.

2.1 Refractive index sensors

Over the years, many refractometries have been developed and the detection limit has been improved gradually from 10^{-2} to 10^{-7} refractive index unit (RIU). Whatever the physical principles are used for these sensors, the interaction between light and the solution of analytes (liquid sample) is fundamentally required. The sensitivity of

device is determined by the degree of liquid-light interaction, which strongly relies on the working principles and actual designs of the sensors. According to the working principles, most available methods could be roughly classified into three categories: ray optics, wave optics and near-field optics (or equivalently, nano-optics).

2.1.1 Refractive index sensors based on ray optics

The ray optics methods make use of the ray nature of the light and usually rely on the refraction [6-8] and reflection [9] at the interface of the liquid sample and another reference medium. In this category, the Abbé refractometer is the first laboratory refractometer developed in late 19th century, and is still popular in commercial devices. The initial Abbé refractometer was developed based on the total internal reflection phenomenon as is shown in Fig. 2.1.

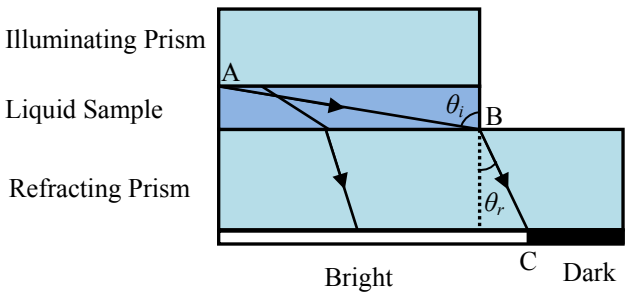

Fig. 2.1 Schematic diagram of the Abbé refractometer.

In operation, the liquid sample layer is sandwiched between an illuminating prism and a refracting prism. When a light beam is projected through the illuminating prism, the light rays are scattered to all directions at the bottom surface of the illuminating prism. According to the Snell's law,

$$n_1 \sin\theta_i = n_2 \sin\theta_r \tag{2.1}$$

Where $n_1$and n_2 is the RI of the incident and media, and θ_i and θ_r is incident angle and angle of refraction, respectively.

The light ray transmits between the two edges of prisms (denoted as line AB in Fig. 1.1) has the largest incident angle (θ_i), and hence the largest angle of refraction (θ_r). As a result, the refracted light all lies on the left side of C. Consequently, there are a bright region (left to C) and a dark region (right to C) on the bottom of the refracting prism. When the RI of liquid sample is changed, the angle of refraction will be varied at the same time. In this way, the change of RI could be obtained by scaling the position of borderline of the bright and dark regions. Over a century has passed, but its principle of operation has been seen very little change. Some modern Abbé refractometers use the digital display for the measurement and reach a detection limit of 10^{-5} RIU.

Besides the Abbé refractometers, there are many other refractometers based on the refraction. One is the differential refractometer proposed by Majer in 1976. [6] As shown in Fig. 2.2, the refractometer consisted of two prisms, and one of them was hollow and filled with sensing liquid. A ray of light passed through these two prisms and hit a photodetector in the distance away from the prisms. The position of light spot was recorded photoelectrically. When the RI of sensing liquid was changed a little, the light ray experienced a small deflection. Thus the difference of RI could be determined by the displacement of the laser spot caused by the refraction. The detection limit of the differential sensors reached typically 1×10^{-4} RIU, and could go to 1×10^{-5} RIU for full-scale reflection. [6] In the accurate characterizations, it is preferable to reduce the diameter of the laser beam so as to diminish the uncertainty of the measurement system. In 2004, Samedov introduced the beam profile alignment optics (BPAO) to get a pure Guassian beam [7]. He built the 3D profiles of a laser beam by charge-coupled device (CCD) beam profiler and used three trap detectors to get more signals. The Guassian profile was further sharpened by the knife-edge profiler technique and finally had a diameter of 321.2 mm. As a result, the uncertainty of the whole system could reach a minimum of 3×10^{-5} RIU,

which represents the highest level that kind of sensor could obtained.

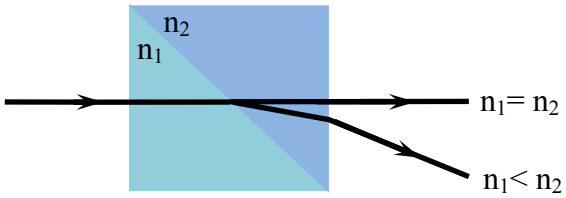

Fig. 2.2 Schematic diagram of the differential refractometer. [6]

The refractometers based on the ray optics, including both the Abbé refractometers and the differential refractometers, have their own advantages. Firstly, the sensors have simple structures and are thus easy to fabricate at low cost. Secondly, the sensors place no rigid requirements of the application environment and have broad commercial potential. However, to achieve a higher sensitivity, the optical signal detection components should have a higher spatial resolution, complicating the design of sensing systems. [7]

2.1.2 Refractive index sensors based on wave optics

The wave optics based methods exploit the wave nature of light and mainly measure the RI by diffraction [10], forward/backward scattering [11, 12] and various interference effects, such as Fabry-Pérot [13-15], Mach-Zehnder [16-19],

Michelson[20, 21], low coherence [22], fiber Bragg gratings [23, 24] and long-period grating [25]. In this category, the measurement is usually carried out in the far field (far greater than the wavelength).

In 2009, Sabatyan demonstrated the RI sensor based on Fresnal diffraction. [10] In this method, an optical fiber immersed in the liquid sample was perpendicular to the laser beam. The Fresnel diffraction pattern diffracted from the immersed fiber was collected by a set of CCD. Then the RI of liquid sample could be calculated by the fitting the normalized intensity distribution in least-square method.

Burggraf et al. illustrated the holographic RI detector by using the forward scattering. [11] A collimated, coherent light beam was divided by a holographic optical element into two coherent beams. One beam (probe beam) passed through the channel filled with the liquid sample, and the other (reference beam) penetrated the glass only. Then the two beams interfered in the far field. The generated interference pattern was detected by a photodiode array. A variation in the RI of the liquid sample would induce a phase change in the probe beam, thus a shift of the interference pattern. In 2002, Markov explored a similar idea using the backward scattering. [12] The detection limit of prototype-sensor could reach 10^{-7} RIU, which

represents the highest level of this category of RI sensors. They used a set of linear CCD array to capture the backscattering interference pattern and to trace the positions of multiple fringes pattern at the same time. This multiple point tracing method significantly improved the detection limit compared with the previous photoelectrical detection.

Fabry-Pérot (FP) interference is a simple interference model that many sensors are based on. The typical structure of FP etalon is shown in Fig. 2.3, which consists of two parallel, highly reflecting mirrors. The two mirrors are at a distance d from each other and have a reflectivity R. The wave is incident at the angle θ.

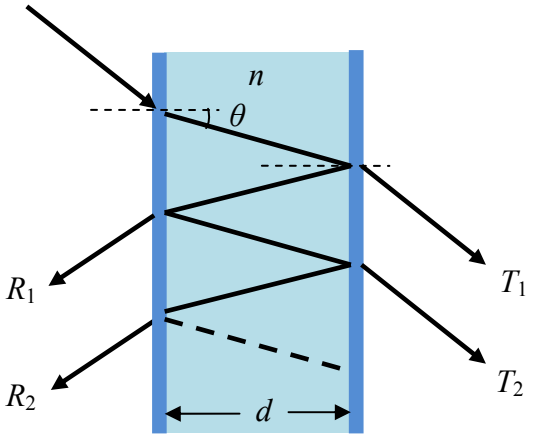

Fig. 2.3 Schematic diagram of the FP interferometer

Because these mirrors are partially reflecting, the incoming light beam is split into many individual components which interfere with each other. The phase

difference between each succeeding reflection is given by δ [39]:

$$\delta = (\frac{2\pi}{\lambda}) \ 2 \times n \times d \times \cos\theta \tag{2.2}$$

And the transmission $T = \frac{1}{1 + F\sin^2(\delta/2)}$, where $F = \frac{4R}{(1-R)^2}$ is the coefficient of fitness. Conventionally, there are a series of interference peaks in the transmission spectrum. For the RI sensors, if the RI of the medium in the cavity is changed, the interference spectrum will be varied, which means the interference peaks will be shifted correspondingly.

In bio-sensing applications there is a need to measure small RI changes in small volumes of liquid. However, size and weight of the traditional bulk refractometers make them not appropriate. A fiber based RI sensor can be very compact in size and be made suitable for remote sensing. On the other hand, ample processing methods on optical fibers and plenty of optical fiber components provide broad designing ideas for the RI sensors.

Liu's group of Nanyang Technological University has conducted a series of experiments to measure the RI of living cells using the optical-fiber-based FP interferometer. The first demonstration was carried out in 2006. [13] In this experiment, two aligned gold coated single mode fibers were aligned opposite to

each other, forming a FP cavity. A microfluidic chip was made to transport kidney cancer cells to the cavity. When the cell was captured in the cavity by a cell holder, the RI of cell could be measured. In the experiment, the kidney cancer cells measured an effective RI of 1.399 RIU at an accuracy of 0.1%. However, the cell holder caused some deformation of the cell, and thus the error in the experiment. As a result, they improved their work by using a pair of fiber Bragg gratings (FBG). [14] The high fitness FP cavity formed by FBG fibers could trap the cell optically and align it to the optical axis automatically. In addition, the detection limit of this design was 0.001 RIU better than the previous level of 0.002 RIU. In 2010, the same group further refined boosted their work using a light collimation mechanism. [15] The diverging light came from the optical fiber was collimated by a spherical curvature, and became less sensitive to the geometrical misalignment, providing better light manipulation and confinement. As a result, the finesse of the improved FP cavity was 18.79, and a sensitivity of 960 nm/RIU with a detection range of 0.043 RIU was achieved.

In addition to the FP interference, other type of interferences such as Mach-Zehnder interference [16-19] and Michelson interference [20] have also been utilized

fiber-based RI sensors. Take Tian's work for example (shown in Fig. 2.4) [16], the sensing element utilized two sharp tapers in the single mode fiber with a separation of several centimeters. The two tapers were immersed in the liquid sample for the RI sensing. In the first taper area some light energy in the core mode was coupled into the cladding mode. And in the second taper, the cladding mode can be coupled back into the core mode and interfered with the light that is always in the core. If the RI of the environment surrounding the single mode fiber is altered, the effective RI of the cladding mode is thus changed. As a result, the interference peak at the output side is shifted. The sensitivity of this sensor was 17 nm/RIU. In the same year, Tian also reported a similar sensor based on the Michelson interference. [20] In this design, the cladding mode produced by the taper was reflected by the gold coated fiber end, and went through the taper again. In order to raise the sensitivity, Zhu optimized the design by adding the third taper between the two tapers, and thus the interaction between the liquid sample and the cladding mode was increased. [17] Some researchers found that a single mode fiber sandwiched with a short section of multimode fiber also had the similar function with the taper. [19, 21] The mismatch of the core sizes of the single mode fiber and the multimode fiber provides similar

conversion between the core mode and the cladding mode of the light. Many other approaches have been applied to the refractometry such as low coherence interferometers [22], fiber Bragg gratings [23, 24] and long period gratings (LPGS)[25]. However, they are not analyzed here as they share the similar principles with the sensors mentioned above.

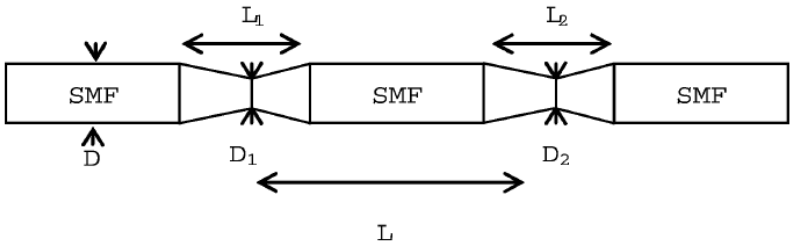

Fig. 2.4 Schematic structure of two-taper-type interferometer. [16]

To sum up, compared with the ray optical RI sensors, the sensors in this category can improve the detection limit to 10^{-4} -10^{-7} RIU, but it is hard to go any further. Normally there are two ways to enhance the detection limits, one is to increase the length of effective optical path in the liquid sample for the light-liquid interaction, which interference based sensors; the other way is to optimize the light detection system and signal extracting algorithm, just as what Ref. [12] did. For the first method, as shown in Eq. 2.2, the phase difference is linear to the effective optical length, and thus an increase of the effective optical length could raise the

"amplify coefficient" of the RI change. However, long optical length requires more volume of sample liquid, which is not good for some biochemical applications. For example, Mach-Zehnder interferometers can offer extreme high detection limit ($\Delta n = 10^{-4} \sim 10^{-7}$ RIU) [18], but the interaction length (typically 4 cm) is not suitable for cell-scale applications. For the second method, the improvement is at the cost of increased complexity and instability of the whole system, making it feasible for many common applications.

2.1.3 Refractive index sensors based on near-field optics

The near-field optics makes use of evanescent waves in the subwavelength region near the interface of two media and have attracted more and more interests. Inspired by the recent rapid progress of nano-optics, different near-field mechanisms have been incorporated into the RI measurement, notably surface plasmon resonance (SPR) [26-40], whispering gallery modes of micro-resonators [41-45], photonic crystal fibers [52-66], slab waveguides [67-70], and optical tunneling effect [71].

The SPR is considered to be the excitation of the surface plasmon polaritons (SPPs) or surface plasmon waves (SPWs), which are the electronmagnetic waves

coupled with free electron density oscillations on the surface between the metal layer and a dielectric medium. Several configurations could be used to excite the SPR, including the prism coupler-based configuration grating coupler-based configuration and optical waveguide-based configuration. The prism coupler-based configuration is the most common approach for exciting SPR, which is shown in Fig. 2.5.

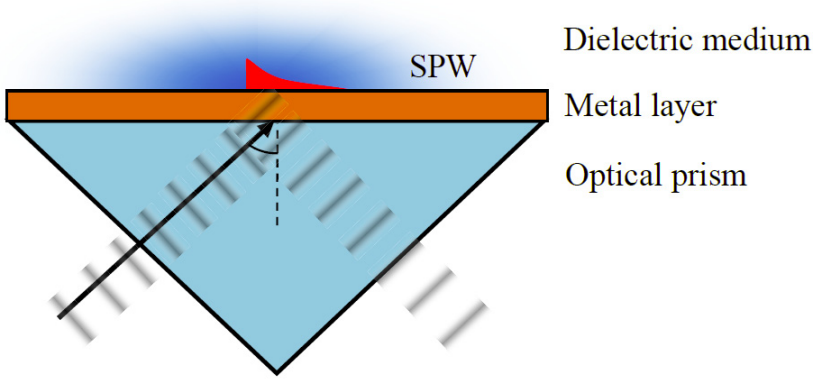

Fig. 2.5 Schematic diagram of surface plasmon resonance (Kretschmann method).

In this method, a metal thin film (Au or Ag) is deposited on the optical prism, and immersed in the dielectric medium (target solution). When a light is incident beyond the critical angle (TM polarized), there will be an evanescently decaying field on the interface of metal layer and optical prism. As the metal layer is very thin (30 – 60 nm), such evanescently decaying field could penetrate the metal thin film and remain stable at the metal-dielectric medium boundary. When the

frequency of light matches the natural frequency of surface electrons oscillating against the restoring force of positive nuclei, the SPP can be excited and propagate along the interface of the metal and dielectric medium. Such matching condition of excitation of SPR could be explained as [26]:

$$k_z = k_{SP} \tag{2.3}$$

here k_z is the propagation constant of the evanescent wave as expressed by

$$k_z = \frac{2\pi}{\lambda} n_p \sin\theta \tag{2.4a}$$

where θ is the incident angle, λ is the wavelength of the incident light and n_p is the RI of optical prism. k_{SP} is the propagation constant of SPWs on the other side of metal thin film, can be expressed as

$$k_{SP} = \mathrm{Re}\left(\frac{2\pi}{\lambda}\sqrt{\frac{\varepsilon_d \varepsilon_m}{\varepsilon_d + \varepsilon_m}}\right) \tag{2.4b}$$

where ε_d and ε_m are the permittivities of the dielectric medium and the metal, respectively. At $k_z = k_{SP}$, the matching condition is satisfied, and the SPR will become excited. The oscillation leads to a wavelength (λ) dependent reduction in the overall reflection, which presents an absorption peak in the reflection spectrum.

As the SPR is very sensitive to the RI near the metal surface (within ~300 nm), it is widely used to develop RI sensors [26] and biosensors [27]. Different

types of fibers (single mode [28-35], multimode [36-39] and polarization maintain fiber [40]) with different structures (off-cladding [36, 37], taper [28, 38], D-shape[29, 30, 32, 40] and modified end [31,39] have been demonstrated). The detection limits of these sensor ranged from 2.5×10^{-4} [36] to 7×10^{-7} RIU [28], or equivalently 300 to 127500 nm/RIU [28, 35]. Among these sensors, Monzon-Hernandez et al's work achieved the highest sensitivity. [28] Their design was quite simple. Standard single mode telecommunication optical fiber (Corning SMF-28) was tapered in 25 μm diameter and 4 mm length. The metal layer covered the whole taper area. The thickness of coated gold layer was 25 nm. Several surface plasmon modes were excited by the thin semi-cylindrical metallic shell. When the taper was immersed in the different liquids, the SPR absorption peaks was shifted as the RI of surrounding liquids was varied. Although the fiber based SPR RI sensors bear the advantages of easy fabrication and high sensitivity, the low detectivity is the drawback of the SPR sensor, which will be analyzed in the next chapter.

Optical resonators based on whisper gallery (WGMs) modes have recently attracted many research interests in sensing applications. [41-45] In such resonators, the light propagates in the form of WGMs originating from the total internal

reflection of the light along a curved surface. The WGM is the surface mode and its evanescent field extends into the surrounding medium for approximately 100 nm.[41] As a result, the WGMs are very sensitive to the change of RI in the surrounding medium. One example for the WGMs RI sensor application is presented as Hanumegowda's work. [41] A fused silicon microsphere was used as the resonator. The broad band light was coupled into the microsphere through an angle polished fiber prism and the WGM, was collected by the detector. Similarly, the whispering gallery resonators could be realized in optical microfiber coils [42], cylindrical shells[43] and micro-sized capillaries [44]. Experimental results show that the sensitivities of these sensors are typically 40 nm/RIU. In 2008, Xiao further optimized the design by using a pair of coupled resonant cavities instead of the single cavity. [45] In this design, one of the cavities is used as the sensing head immersed in the analyte, and the other works in the normal condition as the feedback cavity. The measurement system possesses a sharper asymmetric lineshape compared with the symmetric lineshape coming from the single cavity, which has one order of magnitude increase in the transmission slope and thus enhances the sensitivity of the sensor. The sensitivity of the WGM sensor is determined by the

overlap of the resonant modes and the liquid sample, which is the degree of light-liquid interaction. Since the width of the resonance peak is inversely proportional to the Q factor, smaller shift in the resonance spectrum could be detected when the resonance peak is narrower. The Q factors of these sensor mentioned above is between $10^4 \sim 10^6$, which indicates the peak width is 0.1-100 nm. Although the Q factors of micro-resonantor could be much higher [46], these resonators are not found in the sensor applications. Because higher Q factor requires more strict processing precision, and the thermal stability becomes an issue for the sensor application. [44] For RI sensors application, the liquid sample should be conveniently loaded and unloaded. Nevertheless, for the WGM RI sensors, the resonant cavity and the light coupler (usually the fiber taper or the angled fiber tip) should be in position for high couple efficiency, which makes the transfer of different liquid samples not convenient. This is another disadvantage of WGM sensor for the RI sensor application.

Recently, photon crystal fiber (PCF) has raised many research interests for high-power and high-energy transmission [47, 48], Brillouin scattering [49-51], telecommunications [52, 53], fiber lasers and amplifiers [54-56], and optical sensors

[57-61], including RI sensors [62-66]. However, as the specific micro-structures of PCF are different, different PCFs have different characteristics, and the principles for RI sensing can be different. Photonic bandgap fibers are characterized by having a hollow core by a pattern of periodically distributed air micro-holes along the entire length of fiber. The transmission spectrum of this kind of PCF has some transmission windows (bandgaps), of which positions and bandwidths are related to the geometry of optical fiber and the RI contrast between the optical fiber and the holey area. In 2007, J. Sun used photonic bandgap fibers for the RI measurement.[62] The holes were filled with different liquid samples with the same geometry, and the change of RI could cause a shift of the bandgap. The detection limit obtained was 2×10^{-6} RIU. Another kind of PCF is centered by a solid-core surrounded by periodically distributed holes. Due to the total internal reflection, light is confined to the foundation mode and propagates in the core. Because of the multi-hole structure, the evanescent wave is particularly strong compared with that in the standard optical fiber, which was utilized for the RI sensing by L. Rindorf.[63] In his work, long-period fiber gratings (LPGs) were written in the PCF, and the holes were filled with liquid samples, in which the evanescent wave passed through. The sensitivity of

sensor (2×10^{-5} RIU & 1,500 nm/RIU) was increased by 2 orders of magnitude than the traditional design. Wu et al. proposed a more sensitive design which integrated only one liquid filled channel within the PCF. [64] The PCF functioned as a directional coupler, and the channel filled with liquid sample acted as a waveguide. When the RI of the liquid sample matched the RI of the core, the core mode could be coupled to the liquid channel mode, loading to notches in the transmission spectrum of the PCF. So the change of RI could be recorded as the shift of notches. The detection limit obtained reached 4.6×10^{-7} RIU. Although the PCF RI sensors could get very high sensitivity, it is difficult, to load the liquid sample into the micrometer-sized holes. Similar to the WGM sensors, the sensors are not convenient to carry different liquid samples. Moreover, the bandgaps of the PCFs are usually broad, which affects the detection limit of the sensors. In some designs, the dynamic range of RI is limited. Take Wu's work for example [64], the RI of the liquid sample should be very close to the RI of the core (about 1.47 RIU), and thus limits the applications of the sensors.

With the development of micro-fabrication technology, nanometer level silicon structure could be fabricated with high precision. Owing to its high sensitivity,

compact size and easy monolithic integration, slab waveguide has attracted an interest growing for the RI sensor development.[67-70] As an example, silicon photonic nano-wire was used as a grating structure by periodically varying the waveguide width. [67] The RI of liquid cladding was determined by the stop band edge. As to the spiral-shaped channel waveguide, the effective RI contrast (the RI difference between the waveguide and the liquid cladding) decreased as the radius of curvature of the waveguide decreased. [68] For specific liquid sample, when light propagated along the waveguide, the losses of waveguide gradually rose in the propagating direction until all the light was lost at a certain point in the spiral. The shift of this point was used for monitoring the change of RI of liquid samples. Although the waveguide-based RI sensors have many advantages as mentioned above, the couple of light to the waveguide is difficult and needs great effort, which limits the commercial applications.

In summary, the RI sensors based on near-field optic usually involve evanescent coupling, the liquid sample surrounds the optical device and interacts with the evanescent field. With the exponential decaying, the evanescent coupling has a much strong liquid-light interaction than the direct coupling (light directly

passes through the liquid sample), thus typically offers higher sensitivity than the wave-optical sensors. However, the evanescent-wave sensor is intrinsically limited by the short penetration depth of the decay field. [65] As the near-field effect is confined to a sub-wavelength region, it intensifies the interaction and thus further improves the detection limit to a level close to 10^{-7} RIU. The highest sensitivity of which the sensors based on different principles are presented in Table 2.1. It can be seen that currently the level of 10^{-7} RIU has become a formidable barrier and none of the available methods is able to go beyond it [12, 28, 64].

Table 2.1 Summary of working principle, detection limit of RI sensors.

Category of methods	Working principle	Detection limit (RIU)	References
Ray optics	- Abbé	10^{-2}-10^{-5}	[5]
	- Refraction	1×10^{-4}	[6]
	- Refraction	3×10^{-5}	[7]
	- Reflection	2.5×10^{-5}	[9]
Wave optics	- Diffraction	$\sim1\times10^{-3}$	[10]
	- Forward scattering	NA	[11]
	- Backward scattering	1×10^{-7}	[12]
	- Interference	10^{-4}-10^{-7}	[13-25]
Near-field optics	- Surface plasmon resonance	7×10^{-7}	[28]
	-Whispering gallery mode	$\sim10^{-7}$	[41]
	-Photon crystal fiber	4.6×10^{-7}	[64]
	-Slab waveguide	10^{-6}	[67]

2.2 Resonant optical tunneling effect

2.2.1 Photon tunneling

Before analyzing resonant optical tunneling effect (ROTE), the frustrated total internal reflection (FTIR), which is also called photon tunneling, is introduced as a basic component of the ROTE. As shown in Fig. 2.6, when a light beam transmits from a medium of high RI (n_1) to the lower RI medium (n_2), total internal reflection will occur if the incident angle exceeds the critical angle ($\theta_c = \arcsin(n_2/n_1)$). The incident wave is completely reflected back into the medium 1, but the electromagnetic field penetrates the low RI medium by a small amount (typically less than a wavelength). When the third medium is brought close to the boundary (within the distance of a wavelength), the evanescent filed could be coupled into the third medium.

For the light passes through a thin air separation, the amount of transmission T can be expressed as [71]

$$T = 1 - \left|(z^2+\delta^2)^2[(z^2-\delta^2)^2 + 4z^2\delta^2 \coth(\beta/2)]^{-1}\right| \tag{2.5}$$

$$\beta = (\frac{4\pi d}{\lambda})(n^2 \sin^2\theta - 1)^{1/2} \tag{2.5a}$$

where n is the RI of incident medium, d is the thickness of air separation, and θ is the incident angle. For S-polarization,

$$z = 1/(n\cos\theta) \tag{2.5b}$$

$$\delta = -(n^2 \sin^2\theta - 1)^{-1/2} \tag{2.5c}$$

For P-polarization,

$$z = \cos\theta / n \tag{2.5d}$$

$$\delta = (n^2 \sin^2\theta - 1)^{1/2} \tag{2.5e}$$

Here the S-polarization means the electric field is always perpendicular to the incident plane, it can be also called as the transverse electric (TE) polarized light. Similarly, the P-polarization means the electric field is always inside the incident plane and is the same as the transverse magnetic (TM) polarized light.

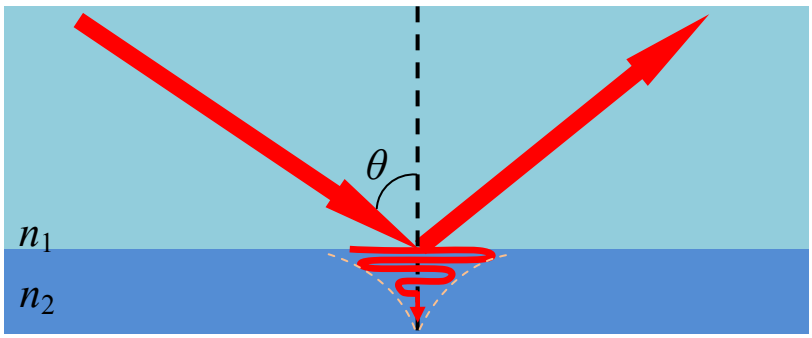

Fig. 2.6 Schematic diagram of photon tunneling.

Grattan et al. demonstrated a fiber-optic pressure by using the FTIR, the pressure caused small displacement of optical element, which was indicated by the

reduction of transmission intensity. [72] Spillman reported the novel fiber-optic hydrophone based on the FTIR, acoustic wave propagating in the water is detected by a pair of opposite angled multimode optical fibers. [73] The FTIR was also applied to the RI sensors by Kameoka. [74] In his work, a micro-channel filled with liquid sample was sandwiched between two transparent glass layers as the photon tunneling chip. For each sample, collimated laser light illuminated the device from one side, and the reflected light was collected as a function of incident angle. As a result, the reflection-incident curves of different samples were recorded and compared with simulation results. According to the author's experimental results, the detection limit of this sensor is better than 3.6×10^{-4} RIU.

2.2.2 Resonant optical tunneling effect

In 1988, the resonant optical tunneling effect (ROTE) was first proposed by Yeh. [85] For the FTIR, when the barrier becomes thicker, the transmission beyond the critical angel is less than the unity. However, as shown in Fig. 2.7, when two barriers are separated by a layer of high RI medium and act as high-reflectance mirrors, under certain condition the electromagnetic radiation could tunnel through these barriers

and the transmission could be unitary. However, Pochi Yeh just preliminarily proposed the definition without any further characteristics analysis.

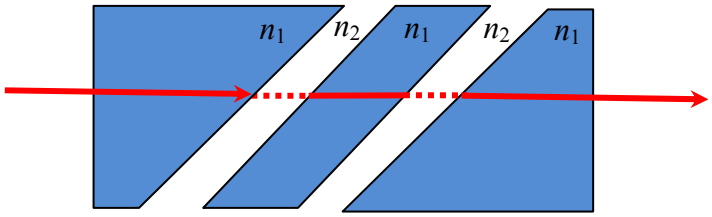

Fig. 2.7 Schematic drawing of a layered structure consisting of two barrier layers separated by a layer of high index of refraction. [85]

Many research effects have been put on the propagation of electromagnetic radiation in periodically stratified media. Having considered the similarity of the situation of light wave propagating through the multi-layer structure and the electrons in crystals, Yeh used the unit cell translation operator to obtain the solutions of the multi-layer structure. [86] The dispersion relation of the structure was analyzed and the existence of band structure was identified. Later the theory was applied to the superlattice structures. [87] Vigoureux and Baïda investigated the transmission through a *n*-resonant barrier structure and found that the transmission efficiency increased abruptly when *n* is larger than 40 (here *n* is the number of layers). [88] Nevertheless the Bloch wave, which describes the waves propagating in the crystal, is suitable for the structure consisting of a large number of layers. For the

structure with $n < 10$, these results are not appropriate. Parametric study of finite-number-layer structures, particularly two or three barriers, have not been carried out yet, and the contributions of the parameters (including the polarization-states, wavelength of incident light, incident angle) should be further examined.

As a new physical mechanism, the ROTE has attracted more and more research interests these days, focusing mainly on the principle and exploited the applications. There are some previous studies carried out be some groups. [89-91, 95] In 1999, Hayashi et al. first demonstrated the resonant optical tunneling (resonant photon tunneling) in experiment. [89] As presented in Fig. 2.8, multilayer samples was fabricated by using an active layer (Al or Al_2O_3) sandwiched by SiO_2 layers on SF10 glass prism.

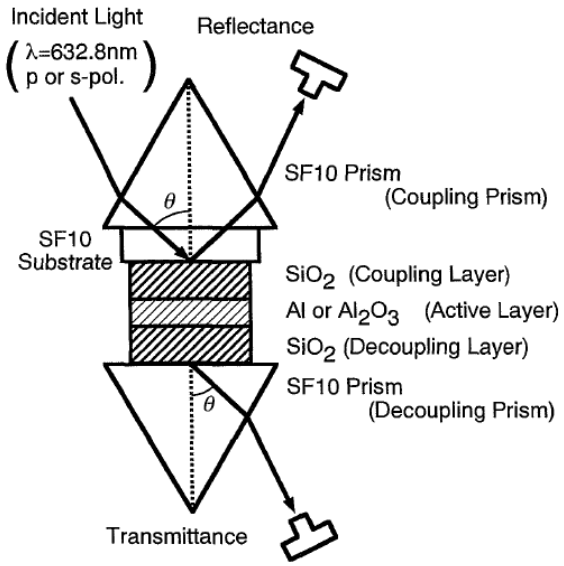

Fig. 2.8 The prepared sample and the experimental configuration of FTIR. [89]

A He-Ne laser with 632.8 nm wavelength was used as the light source. The reflectance and transmittance of the structure were measured as a function of the incident angle. For the Al active layer, a reflection valley and a corresponding transmission peak emerged at the angel beyond the critical angle, indicating the tunneling of photon through two barriers. However, the appeared dip and peak could be observed only in the P-polarized irradiation, and should be long-range surface plasmon polariton. In case of the Al_2O_3 active layer, the reflection dip and the transmission peak were shown for both the P- and S- polarization states.

Similar work was also shown by Yamamoto et al. [90, 91], a multi-layered GaAs/AlGaAs structure was used as a tunneling medium for all optical switching and all optical memory function. The configuration of the multi-layer structure and the equivalent potential diagram are shown in Fig. 2.9 (a) and (b), respectively. As shown in the graph, a layer of low RI medium is sandwiched by high RI bulks, and the photon should penetrate two barriers for transmission. In the experiment, they varied the incident light and measured the reflection intensity. Two sharp absorptions of the reflection were observed at certain angles, which were due to the first- and second-order tunneling modes. Furthermore, the resonant angle shifted

linearly with respect to the increasing RI change of the active layer. Thus the optical switching and all optical memory function could be achieved by varying the RI of active layer, which was induced by the control light irradiation on the active layer.

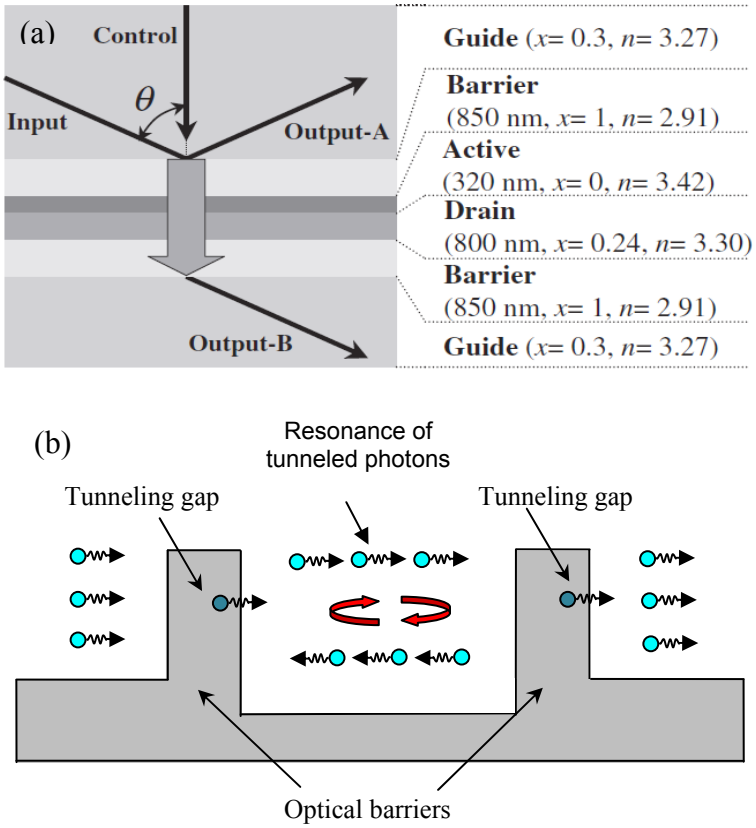

Fig. 2.9 All-optical switch device based on resonant photon tunneling effect. (a) Structure of device, where *x* is the Al content and (b) The optical equivalent of potential diagram. [90]

Liu's group had developed a series of thermo-optic switches based on the photon tunneling effect and the ROTE. [92-95] In the first design shown in Fig. 2.10

(a), a silicon micromachined prism functioned as the switching medium. [92, 93] When the RI of the silicon prism was changed by varying the temperature, the input light passed through the prism or was totally reflected at the silicon-air interface, which represented the on or off states, respectively.

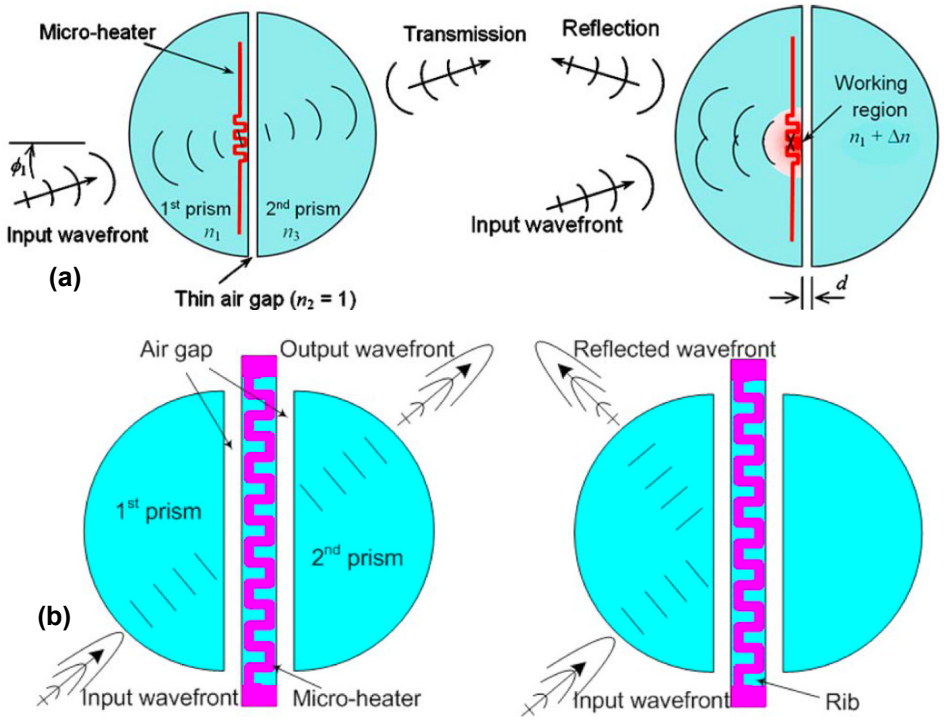

Fig. 2.10 Working principle of the switch based on optical barrier (a) and optical well (b). [92-94]

To further improve the sensitivity of RI change and the selectivity of light, another design used the optical well (Fig. 2.10 (b)) was instead of the optical barrier.[94] The optical well was formed by a thin air gap sandwiched between two

hemicylindrical prisms. Similar to the previous one, the switch function was realized by heating up the working region. However, both the single barrier and single well structure required significant RI change (0.01-0.02 RIU), and only worked for the S-polarized light. To solve this issue, the next step of improvement cascaded two optical barriers to form a resonant cavity for the tunneled waves. [95] The device consisted of two hemicylindrical silicon prisms, two air gaps, and a silicon rib, and maintained asymmetry in the horizontal direction. The photograph of fabricated device is shown in Fig. 2.11. The initial tunneling (the on state) was obtained by choosing proper parameters of the structure. The off state could be obtained by heating up the rib region. The ROTE not only worked for both the P-polarization and S-polarization but also improved the sensitivity.

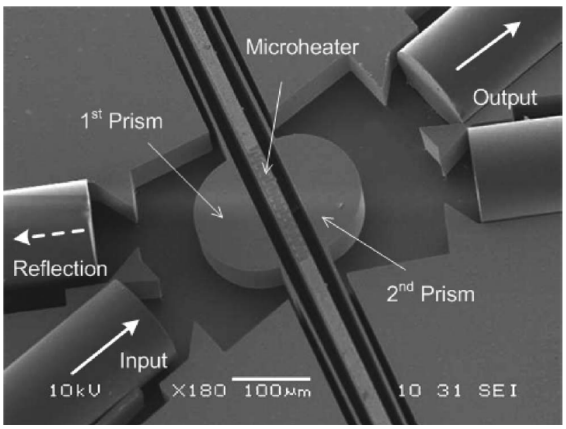

Fig. 2.11 Scanning electron micrograph of the fabricated thermo-optic switch. [95]

2.3 Summary

In summary, after the decades of evolution the RI sensor has achieved higher and higher sensitivity by adopting more and more advanced principles based on the ray optics, the wave optics and the near-field optics. On the other hand, the resonant optical tunneling effect has been applied to the optical switches but its potential for RI sensing remains almost untouched. It is worth conducting in-depth physical study and experimental demonstration.

Chapter 3 Theory of Resonant Optical Tunneling Effect

In this chapter, resonant optical tunneling effect (ROTE) is explored by two approaches: the nano-optics interpretation and the quantum mechanics interpretation. The former is based on the wave nature of the light and treats the tunneling effect as the propagation of light waves through a multilayered structure. The latter is based on the particle nature of the light and treats the tunneling effect as the photons going through potential barriers. Fundamentally, the nano-optics interpretation is based on the Maxwell equations while the quantum mechanics interpretation is based on the Schrödinger equation.

The structure of this chapter is as follows. The nano-optics interpretation is presented as a classical method in section 3.1. As the basic analytical model the transfer matrix method (TMM), will be introduced firstly. The silicon-air-silicon-air-silicon model will be used as the model structure to investigate the ROTE. Next, for the quantum mechanics interpretation, previous studies provided only the basic

concept for limited structures. In this work, the basic corresponding relationship will be generated to build up the theory model for the ROTE.

3.1 Nano-optics interpretation of resonant optical tunneling effect

3.1.1 Transfer matrix method

The reflection and transmission of the light from a single interface between two media could be described by the Fresnel equations. However, when there are multiple interfaces, the reflections themselves are also partially transmitted and partially reflected, thus the overall reflection (or transmission) of a layer structure is the sum of an infinite number of reflections (or transmissions), which is cumbersome to calculate. However, according to Maxwell's equations, on the continuity conditions of the electric field across the interface, the field at the end of the layer can be derived from the field at the beginning of the layer by using a simple matrix operation. A stack of layers can then be expressed as a system matrix, which is the product of all the individual layer matrices. The TMM simplifies the calculation due to the matrix operation, and has been widely used in the optics to analyze the

propagation of electromagnetic waves through a stratified (layered) medium, and the systematic description of TMM could be found in Yeh's work [85] and Furman and Tikhonravov's work[96].

As the RI sensor structure can be treated as a multilayer optical medium (see Fig. 3.1), the TMM could be used to calculate the transmission of the incident light through the RI sensor. In the TMM, each layer is called a slab, the slabs are numbered by 0 to *N*-1 from the input side to the output side, the input space is numbered as 0 whereas and the output space is as *N*.

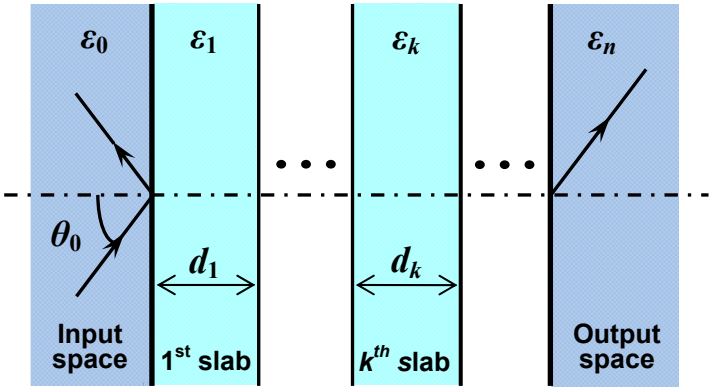

Fig. 3.1 Schematic graph of light propagating in multilayer system.

According to the TMM, when the light passes the slabs, the electric field vector and the magnetic field vector follow the relationship

$$\begin{bmatrix} E_N \\ H_N \end{bmatrix} = [M] \cdot \begin{bmatrix} E_0 \\ H_0 \end{bmatrix} \tag{3.1}$$

where E_0 and H_0 are the electric field vector and the magnetic field vector on the input side (i.e., in the interface between the input space and the 1st slab); E_N and H_N are the electric field vector and the magnetic field vector on the output side (i.e., in the interface between the $(N\text{-}1)_{th}$ slab and the output space); and $[M]$ is the characteristic matrix of the multilayer structure as defined by

$$[M]=\begin{bmatrix} m_{11} & m_{12} \\ m_{21} & m_{22} \end{bmatrix} = M_{N-1}\cdots M_1 = \prod_{k=1}^{N-1}\begin{bmatrix} \cos\delta_k & \frac{i\sin\delta_k}{\eta_k} \\ i\eta_k\sin\delta_k & \cos\delta_k \end{bmatrix} \tag{3.2}$$

here δ_k is the phase factor of the k_{th} slab as given by

$$\delta_k = \frac{2\pi}{\lambda} n_k d_k \cos\theta_k = \frac{2\pi d_k}{\lambda}(\varepsilon_k - n_0^2 \sin^2\theta_0)^{1/2} \tag{3.3}$$

The variable d_k is the thickness of the k_{th} slab, θ_0 the incident angle, λ the wavelength, n_k is the refractive index with $n_k = (\varepsilon_k \mu_k)^{1/2}$, and ε_k and μ_k are the permittivity and permeability of the k_{th} slab, respectively. The variable η_k is the optical admittance and has different forms for different polarization states, there are $\eta_k^s = (\frac{\varepsilon_k}{\mu_k})^{1/2}\cos\theta_k = (\varepsilon_k - n_0^2\sin^2\theta_0)^{1/2}$ for S-polarization and $\eta_k^p = (\frac{\varepsilon_k}{\mu_k})^{1/2}\frac{1}{\cos\theta_k} = \frac{\varepsilon_k}{\eta_k^s}$ for P-polarization ($\mu_k = 1$ for non-magnetic material).

Finally, the transmittance T of the entire multilayer structure (the fraction of incident light that passes through the structure) can be written in terms of the Fresnel reflections (t_s *and* t_p) and the elements of the matrix M [85]

$$T_s = \frac{\eta_N^s}{\eta_0^s}\left|t_s\right|^2 = \frac{\eta_N^s}{\eta_0^s}\cdot\left|\frac{2\eta_0^s}{(m_{11}^s + m_{12}^s\cdot\eta_N^s)\eta_0^s + (m_{21}^s + m_{22}^s\cdot\eta_N^s)}\right|^2 \tag{3.4}$$

$$T_p = \frac{\eta_N^p}{\eta_0^p}\left|t_p\right|^2 = \frac{\eta_N^p}{\eta_0^p}\cdot\left|\frac{2\eta_0^p}{(m_{11}^p + m_{12}^p\cdot\eta_N^p)\eta_0^p + (m_{21}^p + m_{22}^p\cdot\eta_N^p)}\right|^2 \tag{3.5}$$

The reflectance R of the whole multilayer system (the fraction of incident light that reflected back) can be similarly expressed as [85]

$$R_s = \left|r_s\right|^2 = \left|\frac{(m_{11}^s + m_{12}^s\cdot\eta_N^s)\eta_0^s - (m_{21}^s + m_{22}^s\cdot\eta_N^s)}{(m_{11}^s + m_{12}^s\cdot\eta_N^s)\eta_0^s + (m_{21}^s + m_{22}^s\cdot\eta_N^s)}\right|^2 \tag{3.6}$$

$$R_p = \left|r_p\right|^2 = \left|\frac{(m_{11}^p + m_{12}^p\cdot\eta_N^p)\eta_0^p - (m_{21}^p + m_{22}^p\cdot\eta_N^p)}{(m_{11}^p + m_{12}^p\cdot\eta_N^p)\eta_0^p + (m_{21}^p + m_{22}^p\cdot\eta_N^p)}\right|^2 \tag{3.7}$$

As shown in Fig. 3.2, the silicon-air multilayer system is set as the example to explore the ROTE and carry out the parameter study. The light is incident beyond the critical angle from the input space (n_a) and collected by the output space (n_s). This multilayer structure consists of three layers between the input and output spaces, i.e., the tunneling space, the central slab and another tunneling space. The thicknesses of the two tunneling spaces are same, noted as d in the following simulation. Similarly, the thickness of central slab is presented as g. In order to form the optical barriers, the RI of tunneling space should be less than that of input (output) space, and the silicon and air are used as central slab (RI = 3.42 RIU) and

tunneling space (RI = 1.00 RIU) in the simulation, respectively. As various shapes of silicon components could be achieved with high accuracy in the silicon process technology, all the components could be integrated in the whole chip. For this consideration, the input and output spaces use the silicon material, the same as the central slab.

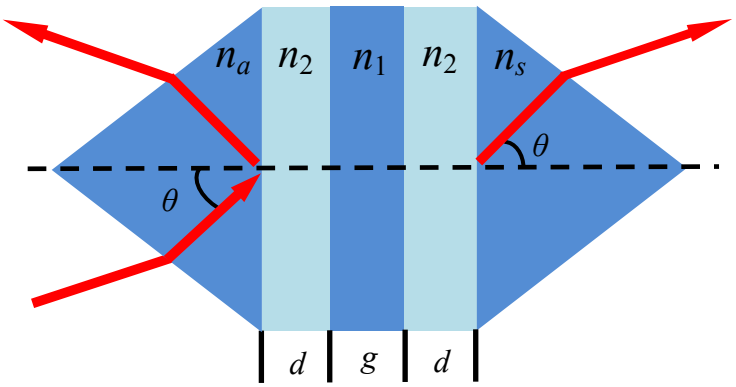

Fig. 3.2 Optical double barrier tunneling structure.

Based on the study above, the transfer matrix of optical double barrier tunneling (ODBT) structure can be expressed as

$$M = M_3 \cdot M_2 \cdot M_1 \tag{3.8}$$

where M_1, M_2 and M_3 represent the characteristic matrix of the tunneling spaces and the central slab as shown in Fig. 3.2. Such relationship can be easily extended to

more tunneling spaces. This is one of the beauties of the TMM. The overall reflectance and transmittance can be further calculated by Eqs. (3.4) - (3.7).

In the theoretical analysis below, it is assumed that:

(1) Every layer (including the input space, the output space and all the intermediate layers) are homogeneous and isotropic.

(2) All the layer boundaries are perfectly parallel and smooth.

In the analysis below, it is assumed that the multilayer structure is symmetric, so the entire multilayer structure has only 3 independent variables, the incident angle θ, the tunneling gap d and the central slab width g. Another variable of the wavelength λ can be normalized into d and g, and thus disappears. The influence of every variable will be investigated separately in the following part.

3.1.2 Parametric study of the incident angle

Figure 3.3 plots the relationship of the transmittance in response to the change of incident angle, in which $\Delta\theta$ represent the increase value of incident angle. As observed in Fig. 3.3, some peaks appeared in the range of incident angle larger than the critical angle. Both P- and S-polarization reach the maximum transmission at $\Delta\theta$

= 1.0 deg. The transmission peaks reappear at larger angle, but at different angle values for different polarization states. Thus this value ($\Delta\theta$ = 1.0 deg) is chosen to be the incident angle in the following simulations. Except the transmittance fluctuations caused by the peaks, the transmittance tends to drop as the incident angle increases. In the close-up views of the transmission peaks in Fig. 3.3 (b), the peak of S-polarization is much sharper than the peak of P-polarization. The transmittance of the S-polarization is dropped by more than 55 dB for an angle change of 0.1 deg, and that of the P-polarization is dropped by about 30 dB.

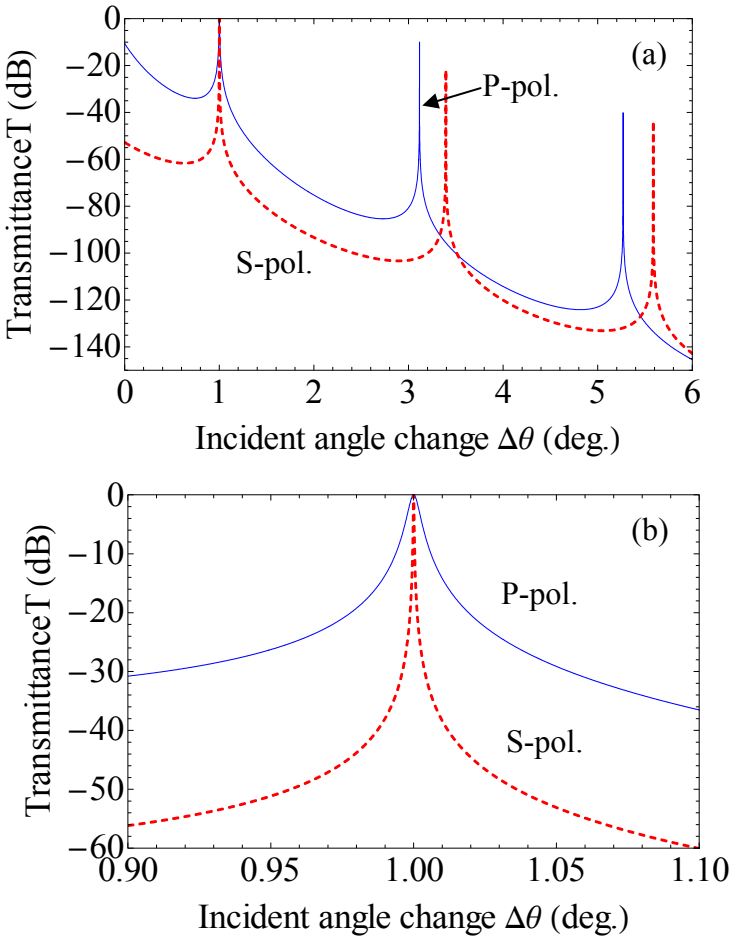

Fig. 3.3 Incident angle dependence of transmittance for both P- and S-polarization. (a) In the range $\Delta\theta$ = 3.0 ± 3.0 deg; (b) in the range $\Delta\theta$ = 1.0 ± 0.1 deg.

3.1.3 Parametric study of the central slab width

The transmittances of both S- and P-polarization are contoured in Fig. 3.4 with respect to the central slab width g and the tunneling gap d. It is to be noted that the widths of the tunneling gap and central slab are all normalized to the wavelength of incident light. Other parameters are $\theta = \theta_c + 1$ deg, and $n_a = n_s = n_1 = n_{Si}$, $n_2 = n_{air}$.

The bright region corresponds to high transmittance. As can be observed in Fig. 3.4(a) and (b), a spike of bright band appears upward for both P- and S-polarization. Near the spike, a small change of the slab width or the tunneling gap would cause a large variation of the transmission (from bright to dark). Fig.3.4 (c) and (d) plot the contours in a large range $g/\lambda = 10 \pm 0.5$. They reveal that the transmission peaks are periodically distributed as the central slab width g increases. The different height of peaks in the graph is due to insufficient of calculation points (N = 600). To demonstrate that, the relationships of T vs. g are plotted in Fig. 3.5 with more data points (N = 10,001), which correspond to the observation lines for d/λ = 1.5 in Fig. 3.4 (a) and (b). In the graph, the maximum points of all the peaks could reach 0 dB, which means the 100% transmittance could obtained for the specific g/λ and d/λ values. Further study shows that the peaks are the same, independent of the values of d/λ.

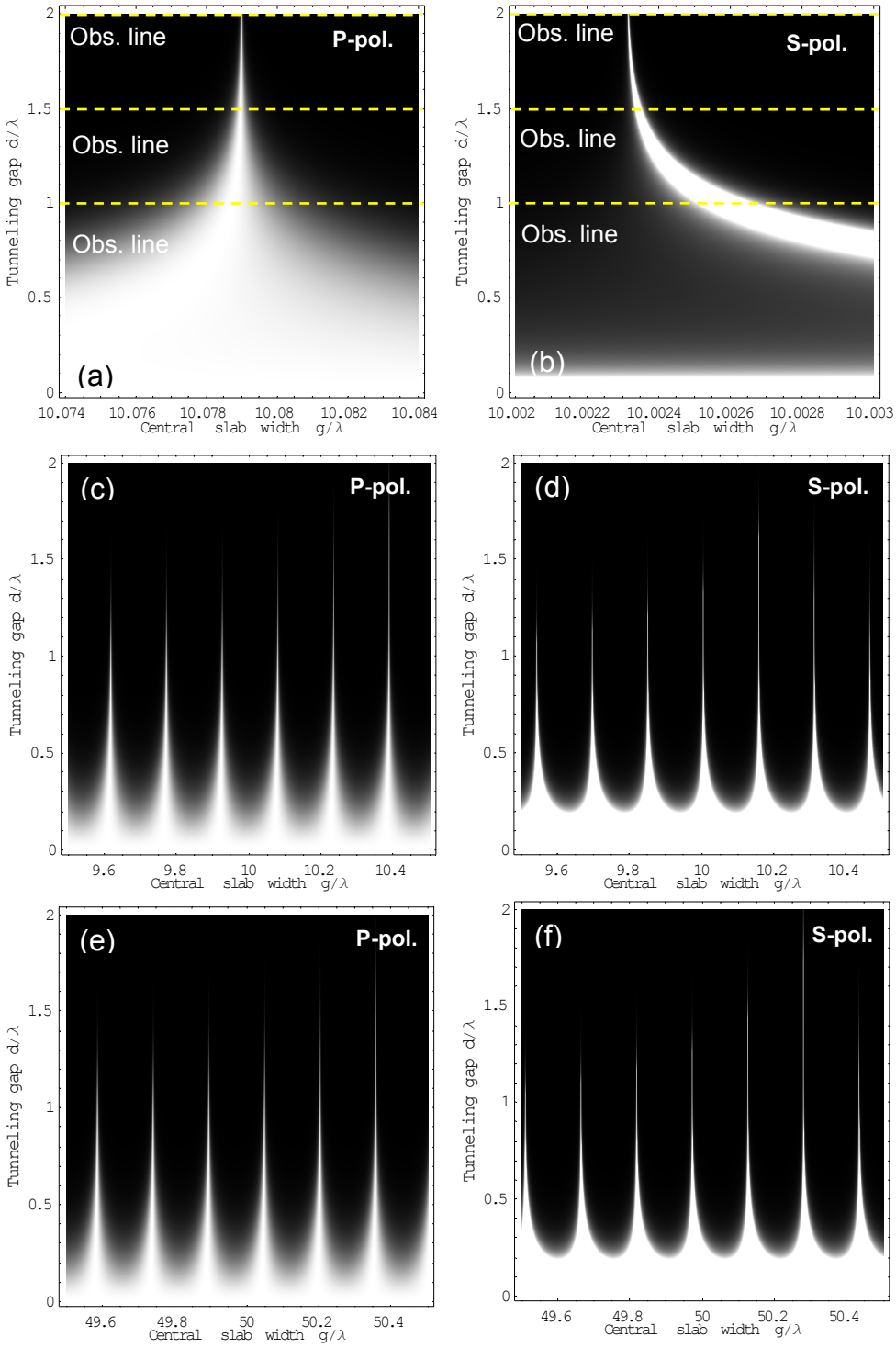

Fig. 3.4 Contours of the transmission with respect to the central channel width and the tunneling gap for P-polarization (a, c and e) and S-polarization (b, d and f) in different regions: (a) and (b), $g/\lambda = 10 \pm 0.03$; (c) and (d), $g/\lambda = 10 \pm 0.5$; (e) and (f), $g/\lambda = 50 \pm 0.5$.

To investigate the dependence of the periodicity of the peak on the central slab width, Fig. 3.4 (e) and (f) show the contours of transmittance in another range of $g/\lambda = 50 \pm 0.5$. For the S-polarization, there are 7 peaks in the range $g/\lambda = 50 \pm 0.5$, and exact the same number of peak in $g/\lambda = 10 \pm 0.5$. For the P-polarization, the peak number becomes 6 but remains the same in the two ranges. This observation shows that the periodicity of transmittance peaks is actually independent of the central slab width g/λ. It also can be observed that the peak positions for S- and P-polarization do not overlap; instead they are shifted by about half a period. In this sense, it is not possible to find a condition to let both polarizations reach the peak at the same time.

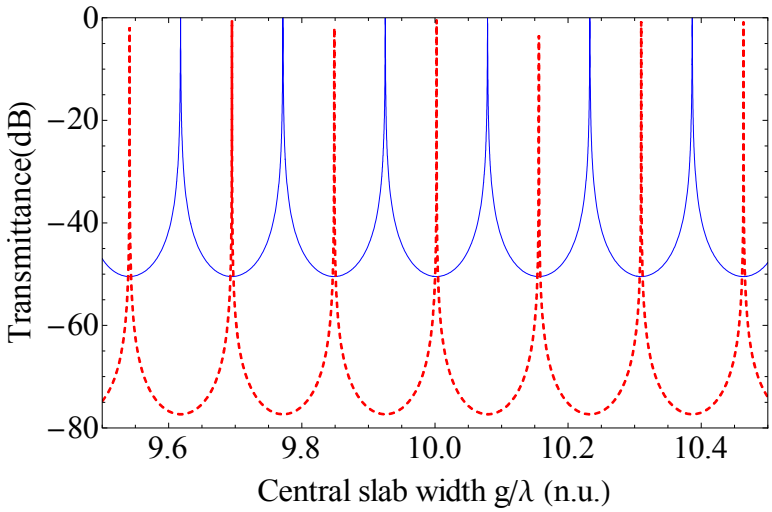

Fig. 3.5 Intensity transmittance as a function of the central slab width, corresponding to the observation lines for $d/\lambda = 1.5$ in Fig. 3.4 (a) and (b), in which the blue and red curve are for P- and S-pol., respectively.

To further investigate the position of the peaks, Fig. 3.6 (a) and (b) plot the curves of T vs. g/λ on conditions of d/λ = 1.0, 1.5 and 2.0 (along the observe lines in Fig. 3.4 (a) and (b)). The peaks are all symmetrical. It can be observed that the larger the value of d/λ is, the sharper the peak becomes. And the maximum position shifts with the d/λ changes for both P- and S-polarization. For S-polarization, the peak position shifts toward smaller g/λ with the increase of d/λ. However, for P-polarization the peak position shifts to the larger g/λ as the value of d/λ grows though the shift is not as obvious as that of S-polarization. For a better view, Fig. 3.7 plots the peak position as a function of d/λ. In the graph, it can be observe the shift directions of S-polarization and P-polarization are reverse as mentioned above. The shift tends to saturated as d/λ grows for both polarization states.

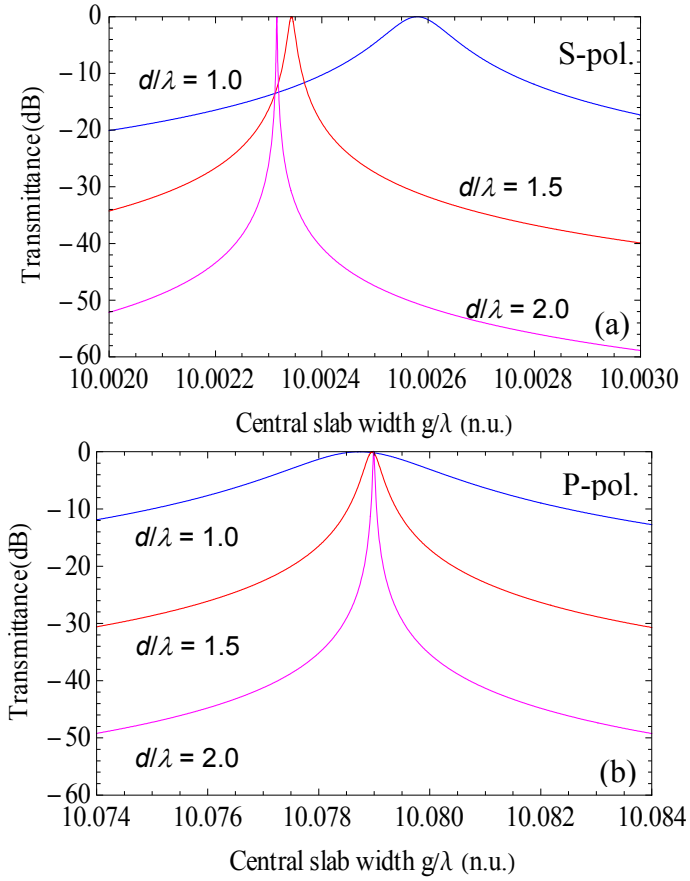

Fig. 3.6 Positions of the transmittance peaks at different tunneling gaps: S-polarization (a) and P-polarization (b).

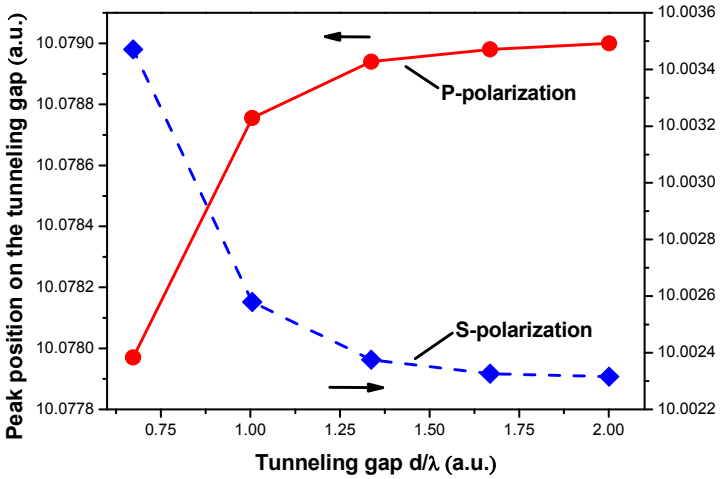

Fig. 3.7 Dependence of peak position on tunneling gap for P- and S-polarization.

3.1.4 Parametric study of the tunneling gap

To study the dependence of the transmittance on the tunneling gap, the curves of T versus d/λ at different parameters of g/λ (along the observe lines in Fig. 3.8) are plotted in Fig. 3.9 (S-polarization) and Fig. 3.11 (P-polarization). In S-polarization state dependent on g/λ, the behaviors of transmittance curves could be described as two groups, which are shown in Fig. 3.9 (a) and (b), respectively. When g/λ is larger than the threshold value (g/λ = 10.00232), the transmittance increases to the 100% transmittance and forms a peak after the initial decrease. If g/λ is smaller than the threshold value (g/λ = 10.00232), the transmittance decreases from 0 dB and drops gradually, never coming back to 100%. This can also be observed in Fig. 3.8 (a), from the top to the bottom, the tail of large horn shaped bright spike turns to right side, which indicates the transmittance could reach maximum value at the right side of the tip of the large spike (g/λ is larger than the threshold value) and decay at the left side of the large spike (g/λ is smaller than the threshold value). In the former case, the peak shifts toward smaller d/λ value as g/λ goes up. The relationship is

shown in Fig. 3.10. It can be seen that, the peak position of d/λ drops quickly with the increase of g/λ and then tends to saturate.

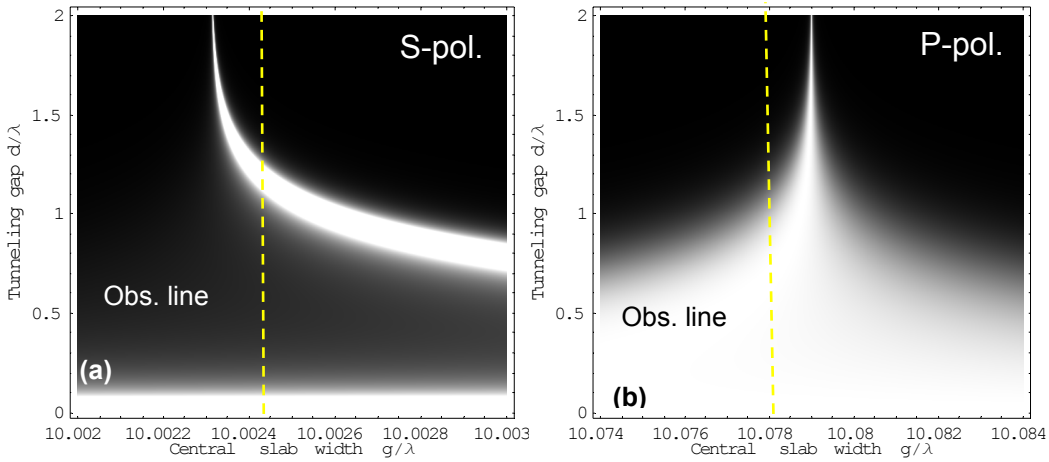

Fig. 3.8 Contours of the transmission with respect to the central channel width and the tunneling gap for S- and P-polarization.

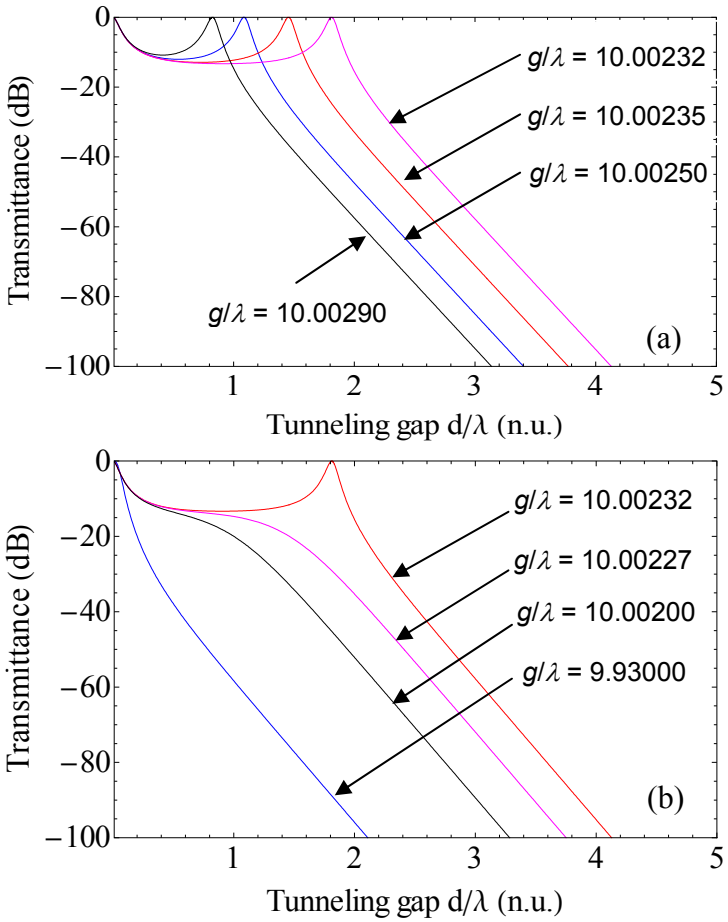

Fig. 3.9 The variation of the transmittance with the tunneling gap at different central slab widths for S-polarization. (a) The central slab width g/λ is larger than the threshold value. (b) The central slab width g/λ is smaller than the threshold value.

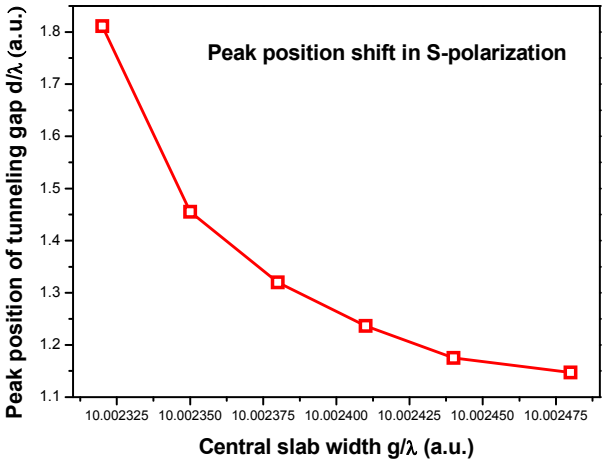

Fig. 3.10 Dependence of the transmittance peak position on the central slab width for S-polarization.

In case of P-polarization, the transmittance is kept nearly constant within a certain range of tunneling gap if the central slab has proper width. For example, T is always close to 1 in the range of $d/\lambda < 3.5$ at $g/\lambda = 10.078994$. The range quickly drops to $d/\lambda < 1.8$ when g/λ is increased by only 0.000006 to 10.079. However, in the zoomed views of the T vs. d/λ curve presented in Fig. 3.11 (c) and (d), which are corresponding to the green contours in Fig. 3.11 (a) and (b), the situation of P-polarization is similar to that of S-polarization. The behaviors of curves also could be divided into two groups, when the g/λ larger than the threshold value, the transmission will not reach 100% intensity, although the difference is very small (less than -0.2 dB). This is also demonstrated in Fig. 3.8, the bright spike of P-polarization is more bilaterally symmetrical than that of S-polarization. For the smaller g/λ value, the peak position will shift towards the smaller d/λ (shown in Fig. 3.12), of which the direction is opposite to that of S-polarization.

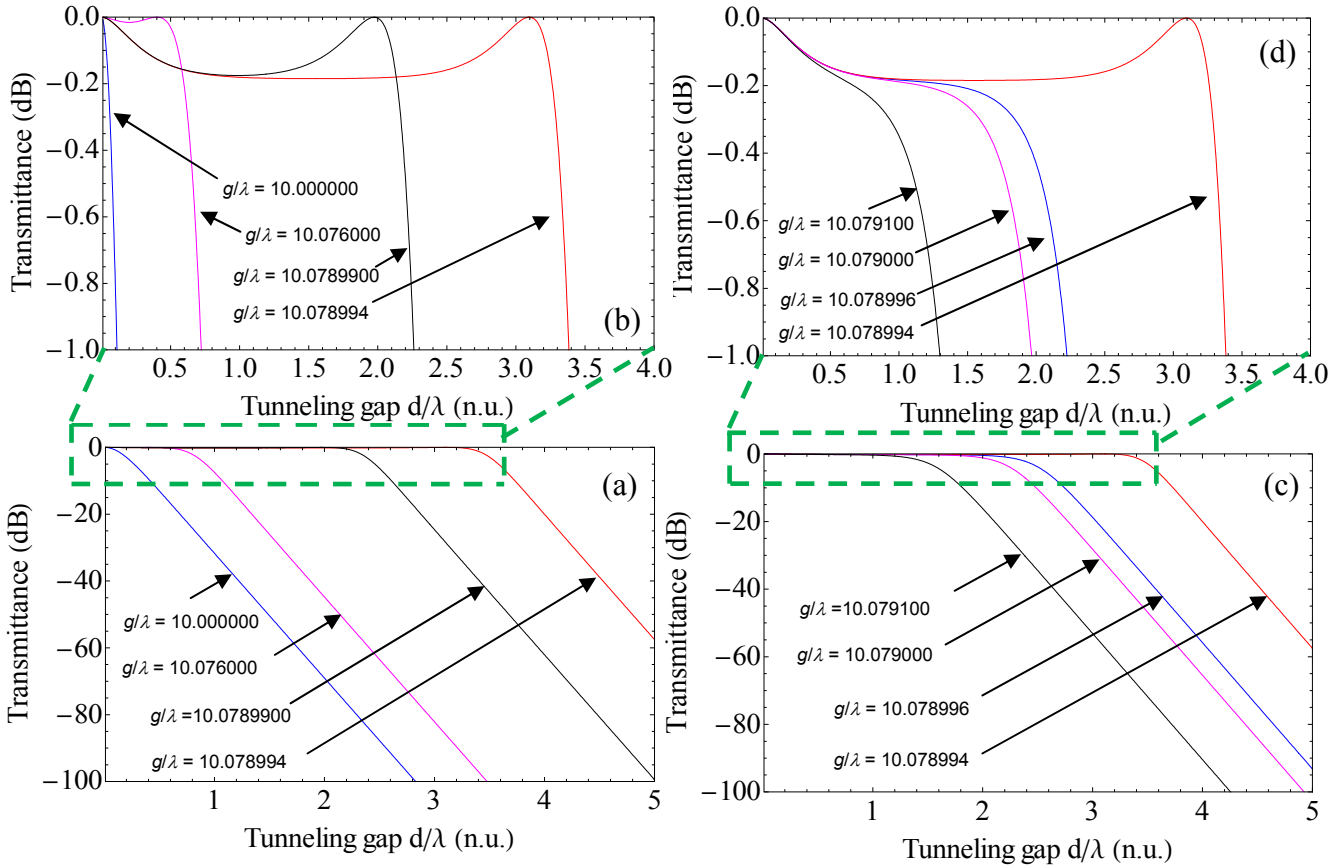

Fig. 3.11 The transmittance varies with the tunneling gap for with different central slab width for P-polarization, (a) the central slab width g/λ smaller than the threshold value; (c) the central slab width g/λ larger than the threshold value.

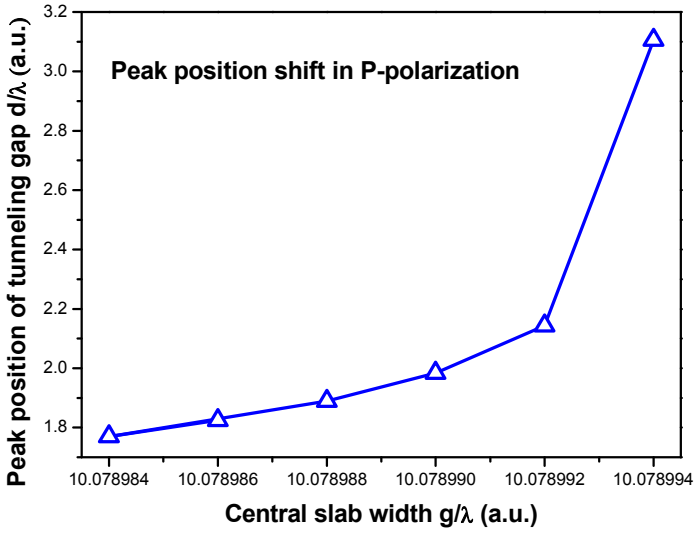

Fig. 3.12 Dependence of the transmittance peak position on the central slab width for P-polarization.

3.1.5 Parametric study of the incident wavelength

In the simulation performed above, the geometrical dimensions of structure, including the central slab width *g* and tunneling gap *d* are normalized to the wavelength of the incident light. Assumed that the laser is used as the light source, and the intensity of the transmission is recorded. In experimental study, this constitutes the intensity-based sensing scheme. For some applications, in order to achieve better resolution or to offset the environmental effect (e.g. thermal effect), the spectrum-based sensing scheme is another option and is more widely used than the intensity-based method.

In this scheme, the incident angle θ, the central slab width g and the tunneling gap d are maintained, a broad band light source is used instead of the laser, and the transmitted spectrum is monitored. Assuming the central wavelength of the broad light source is 1550 nm, in the simulation, the tunneling gap d = 2278.5 nm (1.47λ), and the central slab width g = 15500 nm (10λ). Other parameters are $\theta = \theta_c$ + 1 deg, and $n_a = n_s = n_1 = n_{Si}$, $n_2 = n_{air}$. The transmitted spectrum of the tunneling structure is plotted in Fig. 3.13. It can be seen that the peaks appeared in both P- and S-polarization are periodically distributed. Because every S-polarization peak appears at the valley between two P-polarized peaks, the peaks in both polarization states look to have the same period. However, after checking the exact peak values, the periods of S-polarization and P-polarization are slightly different, and they gradually rise from 22.75 nm to 24.97 nm and from 22.10 nm to 26.64 nm, respectively. In Fig. 3.13 (b), it can be observed that the peak in S-polarization is much sharper than the peak in P-polarization, but the bottom of P-polarization curve is about -50 dB, which is much higher than that of S-polarization curve (less than -60 dB).

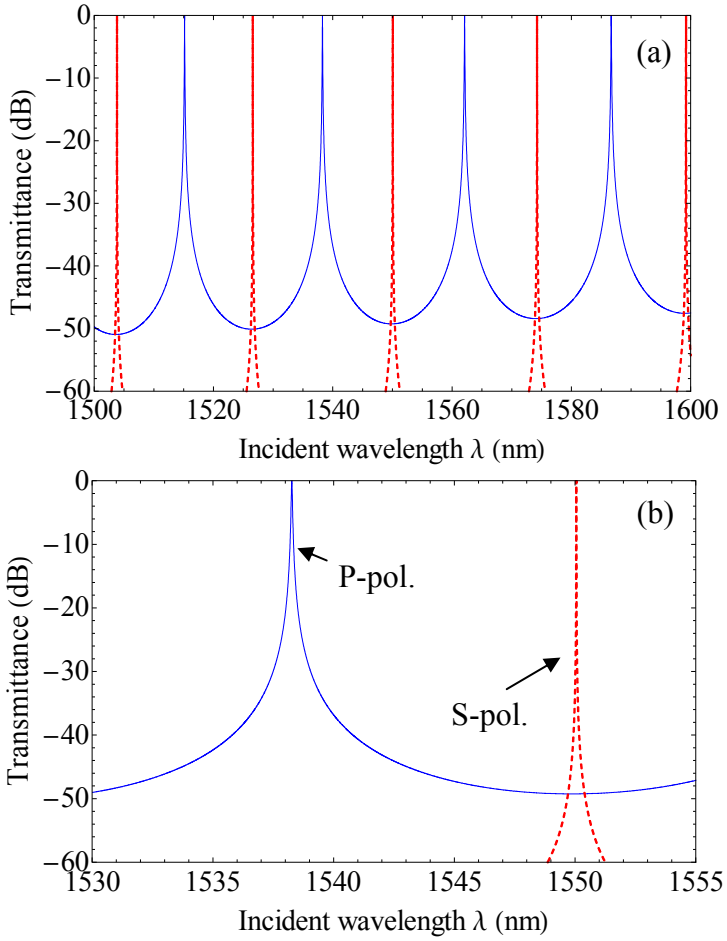

Fig. 3.13 Transmitted spectrum of the tunneling structure, (a) in the range of 1550 ± 50 nm, (b) in the range of 1545 ± 15 nm, in which the solid and dashed curve are for P- and S-polarization, respectively.

3.2 Quantum interpretation of resonant optical tunneling effect

In recent years the analogy between the propagation of electromagnetic waves and that of electron waves has received much experimental and theoretical attention. On

one hand, the optical analogy of quantum physics provides a convenient approach to visualize the ultrafast phenomena in the quantum field and to explore coherent dynamics that is not yet accessible in the quantum systems. For instance, photon tunneling was used as the basic model to investigate the fundamental physical properties of the electron tunneling such as tunneling time, superluminal effect and phase delay [80,81].

On the other hand, the quantum analogy of optics provides a unique angle to design the optical systems for unprecedented functions. A prominent example is the photonic crystal, which deals with the propagation of light in periodic dielectric structures [75-77]. It borrows the idea of electronic bandgap when electrons move in the crystal lattice and generates the optical bandgap for photons, which leads to a variety of phenomena of both fundamental and practical interest.

Another interesting analogy between photon and electron propagation, which has received less attention so far, lies in tunneling phenomena. The nano-optics interpretation of the tunneling phenomena, which is based on Maxwell's equations and transfer matrix model (TMM), has been presented in subsection 3.1. In this section, besides the classic model, another theoretical model: the potential

barrier model (PBM), which is originated from the quantum-optical analogies, will be elaborated. This model is used to explore the frustrated total internal reflection effect (FTIR) and ROTE, and will be compared with the results obtained by using TMM.

3.2.1 Analogy between photon tunneling and electron tunneling

The analogies of the electron tunneling and the optical tunneling are illustrated in Fig. 3.14. The ROTE can be better understood from the quantum equivalences of the total internal reflection (TIR) and the frustrated total internal reflection (FTIR). In the simple case that the light wave goes from a high RI medium to a low RI medium with an angle higher than the critical angle, it represents the classical TIR effect. In the close vicinity of the interface, the evanescent wave actually goes beyond the interface and its amplitude experiences an exponential decay. This is equivalent to an electron encountering a potential step with a potential height larger than the kinetic energy of the electron, as shown in Fig. 3.14(a). According to the relationship between the RI n and the optical potential V [84] (see Eqs. (10) and (11)), the high

RI medium corresponds to the low optical potential for the photons whereas the low RI medium produces the high optical potential. With these, and the TIR structure is equivalent to an optical step.

For the FTIR of the lightwave, another high RI medium is added close to the first high/low interface and part of the evanescent wave can go through the second interface to form a transmission. The amplitude and phase of the transmitted wave follow exactly the same relationship of an electron tunneling through a thin potential barrier as shown in Fig. 3.14(b). In this regard, the FTIR structure forms effectively an optical barrier for the photons.

In the ROTE structure for the lightwave, two low RI layers are sandwiched subsequently between three high RI layers. It is easy to see that the ROTE structure is equivalent to the double potential barriers as shown in Fig. 3.14(c). And the property of the ROTE for lightwave is similar to that of an electron going through a potential well, which has been widely used for resonant tunneling diodes (RTDs). For these reasons, the ROTE structure produces an optical well for the photons.

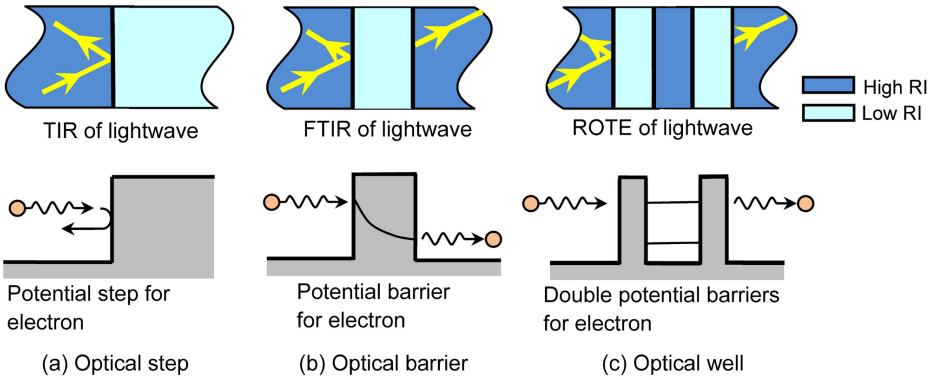

Fig. 3.14 Optical phenomena and their quantum equivalences. (a) Total internal reflection (TIR) of the light is equivalent to the electron encountering a potential barrier; (b) Frustrated total internal reflection (FTIR) of the light is equivalent to the electron tunneling through a potential well; and (c) Resonant optical tunneling effect (ROTE) of the lightwave is equivalent to the resonant tunneling of the electron through a double potential well.

3.2.2 Quantum interpretation of frustrated total internal reflection effect

3.2.2.1 Analogical equations

In this section, the analogy of single barrier model for the optical and electronic structure is introduced.

Figure 3.15 (a) shows the photon tunneling in a FTIR structure. For simplicity, it is assumed the FTIR structure consists of a glass/air/glass multilayer

structure. A P-polarized photon (wavelength λ=514 nm) is incident upon a glass–air interface at an angle θ greater than the critical angle. For the P-polarized waves in the glass region, the wave equation for the H field [97],

$$\nabla^2 H - \frac{n^2}{c^2}\frac{\partial^2 H}{\partial t^2} = 0 \tag{3.9}$$

where n is the refractive index of the glass and c is the speed of light in vacuum. If the wave is a plane wave with an angular frequency ω, Eq. (3.9) can be rewritten as

$$\frac{\partial^2 H}{\partial x^2} + \left(\frac{n^2\omega^2}{c^2} - k_y^2\right)H = 0 \tag{3.10}$$

where k_y is the y-directional component of the incident (or reflected) wave vector, i.e.,

$$k_y = \frac{n\omega}{c}\sin\theta \tag{3.11}$$

Substituting Eq. (3.11) into Eq. (3.10), it can be obtained as

$$\frac{\partial^2 H}{\partial x^2} + \frac{n^2\omega^2}{c^2}(\cos^2\theta)H = 0 \tag{3.12}$$

In the air region, similar to Eq. (3.10), it has

$$\frac{\partial^2 H}{\partial x^2} + \left(\frac{\omega^2}{c^2} - k_y^2\right)H = 0 \tag{3.13}$$

where k_y is the same as that in the glass region because the y-directional component of the propagation vector is conserved. Therefore, substituting Eq. (3.11) into Eq.

(3.13), it has

$$\frac{\partial^2 H}{\partial x^2}+\frac{n^2\omega^2}{c^2}(n^2\sin^2\theta-1)H=0 \tag{3.14}$$

As shown in Fig. 3.15 (b), the time-independent Schrödinger equation for a hetero-structure potential barrier is,

$$\frac{\partial^2 \psi}{\partial x^2}+\frac{2m_1 E}{\hbar^2}\psi=0 \tag{3.15}$$

in the region $x<0$ or $x>d$ and

$$\frac{\partial^2 \psi}{\partial x^2}+\frac{2m_2}{\hbar^2}(V_0-E)\psi=0 \tag{3.16}$$

in the region $0>x>d$, where m_1 and m_2 are the effective masses of electrons in the corresponding regions. Comparing Eqs. (3.12) and (3.14) with Eqs. (3.15) and (3.16), respectively, the following substitutions make the equations of H equivalent to those of ψ:

$$2m_1\frac{E}{\hbar^2}\Leftrightarrow\left(\frac{\omega}{c}\right)^2(n^2\cos^2\theta) \tag{3.17}$$

$$2m_2\frac{V_0-E}{\hbar^2}\Leftrightarrow\left(\frac{\omega}{c}\right)^2(n^2\sin^2\theta-1) \tag{3.18}$$

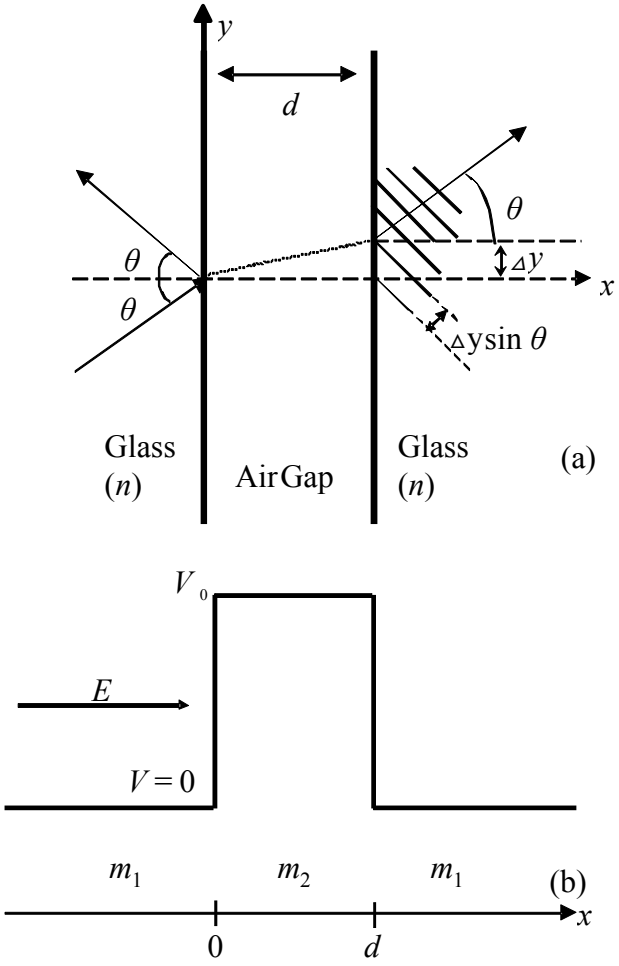

Fig. 3.15 (a) The photon tunneling in a FTIR structure (n is the refractive index of glass). (b) One-dimensional electron tunneling through a hetero-structure potential barrier (m_1 and m_2 are the effective masses of an electron in the corresponding regions). [82]

According some previous work from other groups [80, 82], for different polarization states, the effective mass ratios are different; i.e., $m_2 / m_1 = 1/n^2$ in the P-polarization case and $m_2 / m_1 = 1$ in the S-polarized case. Therefore the P-polarized

wave tunneling problem can be converted into the electron wave tunneling problem. And the generalized analogical relationships as expressed by [80, 82]

$$E = \frac{\hbar^2 n_1^2 \omega^2}{2 m_1 n_2^2 c^2} \cos^2 \theta \tag{3.19}$$

$$V_0 = \begin{cases} \dfrac{\hbar^2 n_1^2 \omega^2}{2 m_e n_2^2 c^2} \left[\left(\dfrac{n_1}{n_2} \right)^2 - 1 \right] \sin^2 \theta & \text{for S-pol. (i.e. TE)} \\ \dfrac{\hbar^2 \omega^2}{2 m_e c^2} \left[\left(\dfrac{n_1}{n_2} \right)^2 - 1 \right] & \text{for P-pol. (i.e. TM)} \end{cases} \tag{3.20}$$

here E is the kinetic energy of the electron, V_0 is the height of potential barrier, c is the speed of light in vacuum, $\hbar$ is the reduced Plank constant, m_e is the mass of electron, ω and θ are the angular frequency and incident angle of light, respectively.

However, Eqs. (3.19) and (3.20) are lengthy and complicate. A simpler and more intuitive analogical relationship was adopted in Hooper's and our work [84, 98, 99], as expressed by

$$E = -n_1^2 k_0^2 \sin^2 \theta \tag{3.21}$$

$$V_0 = -n_2^2 k_0^2 \tag{3.22}$$

where k_0 is the wavenumber of the incident light in free space. Although this corresponding relationship is not mathematically rigid, it is straightforward and reflects most of the features of the optical barrier structure (e.g., change of the

propagation state across the critical angle). For this reason, Eqs. (3.21) and (3.22) is convenient for plotting conceptual diagrams and Eqs. (3.19) and (3.20) are for analyzing detailed performance. It is noted in Eqs. (3.19) and (3.20) the values of E and V_0 are positive while in Eqs. (3.21) and (3.22) they are negative.

3.2.2.2 Two-dimensional model

The above derivation does not consider the shift Δy of lighwave in the y-direction (see Fig. 3.15(a)), which constitutes the one-dimensional model. A more accurate model is further developed by considering Δy, which is called the two-dimensional model.

A photon or an electron wave packet can be indicated as a superposition of corresponding plane waves. The average position where photon tunneled through the FTIR structure and its corresponding phase time could be obtained by comparison with the electron wave packet tunneling [81] and with the stationary-phase approximation [100]. The shift in the y direction, Δy, and the phase time t in the photon tunneling in Fig. 3.15 (a) are given by [82]

$$\Delta y = -\frac{c}{n\omega\cos\theta}\left(\frac{\partial\phi_t}{\partial\theta}\right)_\omega \tag{3.23}$$

$$\tau = \tau_0 + \tau_{\Delta y} = (\frac{\partial \phi_t}{\partial \omega})_\theta + \frac{n}{c}\Delta y \sin\theta \tag{3.24}$$

where ϕ_t is the phase of the complex transmission coefficient $\phi_t = \arg(t)$ for the one-dimensional electron tunneling of Fig. 3.15 (b); i.e

$$\phi_t = \arctan\{\frac{\cos^2\theta - n^2\left(n^2\sin^2\theta - 1\right)}{2n\cos\theta\left(n^2\sin^2\theta - 1\right)^{1/2}} \times \tanh\left[d\frac{\omega}{c}\left(n^2\sin^2\theta - 1\right)^{1/2}\right] \tag{3.25}$$

for the P-polarization photon tunneling. For the S-polarized photon tunneling, with m_2/m_1=1, we obtain [82]

$$\phi_t = \arctan\{\frac{n^2\cos^2\theta - \left(n^2\sin^2\theta - 1\right)}{2n\cos\theta\left(n^2\sin^2\theta - 1\right)^{1/2}} \times \tanh\left[d\frac{\omega}{c}\left(n^2\sin^2\theta - 1\right)^{1/2}\right] \tag{3.26}$$

If the incident photon wave packet peak approaches (x, y) = (0, 0) at time zero, then the optical intensity at (x, y) = (d, 0) can obtain a maximum at time $(\frac{\partial \phi_t}{\partial \omega})_\theta$, and the corresponding wave front, which is perpendicular to the wave propagation direction in the glass medium, propagates a distance $\Delta_y \sin\theta$ (see Fig. 3.15) with the speed c/n, to reach at (x, y) = (d, Δ_y) with another delay of $(n/c)\Delta_y \sin\theta$. [82] If Δ_y in the medium is considered and added to d, the results for single-barrier are shown in Fig. 3.16. It can be seen that, the transmittance spectra from the quantum interpretation and the nano-optics interpretation coincide very well during the whole period, except for the tiny difference existed as the tunneling gap is in the

range of 0.05-0.15 μm, which attributes to the different solution precision levels of the partial differential equations and could be neglected in the actual application. But the real physical origin of this difference needs further exploration. The feasibility of the PBM for exploring the FTIR structure has been successfully demonstrated.

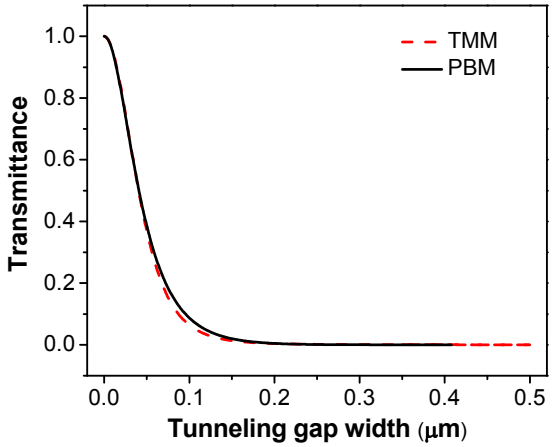

Fig. 3.16 The dependence of transmittance of the single-barrier structure on the tunneling gap calculated by using transfer matrix model (TMM) and potential barrier method (PBM).

3.2.3 Potential barrier model of resonant optical tunneling effect

The above quantum-optical analogical relationship is developed for the optical barrier structures, it can be utilized for the optical well structure (see Fig. 3.14(c)).

According to the corresponding relationship (Eqs. (3.19) and (3.20)), the ROTE optical system can be converted into the finite potential well of quantum mechanics as shown in Fig. 3.17.

On the input side, the wave function should have the form of

$$\psi_1 = Ae^{+jk_1x} + Be^{-jk_1x} \tag{3.27}$$

here x is the propagation direction, the terms Ae^{+jk_1x} and Be^{-jk_1x} represent the forward and backward waves, and thus the reflection is

$$R = \left|\frac{B}{A}\right|^2 \tag{3.28}$$

On the output side, the wave function takes the form $\psi_2 = Ce^{+jk_1x}$, and the transmission is given by

$$T = \left|\frac{C}{A}\right|^2 \tag{3.29}$$

The relationships between the constants A, B and C can be obtained by solving the Schrödinger equation in the finite potential well and by using the continuity conditions on the boundaries.

This model provides a direct explanation of the wavelength selection property of the ROTE structure. As shown in Fig. 3.17, the central part of the double potential barrier structure presents to be a finite quantum well and its supporting energy states are split. That is, only the photons with proper energies (equivalently, proper frequencies, see Eq. (3.19)) can pass through it.

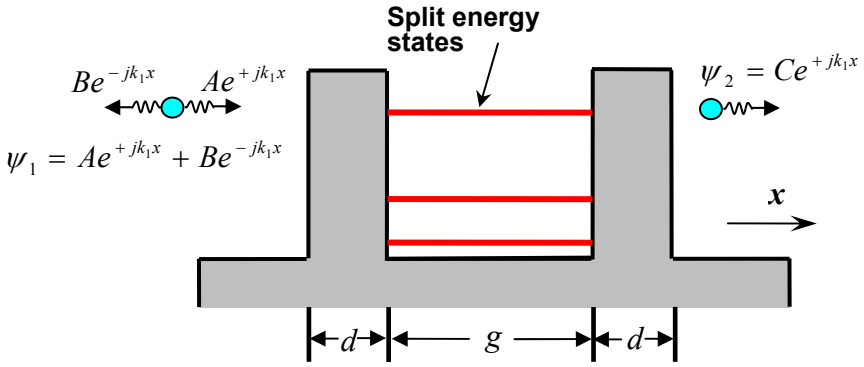

Fig. 3.17 Wave functions of a particle encountering a double potential barrier for the potential barrier model (PBM).

Table 3.1 The parameters of the multilayer structure explored by using the potential barrier model (PBM) and transfer matrix model (TMM).

Parameter	Symbol	Values
Tunneling gap	d	100 nm
Incident angle	θ	18.0^{o}
Refractive index of silicon	n_1	3.42
Refractive index of air	n_2	1.00
Wavelength of incident light	λ	500 nm
Tunneling gap	d	100 nm

For comparison, the same silicon-air multilayer structure (see Fig. 3.2) studied in the TMM is explored by using the PBM. The detailed parameters of the structure are listed in Table 3.1. The P-polarized transmittance of the structure as a function of the central slab width is shown in Fig. 3.18. For comparison, the transmittance of P-polarization of the same structure calculated in transfer matrix model (TMM) is also plotted. It can be seen that a series of sharp peaks of the

transmittance appear for both the PBM and the TMM. However, if the PBM curve is shifted by certain amount (offsets the difference in solution precision levels of the partial differential equations), it can be observed that these two curves have the same period (see Fig.3.18 (b)), and almost overlapped. As shown in Fig. 3.18(c), for individual peak, these two curves have the similar profile and nearly overlapped in the tip region. Consequently, the PBM could characterize some features of the ROTE structure (e.g. the periodically distributed peaks with the same period, high overlap of the single peak), and shows nice potential to be applied in the actual simulation. The study of PBM shows the different physical picture of the ROTE, and offers the possibility to avoid the complex transfer matrix calculation and obtain the transmittance (or reflectance) from directly calculating the split energy states of the whole structure, which has been well-developed in the electronics theory.

Although the PBM has some achievements for exploring the ROTE structure, it still needs to be further optimized. Similar with the parametric study carried out in the TMM (subsection 3.1), the dependence of transmittance on the parameters of the structure (e.g., the incident angle, the tunneling gap, and the wavelength) should be further explored. The achievements of these aims may present

fresh understanding of the ROTE. And the whole theoretical system based on the quantum-optical analogies will be built up for the actual calculations and simulations.

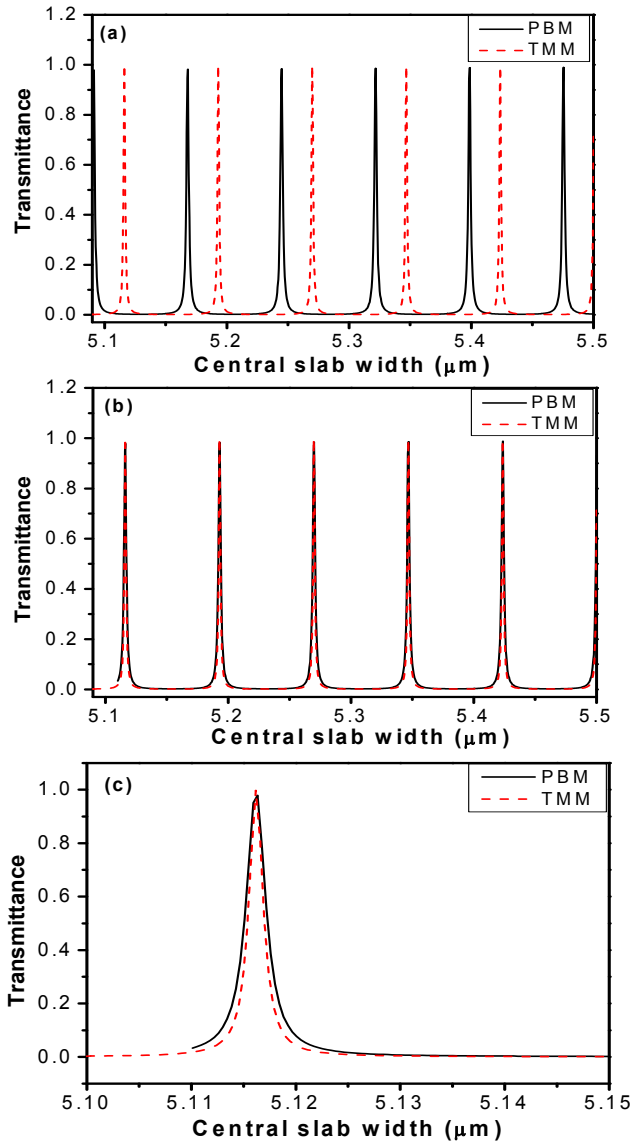

Fig. 3.18 The dependence of P-polarized transmittance of the multilayer structure on the central slab width calculated by using potential barrier method (PBM) and transfer matrix method (TMM) (a); the PBM curve is shifted to show that the PBM transmission curve has the same period as the TMM transmission curve (b); close-up to the single peak (c).

3.3 Summary

This chapter has developed the theoretical models of the ROTE based on the nano-optics interpretation and the quantum mechanics interpretation.

In the section of the nano-optics interpretation, the transfer matrix model is developed. The effects of four parameters, including the incident angle θ, the tunneling gap d, the central slab width g, and the incident wavelength λ are investigated separately. There is a maximum of transmittance for a specific set of parameters. And such maximum transmittance could be periodically reached in a relatively large value range. For different polarization states, the model has the similar characteristics but different sets of values. If only one of parameters, such as the incident angle, the central slab width and the incident wavelength, is changed in a relatively small region (within the period) while the other parameters are kept constant, the transmittance would vary dramatically, showing a sharp peak. For the tunneling gap, the variation of transmittance is complicate and the peak shifts to different directions for different polarization states. Generally speaking, the peak of transmittance in S-polarization state is much sharper than that in P-polarization state.

The quantum mechanism interpretation delivers a better physical picture of the ROTE. For this part, the analogical relationship between the tunneling photon and tunneling electron has been obtained using the single barrier structure. Based on that, the potential barrier model for the ROTE has been derived. Simulation results show that the transmittance curves from the quantum interpretation and the nano-optics interpretation share the same period and overlap well after a shift to compensate the phase difference.

Chapter 4 Design of Refractive Index Sensing Systems

The object of this chapter is to present the designs of RI sensors and to explore their possible RI sensing approaches. As one of well-known nano-optics mechanisms, the surface plasmon resonance (SPR) has attracted a lot research interests. In order to compare with the performance of the ROTE sensor, the design of RI sensor based on the SPR will be firstly presented in this chapter. Based on the physical understanding of the ROTE provided by last chapter, two designs of RI sensors, the microfluidic chip–based design and the angled optical fiber-based design, will be proposed. To estimate the sensitivity of this sensor, for each design, two approaches will be discussed: the intensity-based method and the spectrum-based method. The estimated sensitivity will also be compared with the prevailing methods such as the FP etalons and the SPR sensors.

4.1 Refractive index sensors based on surface plasmon resonance

4.1.1 Surface plasmon resonance sensor designs

Over past decades, optical sensors based on surface plasmon resonance (SPR) have been extensively studied due to its applications for analysis of biomaterials and environmental inspection. As introduced in chapter 2, when the SPR is excited, the absorption dip in the reflection spectrum is very sensitive to the RI change in the vicinity of metal surface. Comparing with the traditional prism-based SPR sensors, the optical fiber-based SPR sensors require very small volume of liquid sample for measurement. Furthermore, the optical fiber-based SPR sensors have simple structure and low cost, making them amenable for remote sensing applications.

As reviewed in chapter 2, various configurations of sensors using to different types of fibers and structures have been proposed by many researchers. [26-40] The most common configuration of optical fiber-based SPR sensor, which is based on Kretschmann method, is shown in Fig. 4.1(a). After removing the cladding part of the multi-mode fiber (usually by tapering the fiber), a metal layer is deposited

on the surface of the core. The spectrum of transmission is collected for RI sensing. It is easy to fabricate and integrate to other device, such as microfluidic chips. Because some DNA probes could be immobilized on the surface of the fiber, this senor is widely used to monitor the DNA molecule *in situ*. However, this design has a severe disadvantage that the incident angle is distributed from 75 deg to 90 deg, which broadens the SPR absorption valley and reduces the resolution of sensor. As the distribution of propagation modes in the multi-mode fiber are nearly random, the distribution of light beams at different incident angles is not stable, which further affects the repeatability of measurements. This is another disadvantage of this kind of sensor. To overcome the these drawbacks, a new design of optical fiber SPR sensor is proposed, which is shown in Fig. 4.1 (b). The single mode fiber with smaller number aperture (NA) is used to reduce the range of incident angle, which is closer to the theoretical model. The fiber tip is polished at the designed angle as the sensing probe, and a thin layer of metal is deposited on the polished surface. The reflection from the polished surface is collected for the measurement. Compared with the tapered SPR design with curved reflection surface, the flat surface could limit the spreading of the incident angle, thus the SPR absorption dip will be sharper.

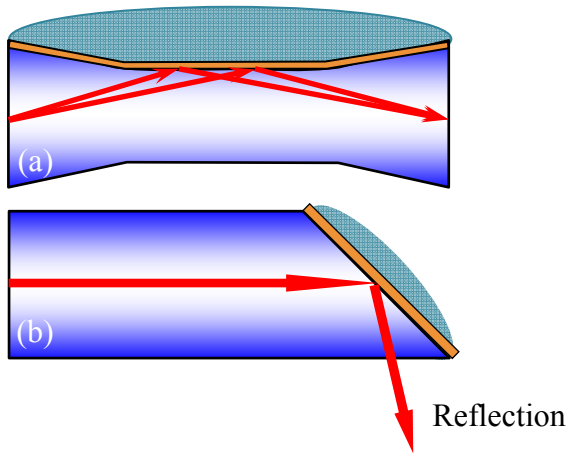

Fig. 4.1 The sensing elements of different designs of SPR sensors: (a) multi-mode fiber-based design, (b) angled single mode fiber-based design.

4.1.2 Performance analysis

In the transfer matrix model, the SPR sensor structure could be considered as a three-layer system (i.e., optical fiber-metal-analyte), which is shown in Fig. 4.2. Because the thickness of metal layer is very small (30-70 nm), the evanescent field could penetrate the metal layer and couple with the analyte. In the following simulation, the light is incident at an angle θ (complementary angle of the polished angle), and the thickness of metal layer is d.

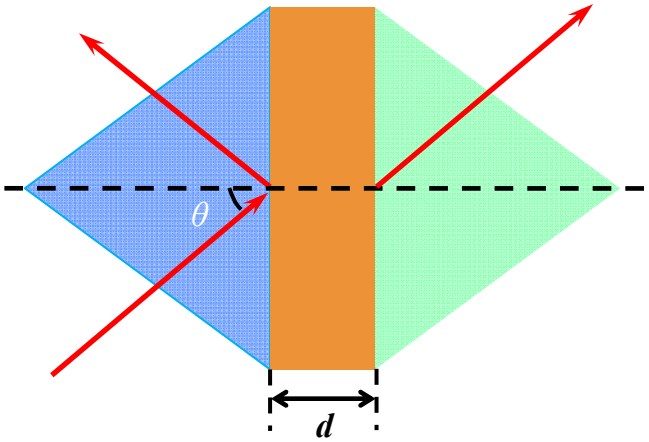

Fig. 4.2 Optical model of the angled fiber SPR sensor.

Figure 4.3 shows the contours of theoretical SPR reflection for air (RI=1.000 RIU) and water (RI=1.333 RIU). The metal used in simulation is silver, with a thickness of 50 nm (typical value for most developed SPR sensors). It is seen that the SPR reflection is strongly dependent on the incident angle and the incident wavelength. Cool colors in the figures correspond to the SPR absorption valleys. It is obvious that, in the two graphs, the absorption patterns in dark colors are not symmetrical in horizontal direction, so the absorption dip is quite different as the incident angle changes. In Fig 4.4, it can be observed that, as the incident angle decreased the SPR dips shifts towards the longer wavelength. Therefore, to get the sharp SPR valley, the incident angle should be strictly controlled in the experimental study.

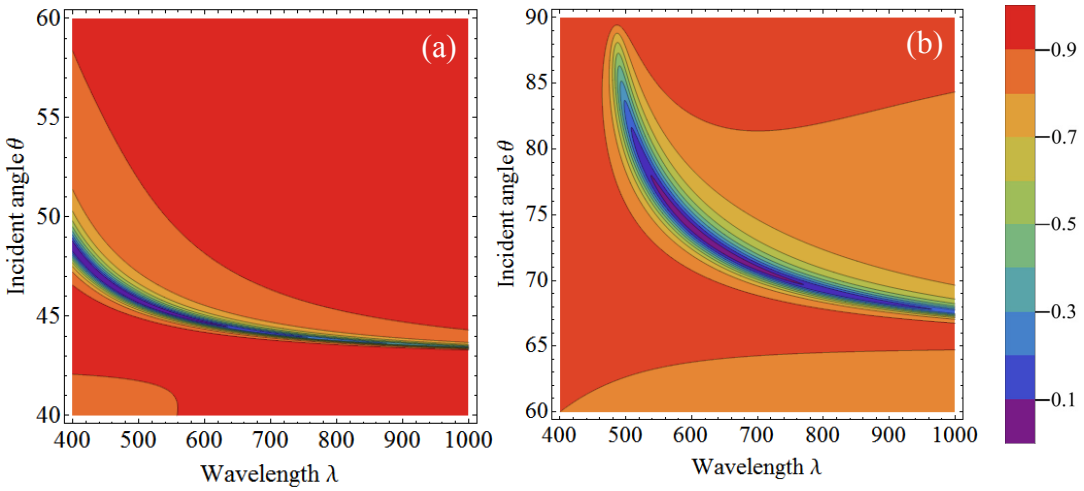

Fig. 4.3 Theoretical SPR spectra as a function of incident angle and incident wavelength for air (a) and water (b).

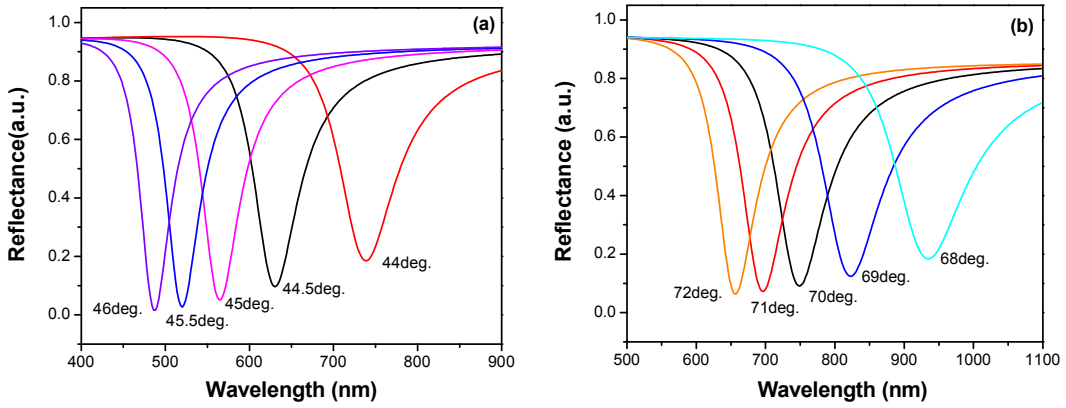

Fig. 4.4 Dependence of the SPR absorption dip shift on the incident angle for air (a) and water (b).

Based the angled fiber sensor design, the performance of the sensor is also predicted. The shift of the SPR absorption dip is shown in Fig. 4.5 as a function of the RI of analyte. When it is used as the gas sensor (RI is near 1.00 RIU), the

simulation results is shown in Fig. 4.5 (a). Here the active incident angle is 45 deg (the critical angle of silica/air is 43 deg), and the metal coating is 50 nm Ag. When the RI of surrounding gas is changed by 0.01 RIU, the SPR absorption valley is shifted by 25.5 nm, correspondingly the theoretical sensitivity of sensor is 2,550 nm/RIU. When it is used to detect the RI of liquid analyte (RI is around 1.33 RIU), the simulation result shown in Fig. 4.3 (b), the incident angle should be set at 70 deg (the critical angle of silica/air is 65 deg). As the RI of surrounding analyte changes from 1.33 to 1.34 RIU, the SPR absorption valley shifts from 727 to 810 nm. The theoretical sensitivity of sensor obtained is calculated to be 8,300 nm/RIU.

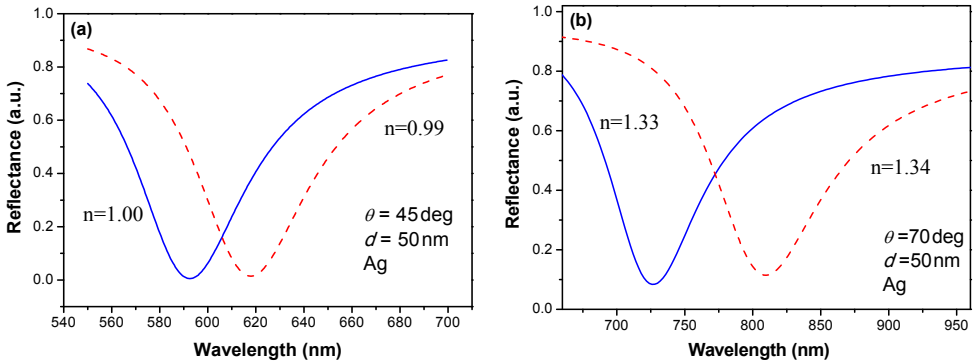

Fig. 4.5 The shifts of the SPR absorption dips when the angled fiber design in used for the RI sensor of (a) gas and (b) liquid analyte.

Wavelength shift (nm) per RIU is a common indicator for the sensitivity of RI sensor. However, in some cases this indicator is not perfect. Some RI sensing

methods (e.g., SPR) produce very large shift of transmission peak (or absorption dip) but the spectrum is broad and flat. This causes some difficulties in finding the accurate position of maximum (or minimum) value in the broad curve, especially in the presence of strong noise. For sensors with a broad spectral width, a parameter with more reference value is **detectivity**, which is defined as

$$\text{Detectivity} = \frac{\delta\lambda}{\delta\lambda_{0.5}} \cdot \frac{1}{\Delta n} = \frac{\text{Sensitivity}}{\delta\lambda_{0.5}} = \frac{\text{SNR}}{\Delta n} \tag{4.1}$$

where $\delta\lambda$ is the wavelength shift in response to the RI change of Δn, $\delta\lambda_{0.5}$ is the full width at half maximum (FWHM) spectral width of the spectrum. The detectivity is based on the parameter signal-to-noise ratio (SNR) proposed in some previous studies [37, 38]. The division by Δn is to normalize the influence of RI change and to facilitate the comparison among different data obtained under different conditions. For the SPR sensors designed above, the FWHM is about 57 nm (gas sensor) and 95 nm (liquid sensor), so the detecitivities for these two sensors are 45 RIU^{-1} for gas sensor and 87 RIU^{-1} for liquid sensor, respectively. The sensitivities and detectivities of SPR sensors for gas sensing and liquid sensing are listed in Table 4.1.

Table 4.1 Comparison of the surface plasmon resonance (SPR) gas RI sensor and liquid RI sensor in terms of sensitivity, FWHM (full width at half maximum) and detectivity.

	SPR gas sensor	SPR liquid sensor
Sensitivity (nm/RIU)	2,550	8,300
FWHM (nm)	57	95
Detectivity (RIU^{-1})	45	87

4.2 Refractive index sensors based on resonant optical tunneling effect

For sensing the RI of liquid analytes, two sensor designs are proposed to construct the ROTE structure and to handle the liquid. One is based on the microfluidic chip and the other is constructed by a pair of angled fibers.

4.2.1 ROTE refractometer using microfluidic chip

4.2.1.1 Concept and sensor design

The top view of the ROTE sensor design is shown in Fig. 4.6(a), which consists of two identical hemi-cylindrical prisms at two ends and a microfluidic channel in the

middle separated by two air tunneling gaps. The whole structure sits on a substrate and may be encapsulated by another top cover (not shown in the figure). The microfluidic channel has a central channel and two channel walls for the liquid sample to flow through. The structure of this sensor has seven layers in total. The design parameters of sensor are listed in Table 4.2. It is noted that the widths of the tunneling gap, the channel wall and the central channel are all normalized to the wavelength of incident light.

The optical model of the ROTE sensor is illustrated in Fig. 4.6 (b). The incident light hits the interface between the first prism and the air tunneling gap at an angle greater than the critical angle, tunnels across the air gap, and propagates through the microchannel. It then passes another gap and reaches the prism to form the transmission output. The symmetry of the structures ensures a high coupling efficiency from the input to the output. The liquid sample follows through the microchannel and becomes part of the resonant tunneling structure, thus its RI would affect the transmission.

The corresponding quantum model is shown in Fig. 4.6(c). According to the relationship between the RI n and the optical potential V (see subsection 3.2.2.1), the high RI parts (the prisms, the channel walls and the central channel) correspond to low optical potentials for the photons whereas the low index parts (i.e., the two air tunneling gaps) produce high optical potentials and thus the optical barriers. The resonance condition is highly dependent on the optical path length $L = n_3 g$, where n_3 is the RI of the central channel and g is the physical length of the central channel. Once the RI is changed, the resonance condition is broken, thus the transmission intensity will be reduced or the transmission peak will be shifted.

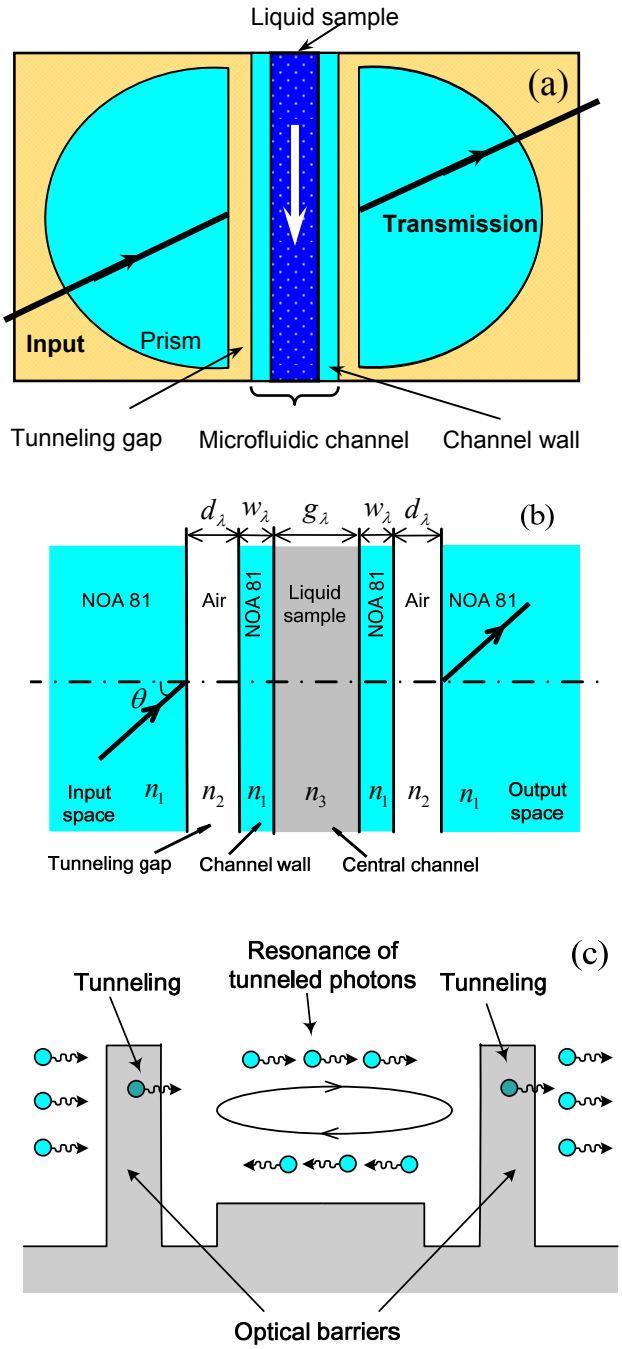

Fig. 4.6 Device design and theoretical models of the microfluidic RI sensor. (a) Top view of the sensor structure; (b) optical model of the sensor; and (c) equivalent quantum model of the sensor.

Table 4.2 Design parameters of the RI sensor based on the microfluidic chip.

Parameter	Symbol	Values	
		S-pol.	P-pol.
Normalized tunneling gap	d_λ	1.5000	1.5000
Incident angle	θ	42.0233°	42.0738°
Normalized channel width	g_λ	20.6350	20.7955
Normalized width of channel walls	w_λ	5.000	5.000
RI of prisms and channel walls	n_1	1.560	1.560
RI of tunneling gap	n_2	1.000	1.000

The microchannel structure can be fabricated by thiolene based resin NOA81 (Norland optical adhesive) instead of the widely-used mirofluidic material polydimethylsiloxane (PDMS). NOA81 has an elastic modulus three orders of magnitude higher than PDMS (typically 1 GPa) and could fabricate pressure resistant devices for the transport of complex fluids. [101] This avoids sagging effects, even for very low aspect ratio shallow channels. Moreover, NOA81 enables the replication of submicron features, low autofluorescence and biocompatible, which is suitable for the sensor application. The RI of NOA81 is 1.56 RIU from the datasheet. According to Table 4.2, if the D-line emission (wavelength 589 nm) is used as the light source, the width of central channel is larger than 12 μm with about 3 μm channel wall. The high processing precision of NOA81 ensures that the all the

design parameters could be achieved. A pair of single-mode optical fibers can be used for light input and output. The incident angle could be adjusted by high-precision micro-positioners.

From the above discussion, it can be seen that the seven-layer ROTE sensor is similar to the five-layer structure that was studied by the authors previously, which had two prisms, two air gaps and a central slab [95]. The difference is the previous study used only one central slab in the middle while the ROTE sensor has a three-layer microfluidic channel in the middle. This is because the ROTE sensor is designed for liquid samples, two channel walls have to be used to contain the liquid sample inside the central channel. As the liquid sample and the two channel walls have higher refractive indices than the air tunneling gaps, the whole microfluidic channel can be treated as a single layer. From this understanding, the combined effect of the central channel and the two channel walls is equivalent to the central slab in the previous study, and thus this seven-layer structure functions similarly to the previous fix-layer structure in term of the ROTE [95]. This point is also supported by the illustration in Fig. 4.6(c), the channel walls and the central channel produce low optical potentials and do not act as optical barriers to the photons.

4.2.1.2 Theoretical analysis of the sensor

To measure the RI using the ROTE sensor, there are two approaches: the intensity-based approach and the spectrum-based approach as briefly discussed in subsection 3.1.5. The former uses a single-wavelength laser as the light source and monitors the change of transmission intensity; and the latter utilizes a broadband light source as the input and monitors the shift of transmission peak. Detailed analyses of these two approaches will be presented below after a brief presentation of the analytical method.

a. Intensity-based refractive index sensing

This part will study the dependence of the transmission on the structural parameters and the RI change. The designed parameters as listed in Table 4.2. From Fig. 4.6(a) one can imagine that the liquid sample could flow through the central channel or the tunneling gaps. Therefore, it is necessary to study which one has better sensitivity to the physical size and the RI.

The transmissions of both S- and P-polarization are contoured in Fig. 4.7 with respect to the channel width and the tunneling gap. The bright region corresponds to high transmission. As can be observed in Fig. 4.7(a) and (b), a spike

of bright band appears upward for both P- and S-polarization. Near the spike, a small change of the central channel width would cause a large variation of the transmission (from bright to dark). However, with the change of the tunneling gap, the transmission is always in the bright region and thus does not vary that much. This shows clearly that the transmission is far more sensitive to the width of central channel than to that of tunneling gap. The transmission has different levels of dependence on the RI changes of different parts. Fig. 4.8 shows the contoured transmissions with respect of the RI changes of the central channel (Δn_3, the x axis) and the tunneling gap (Δn_2, the y axis).

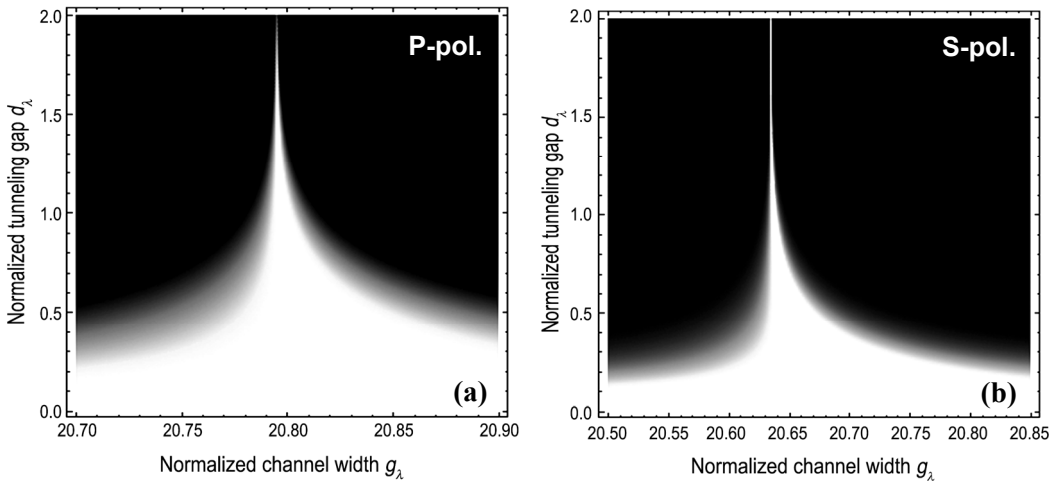

Fig. 4.7 Contours of the transmission with respect to the central channel width and the tunneling gap for P-polarization (a) and S-polarization (b).

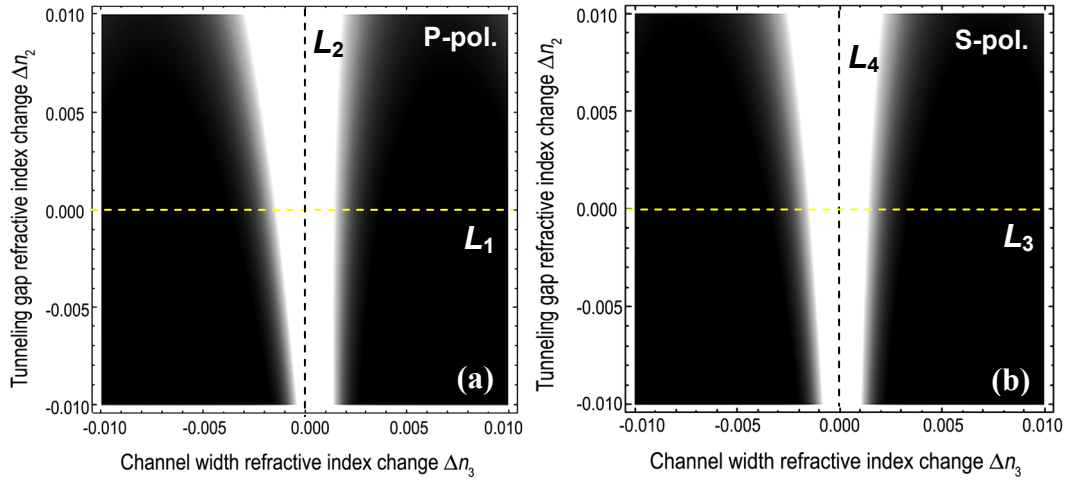

Fig. 4.8 Transmissions contoured with respect of the RI changes of the central tunnel channel and the tunneling gap for P-polarization (a) and S-polarization (b).

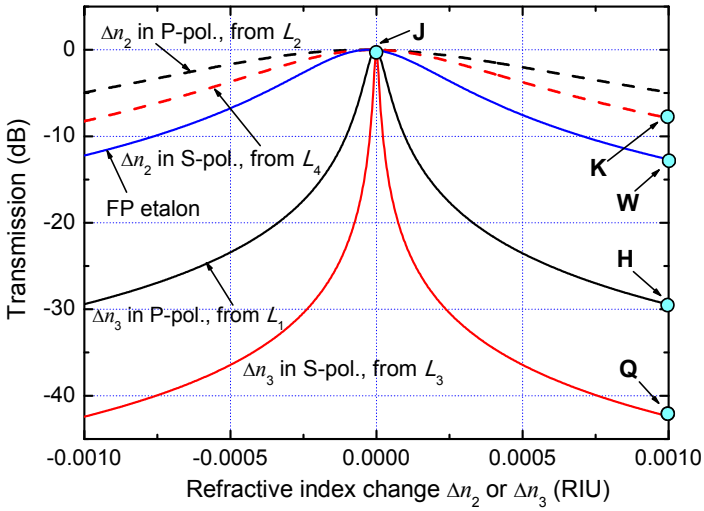

Fig. 4.9 Dependence of transmission on the changes of refractive indices of the central tunnel channel (Δn_3) and the tunneling gap (Δn_2) for P-polarization (black lines) and S-polarization (red lines). The curves are obtained from the observation line L_1 to L_4 in Fig. 4.8. For comparison, the transmission of a Fabry-Pérot (FP) etalon ($R = 0.95$) is also plotted.

Both contours have bright bands in the vertical direction. The transmissions vary more rapidly along the x axis than along the y axis for both P- and S-polarization, which suggests that the transmission is more sensitive to the RI change of the central channel than to that of tunneling gap. Quantitative comparison can be obtained by plotting the transmission curves along the observation lines L_1 to L_4 (see Fig. 4.8). The plotted results are shown in Fig. 4.9. It is easy to see that the transmission drops much faster with Δn_3 than Δn_2. At the initial state (point J), the transmission is at 0 dB (i.e., 100% transmission). For $\Delta n_3 = 1 \times 10^{-3}$ RIU, the transmission of the S-polarization state is reduced to -42.4 dB (point Q), while for $\Delta n_2 = 1 \times 10^{-3}$ RIU, it drops to only -8.3 dB (point K). Therefore, the transmission is over 1,000 times more sensitive to the RI change of the central channel than to that of the tunneling gap. For this reason, the liquid sample is designed to flow through the central channel rather than the tunneling gap.

The influence of the polarization state can also be derived from Fig. 4.9. Comparing the two curves of Δn_3 (those from L_1 and L_3), it can be seen that the S-polarization experiences a steeper drop of the transmission than the P-polarization. For instance, at $\Delta n_3 = 1 \times 10^{-3}$ RIU, the transmission is -42.4 dB for the S-

polarization (point Q) whereas it is only -29.3 dB for the P-polarization (point H). Therefore, the ROTE sensor can be > 10 times more sensitive when the S-polarization is used. For this reason, the analysis below will always use the S-polarization.

To show the ultra-high sensitivity of the ROTE sensor, the transmission variation of a Fabry-Pérot (FP) etalon with 95%-reflectivity mirrors is also plotted in Fig. 4.9. The length of the FP resonant cavity is 33.6λ, which is chosen to be the same as optical path length (OPL) of the ROTE region (i.e., channel's OPL + $2\times$(channel wall's OPL+ tunneling gap's OPL)). At $\Delta n_3 = 1 \times 10^{-3}$ RIU, the FP transmission drops to only -12.2 dB, three orders smaller than the drop of -42.4 dB in the ROTE sensor. As the etalons have already demonstrated a detection limit of 10^{-4} – 10^{-6} RIU [65], it is reasonable to expect the ROTE sensor to achieve an unprecedented level of detection limit up to 10^{-7} – 10^{-9} RIU.

The above analysis uses a single wavelength laser as the input and finds rapid drop of the transmission when the parameters of the central channel moves away from the designed values. Such intensity-based approach requires high fidelity of fabrication and strict control of experimental conditions (such as the initial RI of

the liquid sample, temperature, etc.), making it challenging in real implementation. Such problem could be circumvented by using a broadband light source as the input and then by observing the transmission peak. Because the dimensions of this ROTE sensor structure are normalized to the wavelength in the calculation, the broadband of light source can easily offset the fabrication error and the drift of experimental conditions by a shift of the transmission peak. In addition, it makes the experimental observation easier since there is always a peak in the output spectrum. More details are presented in the following part.

b. Spectrum-based refractive index sensing

Assume the incident broadband light has a central wavelength of 589 nm (D-line emission of a sodium lamp) and a bandwidth of 10 nm, the relationship between the peak shift and the RI change of the liquid sample in the central channel is plotted in Fig. 4.10. The inset shows the actual spectra correspond to the different RI of the liquid sample. The increase of the liquid sample RI causes a shift of the ROTE peak toward longer wavelength. The calculated sensitivity of sensor is 760 nm/RIU. With a high-resolution optical spectrum analyzer (0.01 pico-meter), the detection limit of

the ROTE senor could reach 1×10^{-8} RIU, roughly the same level as that of the intensity-based approach.

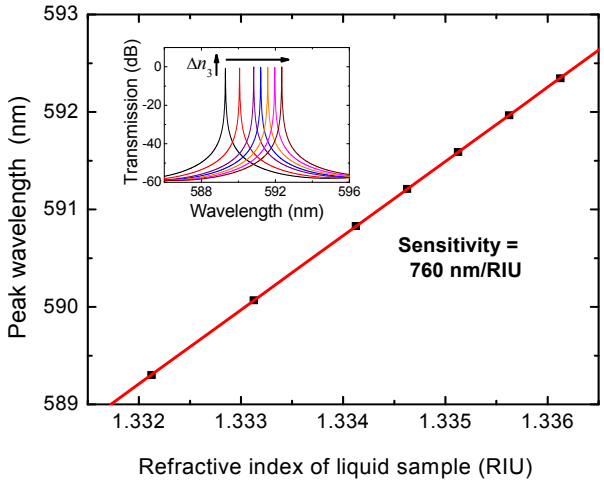

Fig. 4.10 Shift of the transmission peak wavelength with respect to the RI n_3 of the liquid sample in the central channel. The inset illustrates the shift of transmission spectra with the increase of the RI n_3.

Figure 4.11 compares the spectra of the ROTE sensor with the FP etalon and the SPR sensor. The latter two have been well established for high-sensitivity RI measurement. The parameters of FP etalon are the same as mentioned above. The SPR spectrum is the simulation result in the subsection 4.1.1. The SPR sensor utilizes a 50-nm thick silver thin film coated on the surface of NOA81 and has the incident light entering at 70 degrees. After shift, the SPR absorption dip is plotted together with the FP interference pattern and ROTE transmission spectrum. It can be

seen from Fig. 4.11 that the ROTE sensor has much narrower spectral width than the FP etalon and the SPR sensor. The sensitivities and the detectivities of different sensors are listed in Table 4.3. In term of sensitivity, the SPR has the largest sensitivity of 8,300 nm/RIU, about 11 times of the ROTE sensitivity (760 nm/RIU) and 19 times of the FP etalon sensitivity (440 nm/RIU). Nevertheless, in term of detectivity, the ROTE sensor obtains 85,000 RIU^{-1}, which is 85 times larger than the FP etalon (1,000 RIU^{-1}) and 977 times larger than the SPR sensor (87 RIU^{-1}). This comparison gives great confidence that the ROTE sensor can achieve an unprecedented sensitivity of RI measurement.

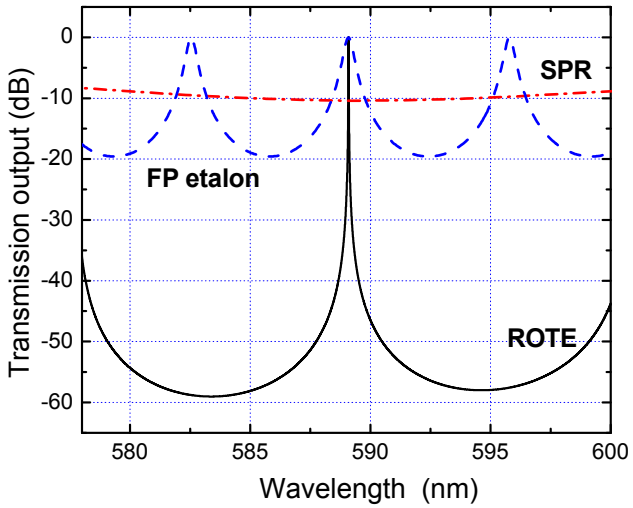

Fig. 4.11 Comparison of the transmission spectrum of the ROTE sensor with the transmission spectrum of the Fabry-Pérot (FP) etalon and the reflection spectrum of surface plasmon resonance (SPR) sensors. The latter two are widely used for highly-sensitive RI sensing.

Table 4.3 Comparison of the sensitivity and detectivity of the resonant optical tunneling effect (ROTE) sensor based on microfluidic chip, the Fabry-Pérot etalon and the surface plasmon resonance (SPR) sensor.

	ROTE sensor*	FP etalon (R = 95%)	SPR sensor
Sensitivity (nm/RIU)	760	440	8,300
FWHM (nm)	0.0089	0.44	95
Detectivity (RIU^{-1})	85,000	1,000	87

* The ROTE sensor based on microfluidic chip.

4.2.2 ROTE refractometer using angled fibers

4.2.2.1 Concept and sensor design

The structural design of the fiber-based ROTE sensor is shown in Fig. 4.12(a). Two single-mode optical fibers (input and output fibers) are polished with certain angle and then coated with silver. They are separated by a small gap, in which the liquid sample is filled in. In this way, the liquid sample becomes part of the resonant optical tunneling structure. In total, this sensor has five layers: the input fiber, the silver layer, the liquid sample, another silver layer and the output fiber. Although the silver layers introduce some loss due to the absorption of light, it can be alleviated by using very thin silver films (10 – 30 nm). The design parameters are listed in Table 4.4. It is noted that the tunneling gap width (i.e., the silver layer thickness) and the

cavity width (i.e., physical separation of fibers) are all normalized to the wavelength of incident light.

The optical model of the ROTE sensor is illustrated in Fig. 4.12 (b). The incident light hits the interface between the input fiber and the thin silver layer at an angle greater than the critical angle, tunnels across the silver tunneling gap, and propagates through the central cavity. It then tunnels across another silver layer and reaches the output fiber to form the transmission output. As the diameter of fiber core is only 8 μm and the central cavity width is about 15 μm, the minimum amount of the liquid sample is only about 4 pico-litre. Such a low volume requirement is of significance for the applications in which the sample liquids are rare or expensive.

The corresponding quantum model is shown in Fig. 4.12(c). According to the relationship between the RI n and the optical potential V (see subsection 3.2.2.1), high RI media (i.e., optical fibers, liquid sample) correspond to low optical potential for the photons, while low RI parts (i.e., silver layers) produce high optical potential and act as optical barriers. Based on this model, the photons resonate between the two optical barriers and generate a series of resonant modes. The change of RI of liquid sample results in a variation of the path length of the optical cavity $L = n_3 g_\lambda$

(where n_3 is the RI of the liquid sample, g_λ is the normalized physical length of the optical cavity) and the change of resonant condition, thus the transmission intensity will be altered.

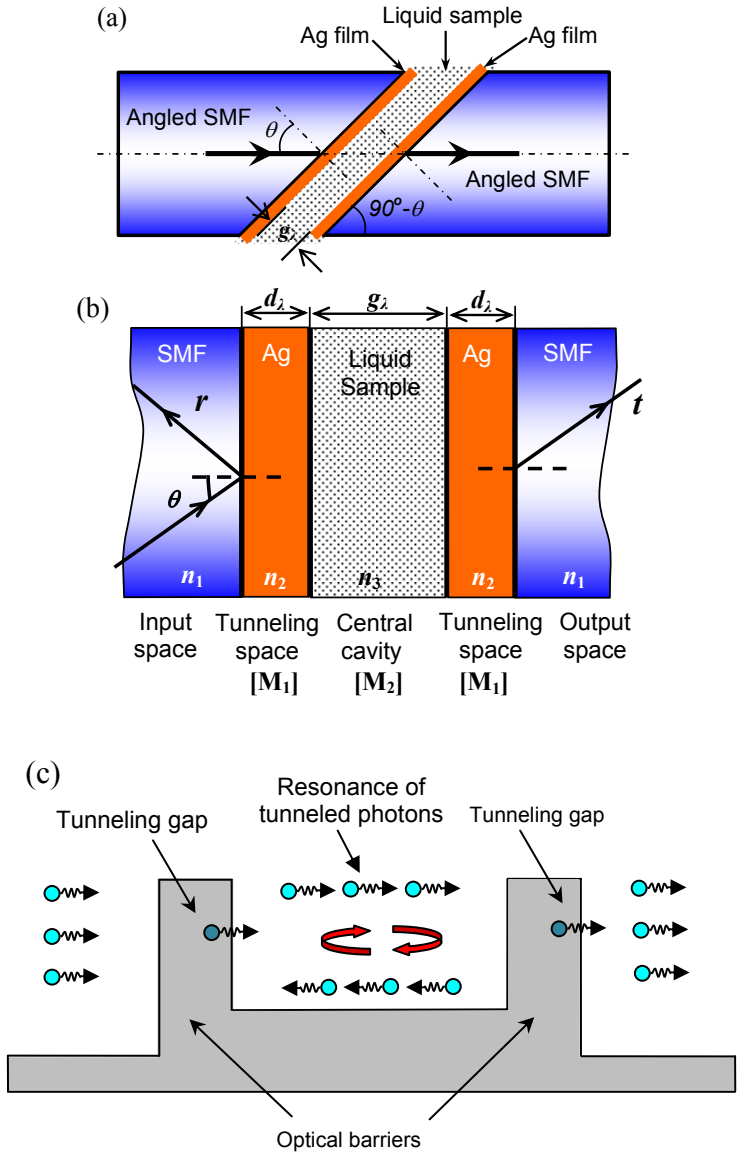

Fig. 4.12 Device design and theoretical models of the RI sensor based on resonant optical tunneling effect. (a) Schematic diagram of the sensor structure; (b) optical model of the sensor; and (c) equivalent quantum model of the sensor.

4.2.2.2 Theoretical analysis of the sensor

The theoretical model for this sensor can be developed using the transfer matrix method (TMM) [85]. Similarly, both the intensity-based approach and spectrum-based approach will be discussed. The estimated sensitivity will also be compared with the FP etalon and the SPR sensor as well.

This part will study the dependence of transmission on the structural parameters and the RI change. Firstly, the five-layer structure model is investigated and the design parameter of IR sensor is determined. The dependence of the transmission on the cavity width (i.e., liquid sample) and the tunneling gap (i.e., silver layer) is contoured in Fig. 4.13. The bright region corresponds to high transmission. As shown in Fig. 4.13, a spike appears upward in either S-polarization or P-polarization. Transmission band narrows down and the transmission intensity drops as the tunneling gap increases. It can be seen that in the spike region a small change of central cavity width would cause a large variation of the transmission intensity (from bright to dark). This is true for both S- and P-polarization. In contrast, in the spike the intensity does not change that much with the increase of the tunneling gap. Therefore, the transmission is far more sensitive to the central cavity

width than to the tunneling gap. Because the change of RI has the same effect as the change of physical length, the transmission is more sensitive to the RI change in the central cavity. This is why the sensor design chooses to hold the liquid sample between the two silver layers. This finding is the same as that in the microfluidic chip-based ROTE sensor (see subsection 4.2.1.2), in which the transmission is more sensitive to the RI change of the central channel than that of the tunneling gap. Moreover, the low sensitivity to the tunneling gap is beneficial since it loosens the requirement for the control of silver layer thickness. By balancing the sensor sensitivity and transmission intensity, the design parameters of the sensor are chosen as listed in Table 4.4.

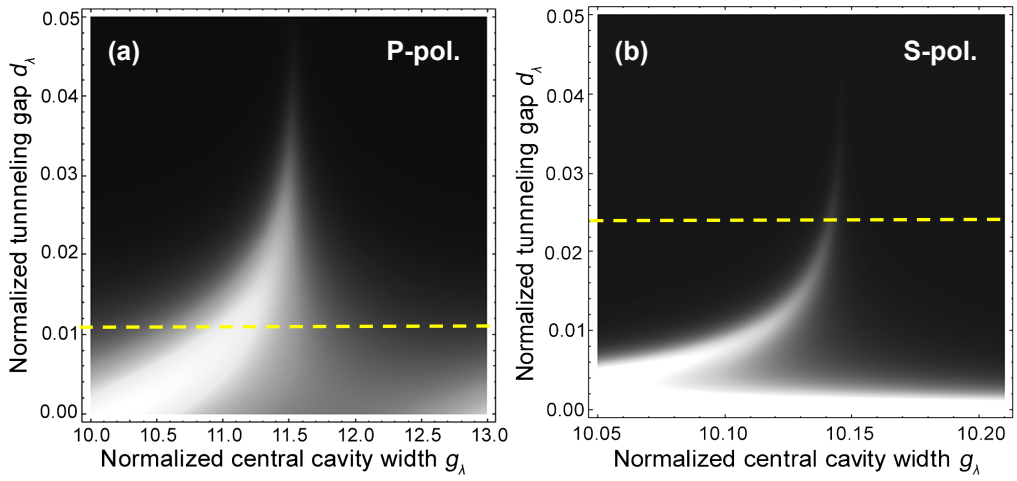

Fig. 4.13 Contours of the transmission as functions of the central cavity width and the tunneling gap. (a) P-polarization and (b) S-polarization.

Table 4.4 Design parameters of the RI sensor based on the angled fibers.

Parameter	Symbol	Values	
		S-pol.	P-pol.
Normalized tunneling gap	d_λ	0.011	0.026
Normalized cavity width	g_λ	10.120	11.450
Incident angle	θ	63.0^o	
RI of fiber	n_1	1.4677	
RI of Ag layer	n_2	0.37 –j8.632	
RI of liquid sample	n_3	1.316	

a. Intensity-based refractive index sensing

The transmission intensity as a function of the RI change of the central cavity Δn_3 is plotted in Fig. 4.14 for both P- and S-polarization. The curves correspond to the observation lines in Fig. 4.13. It can be seen that transmission intensities are strongly dependent on Δn_3, and the transmission curve of S-polarization is significantly steeper than the P-polarization curve. In the initial state, maximum transmission is obtained as indicated by the point *N*, which is about -5 dB due to the absorption of silver layers. When Δn_3 is changed by 1×10^{-3} RIU, the transmission drops to point *Q* (-17.5 dB) and *R* (-37.5 dB) for S- and P-polarization, respectively. It shows S-polarization is more sensitive than P-polarization. For this reason, S-polarization is used in further discussion. For comparison, the transmission variation of a FP etalon is also plotted in Fig. 4.14, which decreases by about -9 dB when subjected to the

same amount of RI variation. The transmission change of the ROTE sensor is about 1,000 times larger than that of the FP etalon, implying the ROTE sensor is more sensitive as compared to the FP etalon. Here the FP etalon has same cavity width with the ROTE sensor and is formed by two 95%-reflectivity mirrors. As the etalons have already been demonstrated a detection limit of 10^{-4} – 10^{-6} RIU [65], it is reasonable to expect the ROTE sensor offers a detection limit level up to 10^{-7} – 10^{-9} RIU. Again, these features of the higher sensitivity for S-polarization and the 1,000 times more sensitive than the FP etalon are the same as these in the microfluidic chip based design.

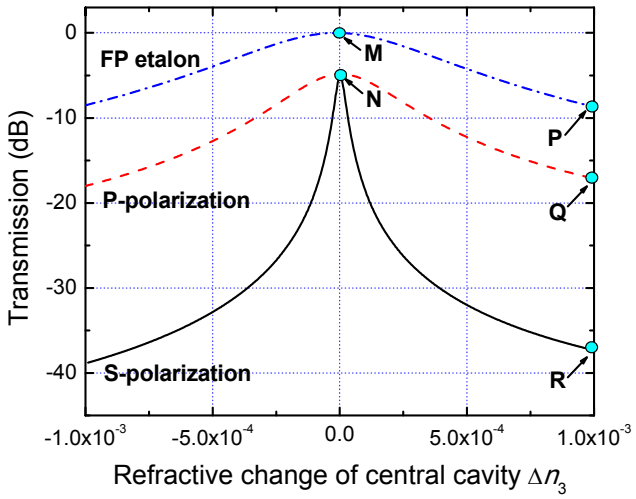

Fig. 4.14 Variation of the transmission in response to the change of RI of the central cavity Δn_3 for P-polarization (solid line) and S-polarization (dashed line). For comparison, the transmission of a Fabry-Pérot (FP) etalon (R = 0.95) is also included.

b. Spectrum-based RI sensing method

In this method, a broad band light source with a center wavelength of 1310 nm and a spectral range from 1200 to 1450 nm is used as the light source. As shown in Fig. 4.15 and the inset, the increase of the liquid sample RI causes a red shift of the ROTE peak and a linear relationship is present. The sensitivity of sensor obtained is as high as 81,000 nm/RIU. As the resolution of optical spectrum analyzer could reach 0.01 pico-meter, the sensor could offer a detection limit of 1.2×10^{-10} RIU in an ideal case.

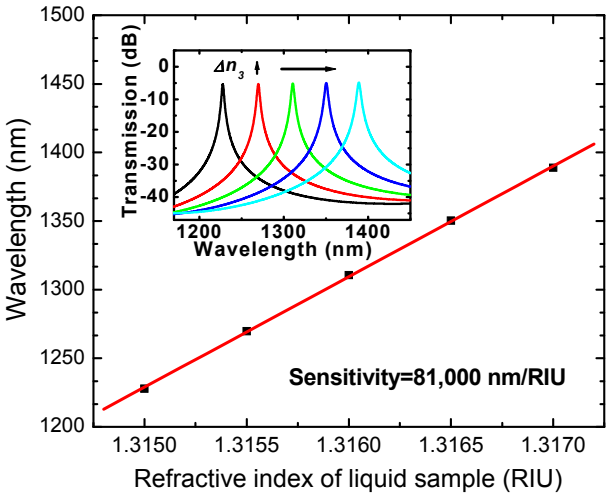

Fig. 4.15 Wavelength of the transmission peak as a function of the RI n_3 of the liquid sample in the central cavity. The inset illustrates the shift of transmission spectra with the increase of the RI n_3.

Figure 4.16 compares the spectra of the ROTE sensor with the FP etalon and the SPR sensor. The latter two have been well established for high-sensitivity RI measurement. The cavity length and the mirror reflectivity of the FP etalon are the same as used in Fig. 4.14. The SPR spectrum is from the sensor for liquid sensing designed in section 4.1 in this chapter, and artificially shifts to the region of Fig. 4.14.

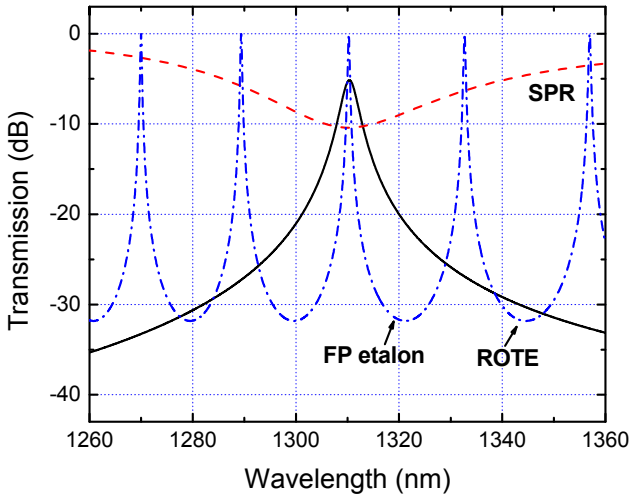

Fig. 4.16 Comparison of the transmission spectrum of the ROTE sensor with the transmission spectrum of the Fabry-Pérot (FP) etalon and the reflection spectrum of surface plasmon resonance (SPR) sensor. The latter two are widely used for highly-sensitive RI sensing.

Table 4.5 lists the sensitivity, the FWHM and the detectivity of two designs of ROTE sensors as compared with the FP etalon and the SPR sensors. It is noted the FP etalon has the same OPL with the angled-fiber ROTE sensor and thus the

performance is different from that in Table 4.2. It can be seen from Table 4.5 that the sensitivity of the ROTE sensor is much larger than the other two methods. More specifically, it is 184 times larger than that of the FP etalon and about 10 times larger than that of SPR sensor. In term of the FWHM, the FP etalon is the narrowest and the SPR sensor is over 30 times broader than the ROTE. In term of the detectivity, the ROTE sensor is again the best, about 20 times of that of FP etalon and 310 times of that of SPR. The simulation results demonstrate that the ROTE sensor has both ultrahigh sensitivity and considerable detectivity, making it promising for liquid RI sensing.

Table 4.5 Comparison of the resonant optical tunneling effect (ROTE) sensor, the Fabry-Pérot etalon and the surface plasmon resonance (SPR) sensor in terms of sensitivity, FWHM (full width at half maximum) and detectivity.

	The ROTE sensor based on the angled fiber	The ROTE sensor based on microfluidic chip	FP etalon (R = 95%)	SPR sensor
Sensitivity (nm/RIU)	81,000	760	440	8,300
FWHM (nm)	3.0	0.0089	0.35	95
Detectivity (RIU^{-1})	27,000	85,000	1,300	87

By changing the parameters of the ROTE structure, there are several ways to improve the sensitivities of the ROTE sensors. For typical ROTE structure sensor

design, from the simulation results obtained in Chapter 3, the larger incident angle, the sharper the ROTE transmitted peak will become, thus the sensor will have higher sensitivity. Similarly, if the tunneling gap of the TORE structure is larger, the central slab width *g* dependent transmittance will be sharper, which indicates the sensitivity of the sensor will be higher. Furthermore, as both designs use the central slab region for the liquid sensing, of which the change of the OPL (Δl) can be expressed as $\Delta l = l \times \Delta n$ (l and Δn are the length and the RI variation of OPL of the central slab width, respectively). For the same variation of RI, the larger change of OPL could be obtained if the central slab width is longer. As the OPL will finally affect the transmission, if other parameters are same, the sensor structure with larger central slab width will have a larger sensitivity.

It is hard to make the similar sensor designs have the same performance. Due to the absorption of metal layers, the tunneling gap of angled fiber-based design (metal layer) cannot be too thin so that the transmitted power is detectable. Thus the width of transmitted peak in angled fiber design is larger than that in in the microfluidic design. And the angled fiber-based design has lower detectivity value than the microfluidic chip-based design. On the other hand, the incident angle of

angled fiber-based design is 63 deg, which is far beyond the critical angle (about 17 deg). Its angle difference is much larger than that in the microfluidic design, which is only 2 deg larger than the critical angle (about 40 deg). Therefore, the angled fiber based design presents higher sensitivity compared with the microfluidic-based design. To achieve the best performance of the sensor, all the parameters obtained in this chapter have been comprised and optimized.

4.3 Summary

In this chapter, two designs of ultra-sensitive RI sensors have been proposed based on the ROTE, and their performances have been analyzed and compared with two prevailing RI sensors such as the FP etalon and the SPR sensor.

First, the SPR sensor has been investigated briefly to find the working conditions of incident angle and light wavelength. To achieve the sharper SPR dip, a new design has been demonstrated, using the angled single mode fiber tip instead of the multi-mode fiber decladding. According to the simulation results, the obtained sensitivities are 2,550 nm/RIU for the gas RI sensing and 8,300 nm/RIU for the liquid RI sensing. Sometimes, the rather large spectral width makes it difficult to

find the accurate position of a broad peak (or dip). Therefore, besides the sensitivity, another parameter *detectivity* has been proposed to take into the consideration the spectral width of the peak (or dip). This facilitates a fair comparison of the performances of different types of sensors.

To break the current detection limit barrier of 10^{-7} RIU, two models of ROTE sensors, microfluidic chip-based design and angled optical fiber-based design have been proposed. For each type of design, two independent sensing methods, the intensity-based method and the spectrum-based method, are suggested to retrieve the RI change of liquid samples. In case of the intensity-based method, as the transmission change of the ROTE sensors are about three orders larger than that of the FP etalon, the ROTE sensors achieve an unprecedented level of detection limit up to 10^{-7} – 10^{-9} RIU for both designs. For the spectrum-based method, the sensitivity of microfluidic chip-based sensor could achieve 760 nm/RIU. As to the angled optical fiber-based sensor, the sensitivity expected to reach 81,000 nm/RIU, which corresponds to 1.2×10^{-10} RIU in an ideal case. The comparison between these two ROTE designs shows that the microfluidic chip based design provides better detectivity whereas the angled fiber based design exhibits higher sensitivity.

Furthermore, theoretical study shows that the ROTE sensors have much higher detectivity than the well-established methods such as Fabry–Pérot etalons and SPR sensors. With the merits of ultrahigh sensitivity, fiber integration and small sample volume, the ROTE sensors could find potential applications in biomedical studies.

Chapter 5 Experimental Investigation and Results

The experimental issues will be elaborated in this chapter, which includes the fabrication and characterization of the sensors. The designs proposed in the previous chapter will be demonstrated in this chapter.

Compared with the microfluidic chip based design, the angled optical fiber design has higher sensitivity and thus is chosen to be fabricated. To realize this design, the fabrication process of sensors will be presented. The polishing method for the angled optical fibers will be shared in the chapter. The uniform metal layer, of which the thickness could be strictly adjusted, is also very important for the sensor performance. Thus the processing of metal layer deposition will be presented in this chapter as well.

In the experimental studies, the SPR sensor and the ROTE sensor, both are based the angled fibers will be characterized. For the SPR RI sensor, the responses of different analytes with different refractive indices will be measured. For the ROTE sensor, the effects should be verified, before the sensor characterization. The

experimental results will then be analyzed and compared with the results of the theoretical study.

5.1 Fabrication of refractive index sensors

5.1.1 Fiber polishing

For both the SPR sensor and ROTE sensors, the angled fiber tip is used as the sensing probe. Fiber polishing is the first step in the sensor fabrication. As the sensing signal is sensitive to the incidence angle, the polished angle should be well controlled. Meanwhile, the polished surface should be smooth enough so that the light will not scatter on the polished surface.

In this work, the polishing of fiber is accomplished by the Fiber Lensing Machine (Ultra Tec Manufacturing. Inc.) shown in Fig. 5.1. It is a powerful instrument for producing accurate end profiles on the bare optical fiber, of which the angular accuracy could reach 0.1 deg in the region from 20 deg to 180 deg.

Fig. 5.1 ULTRAPOL fiber lensing machine (picture from the website of Ultra Tec Manufacturing, Inc.).

The typical procedures of polishing optical fiber are listed as follows:

(1) Prepare the sample. The bare fiber (SMF28, Corning) is spliced and the length of exposed cladding part should be 1-2 mm. For some large angle (≥ 65 deg), to alleviate the fiber bending during polishing and to enhance the strength of optical fiber, the fiber without the buffer layer is slipped through a capillary (Polyimide tube) with little larger diameter (304 μm) and fixed using the photoresisit (Injectorall Positive Photoresisit). The process flow of sample preparation is shown in Fig. 5.2.

(2) As a layer of photoresist can protect the side wall of polishing surface and avoid break the corner of the fiber tip, the row of fiber tips is lightly dipped in the photoresist and heated for several minutes for solidification. Then the sample is glued on the holder of the polishing machine by using double faced adhesive tape.

(3) Start the rotating plane. The grid of the first polishing paper is 8 μm. The fiber is polished to form the angled end face. Feed the holder in 20 μm in every 20 seconds and sprinkle some water on the polishing paper to remove the grinded small particles.

(4) When the angled fiber tip is formed roughly, stop the rotating plane. Check the polished surface in a handhold microscope. If there are obvious defects on the polished surface, repeat the last step, until the surface is very flat and has no any obvious defects.

(5) Replace the used polishing paper (grid size 8 μm) using a fine polishing paper (0.3 μm grid). The purpose of this step is to smoothen the surface. The holder maintains the former position, and the polished surface should be checked time to time. Typically, the polishing time of this step is less than 30 seconds. However, the polishing time could be reasonably prolonged based on the observation of the polished surface.

(6) Release the optical fiber from the holder and clean the tip using the ultrasonic cleaner for 20 seconds. Use acetone and ethanol, to resolve the photoresist and then de-ionized (DI) water to clean the polished fiber tip.

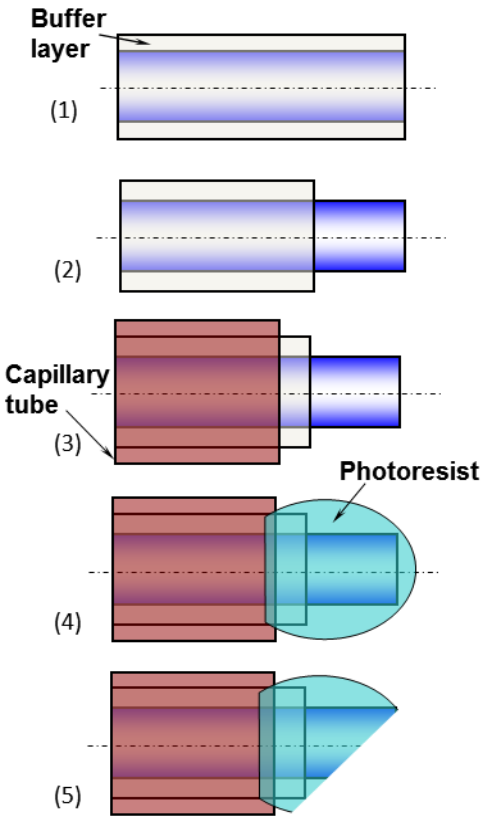

Fig. 5.2 Process flow of the sample preparation for fiber polishing.

There are some tips for getting smooth polished surface:

(1) Good alignment. The optical fiber should be perpendicular to the polishing plane.

(2) Carefully cleaning the polish paper before polishing.

(3) Repeating step (5) is important to get the smooth surface.

Fig. 5.3 presents the photos of the profile and the polished surface of the fiber tips in different angles (45 deg and 20 deg). The profile of the tips shows that the polished angle is sharp and the shining reflection qualitatively indicates that the polished surface is very smooth.

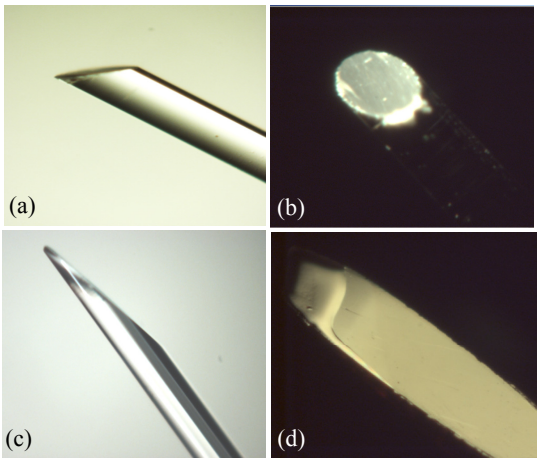

Fig. 5.3 Photographs of the polished optical fibers. (a) and (b) are for 45 deg. (c) and (d) are for 20 deg.

The polished surface is observed in a 3-D profilometer (TMS-1200 Top Map μ.Lab, Polytec), and the topography of the polished surface is shown in Fig. 5.4 (a). It can be seen that the overall surface is very flat. Except for a few pits around the rim of the plane, the surface does not have obvious defects all over the area. Although the edge of the fiber end is not as smooth and regular as the central area, it will not affect the light reflection/transmission because it is far from the core of the optical fiber. the profile along the observing line is presented in Fig. 5.4 (b). It shows that the central area is 200-300 nm higher than the edge part. And the fluctuation of central area of the surface (core of optical fiber) is less than 100 nm across the length of 100 μm, which is qualified for the wave-optic application.

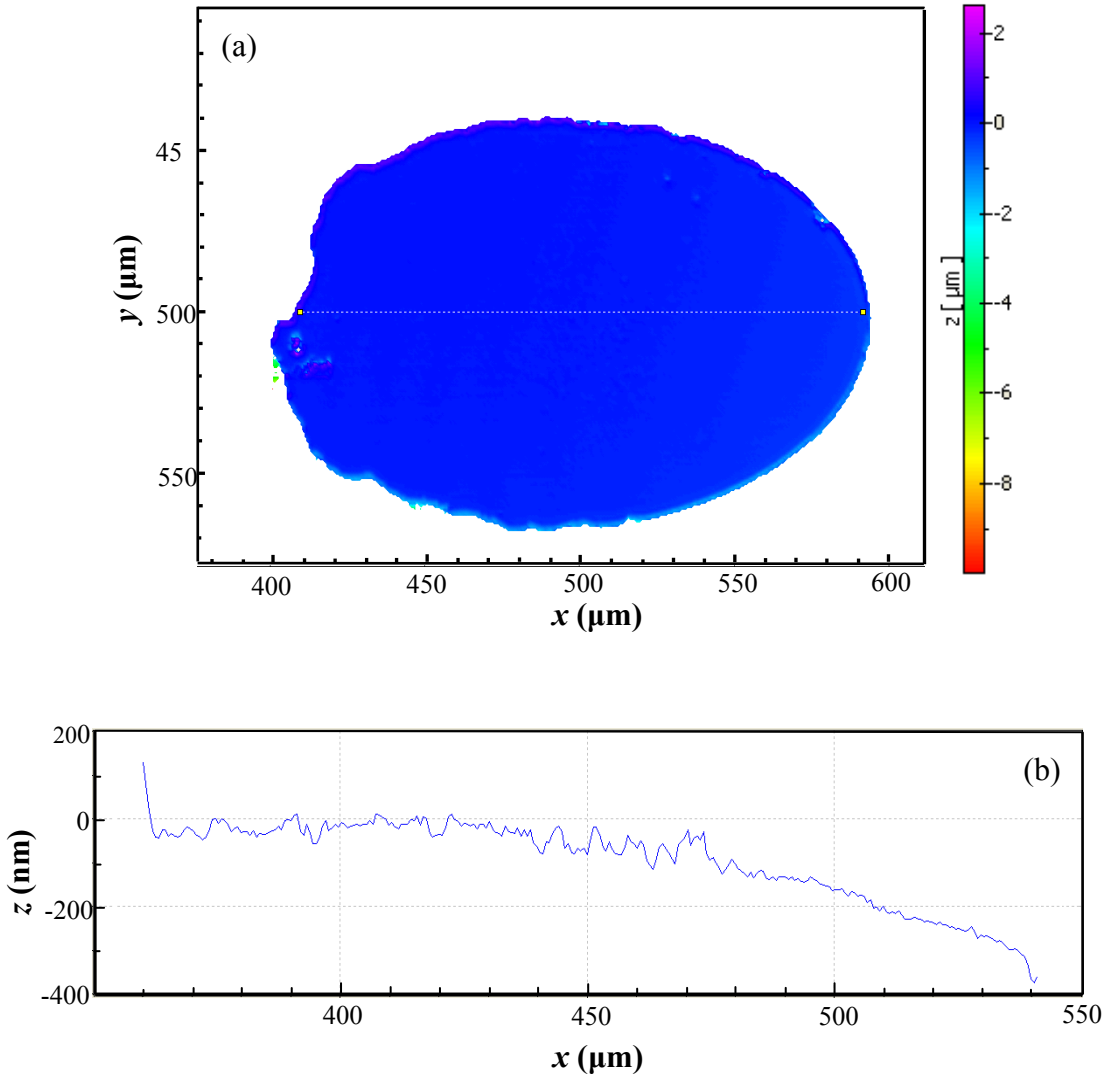

Fig. 5.4 The polished surface of the optical fiber. (a) The altitude map of the polished surface; (b) the height profile of the optical fiber surface.

5.1.2 Metal deposition

The quality of metal layer is critical to the performance of the photonic devices. As the metal layer is very thin, it should be as uniform as possible to reduce the possible thickness error in the fabrication process. With the booming of nanotechnology in last decades, various metal layer deposition technologies have been developed, including magnetic sputtering, thermal evaporation, electron beam evaporation and pulsed laser evaporation. Each method has its own characteristics for specific applications. For the magnetic sputtering, the formed metal layer has good crystalline quality and could firmly adhere to the substrate, but its deposition rate is too fast to control the thickness of the metal film in nanometer level. Thus, if the tolerance of thickness of metal film is at the level of ± 10 nm, such as the SPR sensor, it can be used for the metal film deposition. However, for some applications (such as the ROTE sensor), the signal of senor is ultra-sensitive to the thickness of metal film, and the thickness is more important than the quality of metal film. In that case, the thermal evaporation system, of which the deposition rate could be as low as 0.1 nm and the thickness of metal film could be monitored in the real time, is utilized in the experiment for the ROTE sensor.

It is noted that the silver is used as the material of tunneling barrier in the previous simulation study (see sub-section 4.2.3). However, as we are unfortunately short of the silver target for the thermal evaporation, the gold is utilized instead of silver. Furthermore, as silver is apt to react with the sulfur widely distributed in the open environment, the generated silver sulfide will further affect the performance and life time of the sensor. Compared with silver (RI = 0.37+ j8.632, λ = 1310 nm), the replacement of gold (RI = 0.414+j8.365, λ = 1310 nm) will not cause significant difference to the simulation results.

5.2 Refractive index senor based on surface plasmon resonance

5.2.1 Experimental setup

A commercial communication fiber (Corning SMF-28e) is polished in 20 deg (the incident angle for propagating light beam is 70 deg), and is coated with 50 nm Ag using the magnetic sputtering. After the fabrication, the next step of the work moves to the characterization of the sensor. The spectral response is measured with respect to the RI change of the surrounding medium. The experimental setup is shown in Fig.

5.5. Because the SPR characteristic absorption peak is very broad (80-200 nm), a halogen lamp (NAVITAR, 150W) is used as the broad band light source. The intensity of P-polarization and S-polarization light is nearly equal in this light source. As only P-polarization light could excite the SPW, only nearly half of the power is involved in the SPR. In the experimental setup, the light beams from the broadband light source are coupled into a single mode fiber by an objective lens are reflected on the metal coating of the angled fiber, and are finally collected by a spectrometer. The photographs of experimental setup are shown in Fig. 5.6.

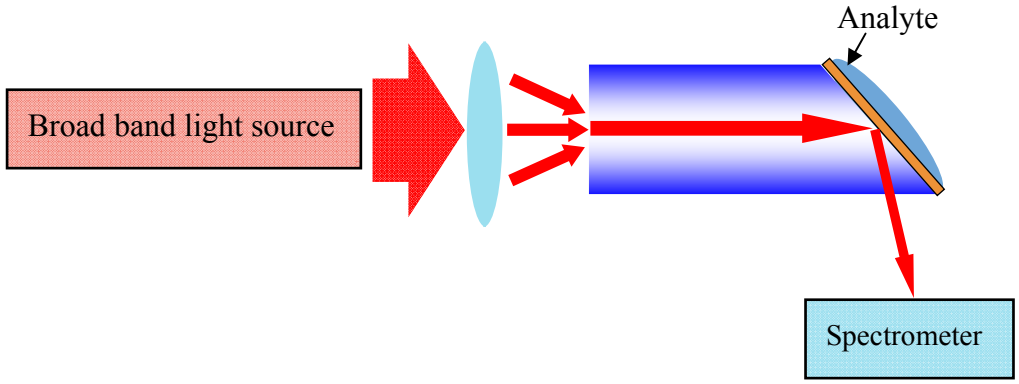

Fig. 5.5 Schematic diagram of the experimental setup for the SPR sensor characterization

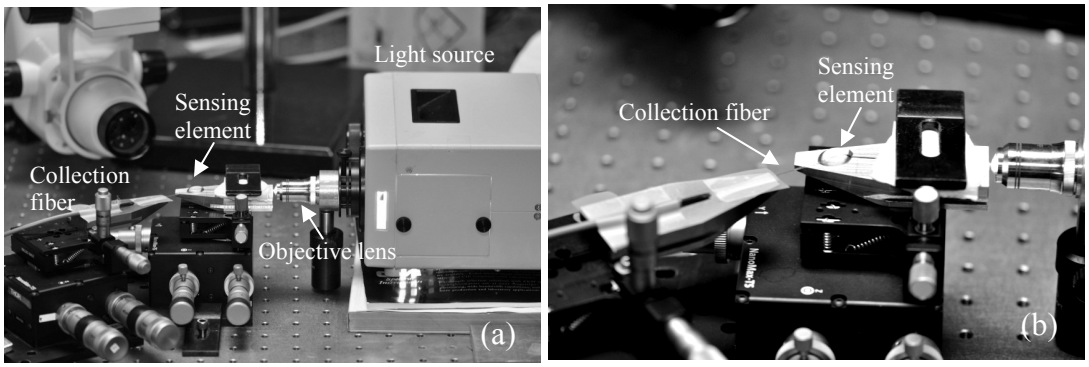

Fig. 5.6 Photographs of the experimental setup for the SPR sensor. (a) General layout and (b) close-up of the fiber alignment.

5.2.2 Experimental results and discussion

Different amounts of DI water are added into the ethanol solution to form the analytes with different refractive indices. The refractive indices of the solutions are calibrated using a digital refractometer (TDR095c, Sino Science & Technology Co., Ltd.). The angled fiber tip is immersed in the analytes and the reflected spectra are collected and shown in Fig. 5.7.

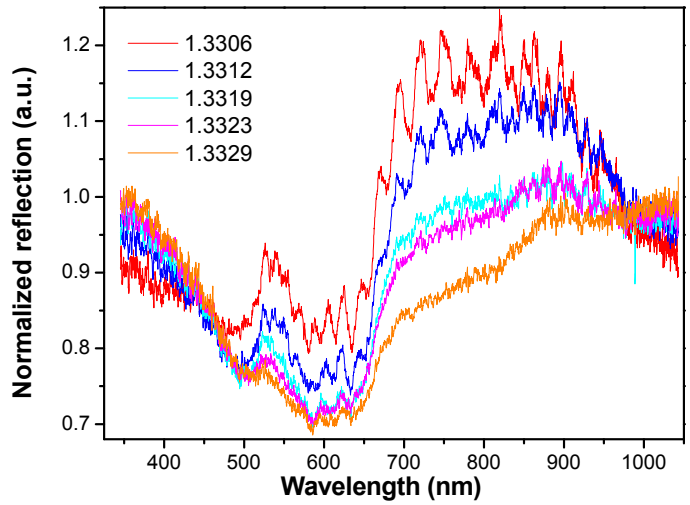

Fig. 5.7 Reflection spectra of the SPR sensor in different analytes.

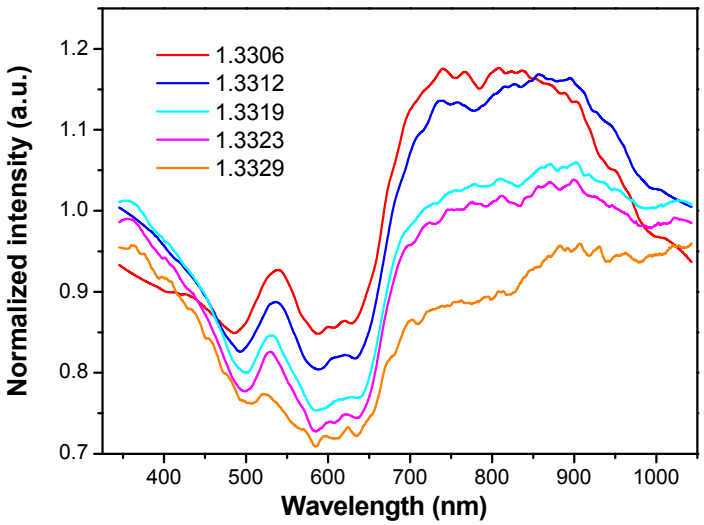

Fig. 5.8 The reflection spectra of angled optical fiber tip in different solutions: experimental data after signal smoothing.

In Fig. 5.7, it can be observed that the minima of normalized intensities decrease gradually from 0.8 to 0.7. After deducing the S-pol. light (only the P-pol.

light is involved in the SPR effect), the equivalent normalized intensity ranges from 0.3 to 0.2, which are lower than the simulation value (0.4). That possible because the detecting probe has relatively large sensing area and big NA, some light from other sources (multi-reflected light in the fiber tip, the light trapped in the liquid drop) are also coupled into the spectrometer together with the signal. Another prominent feature in Fig. 5.7 is there are a series of small peaks appeared in each curve, especially the first two curves from upside. These peaks are roughly periodical, of which the free spectral range (FSR) is about 30 nm, and the corresponding optical length is calculated to be 5 μm. The appearance of these peaks is possibly due to the interference of the multi-reflected light beams in the fiber tip. The curves after smoothing are presented in Fig. 5.8. On both sides of the central dip, as the RI of surrounding dielectric medium increases, the intensity of left side (350-450 nm) gradually increases. On the contrary, the intensity of right side (700-1000 nm) drops, which indicates the red shift of the whole curves when the RI of analyte rises. The bulge (from 500–600 nm) at the bottom of the valley attributes to the normalization error, and it nearly maintains stable during the large valley shift. However, the small valley (centered at 500 nm) isolated by this bulge presents more obvious movement

compared with the broad valley. Although the SPR absorption valley is so broad, its shift could be clearly observed in the track of the small valley.

The shift of SPR absorption valley is plotted in Fig. 5.9 as a function of the refractive indices of anatyles. In simulation, the obtained sensitivity of the SPR is 8,300 nm/RIU (see sub-section 4.1.2). After linear fitting, the sensitivity of the experimental study is 7,650 nm/RIU, which matches well with the theoretical value.

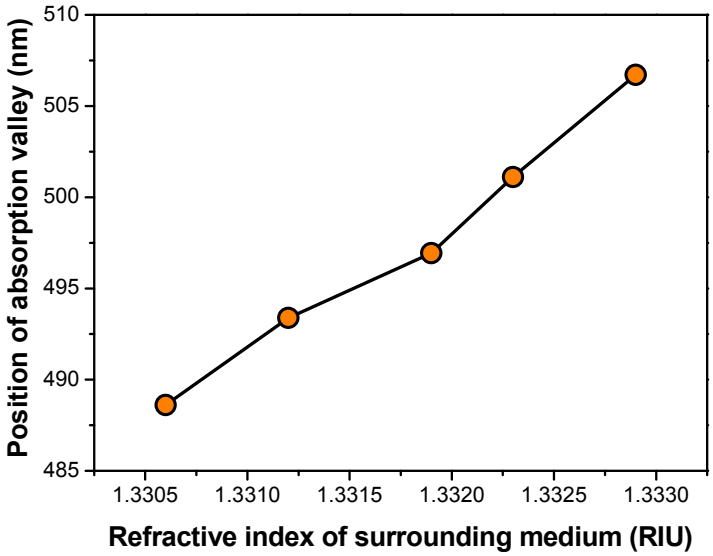

Fig. 5.9 Shift of the SPR valley with the change of RI of the surrounding medium.

In the Fig 5.7, all the curves have a broad absorption valley from 350 to 700 nm, which is broader than the value obtained in the simulation (FWHM 95nm). The reason is analyzed as follows. As the core diameter of the visible band single mode optical fiber (3.2 μm) is so small that the coupled light is too weak, and thus the near

infrared single mode fiber (Corning SMF-28e) is used in the experiment. In fiber optics, the normalized frequency

$$V = \frac{\pi d}{\lambda} NA \tag{5.1}$$

is used to describe the modal dispersion in waveguides, where d is the diameter of the core, λ is the incident wavelength. Since the NAs of these two types of fibers are same (0.13), however, the diameter of core increases from 3.2 to 8.5 μm, the result in normalized frequency V rises from 1.74 to 4.63 (at λ = 750 nm), which means some other modes (LP_{11}, LP_{21}, LP_{02}) propagating along the optical fiber together with the LP_{01} mode. Therefore, the fiber used in the experiment is not exact the single mode fiber if the wavelength of incident light is shorter than its working wavelength. As the core diameter of the used fiber (8.5 μm) is relatively large for the wavelength (600-800 nm), the ray picture is valid within the geometrical-optics approximation. When a ray is incident from a medium of RI n to the outside medium, the possible range of incident angle θ_{in} could be calculated from the value of NA according to Snell's law (Equ.2.11),

$$NA = n \sin \theta_{in} \tag{5.2}$$

In this case, since the NA is 0.13 and n is 1.47, the obtained range of

Incident angle is ± 5 deg. However, the SPR absorption peak will shift with the variation of the incident angle according to Fig. 4.3. Consequently, the absorption valleys overlap with each other and initial broaden the SPR absorption valley. This is exemplified in Fig. 5.10. If the incident angles of light beams range from 68 deg to 72 deg (their intensity distribution is complicated and not stable in open environment, so the beams are assumed to have the equal intensity), the calculated SPR absorption valley is as broad as over 250 nm. Therefore, the width of the SPR valley obtained in the experiment is much broader than the simulation predicted.

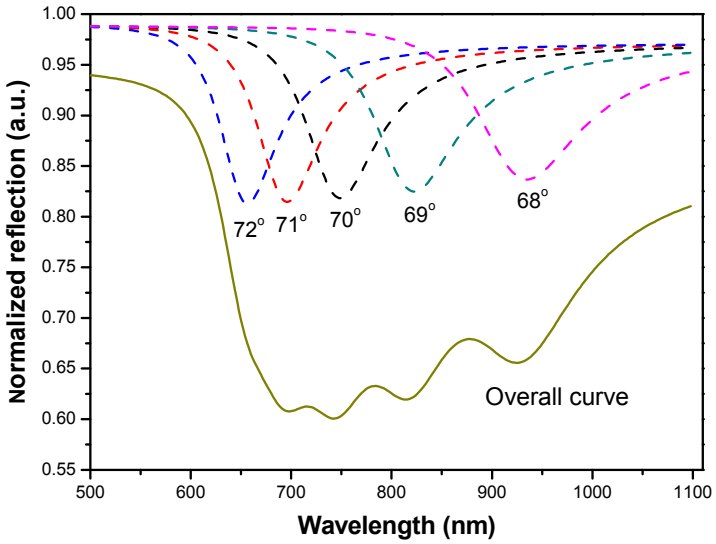

Fig. 5.10 The broaden SPR absorption valley due to the summation of the absorption valleys of various incident angles.

5.3 Refractive index senor based on resonant optical tunneling effect

5.3.1 Experimental setup

For the RI sensor based on the ROTE, to verify the ROTE, the first step is to detect the tunneling signal. For this purpose, two commercial polarization maintaining optical fiber (Thorlabs) are polished in 53 deg before coating with Au. As the real part of RI of Au ranges from 0.2 to 0.6 in near infrared regions [102], all the light beams propagating along the optical fiber are totally reflected at the gold coated surface (NA = 0.13). The gold layer is deposited using the thermal evaporation, of which the deposition rate is 1.5Å/s and the accuracy of monitor is 1Å. Before the Au coating, 2.0 nm Cr is deposited in advance to increase the adhesive to the silica. The thickness of coated Au layer is 18.0 nm. The experimental setup is shown in Fig. 5.11. A tunable laser (Yokogawa, AQ 2100) is used as the light source. The transmission spectrum is measured by an optical spectrum analyzer (Yokogawa, AQ6370B). On the synchronous mode (the laser communicates with the optical spectrum analyzer in real time), the output wavelength of the laser could scan from

1440 to 1650 nm with high power density. Because the ROTE depends on the polarization state of the incident light (see Chapter 3), a polarization controller (Thorlabs) is used to adjust the polarization state of the incident light.

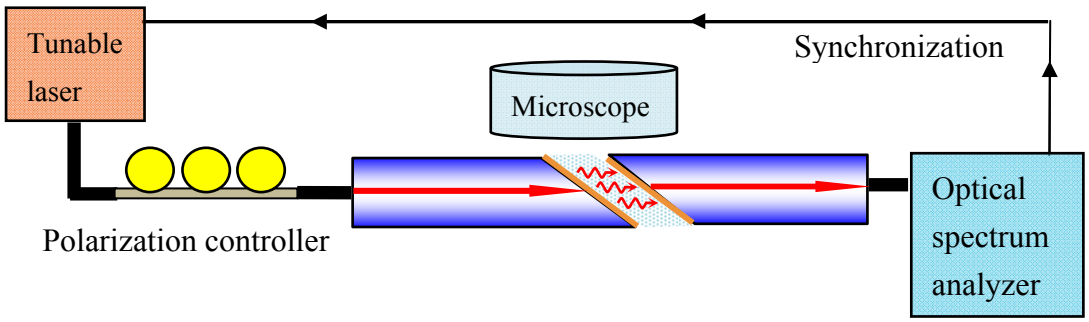

Fig. 5.11 Schematic diagram of the experimental setup for ROTE RI sensor.

Fig. 5.12 presents the photographs of the experimental setup. A pair of sensing probes is fixed on the glass slides by wax and mounted oppositely on a couple of goniometer pairs (Thorlabs, GN2), which could rotate the fiber tip by certain angle. The positions of the two fiber tips could be adjusted by the micropositioners (Melles Griot, 17MAX303). Two mutual perpendicular microscope tubes are utilized to visualize alignment of the fiber tips. By using the pixel ruler, the separation between fiber tips could be measured on the image captured by the microscope. The loading of the analyte (DI water) is achieved by a piece of slim glass slide, which could be lift by micropositioner and immerse the sensing probes.

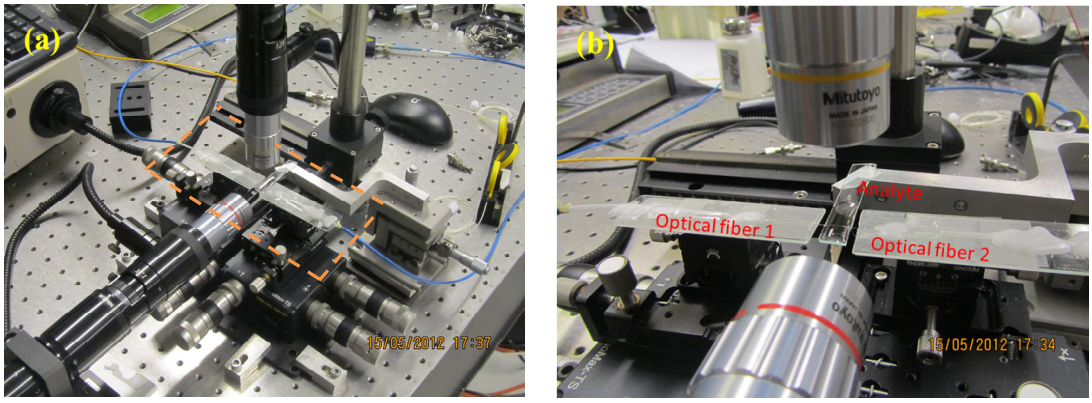

Fig.5.12 Photographs of the experimental setup for the ROTE sensor characterization. (a) General layout and (b) close-up to the sensor.

5.3.2 Experimental results and discussions

Before the experiment, a laser locator (JDSU, λ = 630-670 nm, 1 mW) is applied as the temporary light source to get further high accuracy alignment by measuring the transmitted power. For reference, the photo of the aligned fiber tips is presented in Fig. 5.13. By adjusting the separation of fiber tips, a broad and oblate peak appears in the output spectrum as shown in Fig. 5.14. For the single wavelength, the light source used in the experiment is linearly polarized. However, when the output spectrum covers a range of wavelength, the polarization state keeps changing when the wavelength of emission is scanning. Thus the light source contains both P- and S-polarization state light. However, if take the absorption of the metal layer and

analyte into consideration, the ROTE transmission of P-polarization is 10 times larger than that of S-polarization light (which is not considered in previous simulation, see Fig. 4.14). Therefore, the P-polarized transmission is dominant if the P- and S-polarization states are all involved and have evenly distributed power in the incident light. Fig. 5.14 plots the ROTE transmitted spectrum from theoretical simulation (P-polarized light) and experiment. It can be seen that the peak obtained in the experiment is much broader than the simulation result. The reason for this phenomenon can be explained by the spreading of the incident angles. The number aperture (NA) of the optical fiber is 0.14, thus the corresponding spread of incident angle is ± 5 deg. On the other side, the ROTE peak is very sensitive to the incident angle (see section 3.1). This is the main reason for the broadening of the ROTE transmitted peak. Besides of the spreading of incident angle, the polarization states of incident light also broadens of the ROTE transmission peak. For the small peaks appeared in the profile of the ROTE peak. The FSR of these peaks is 6 nm, which corresponding optical length is 150 μm. Thus these peaks attribute to the FP interferometer formed by the overlapped part of the optical fibers.

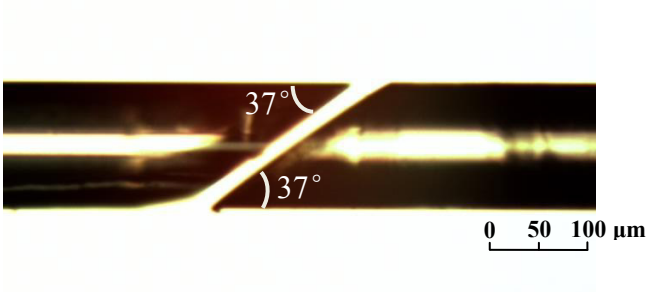

Fig. 5.13 Photo of the aligned angled fibers in characterizing the ROTE sensor.

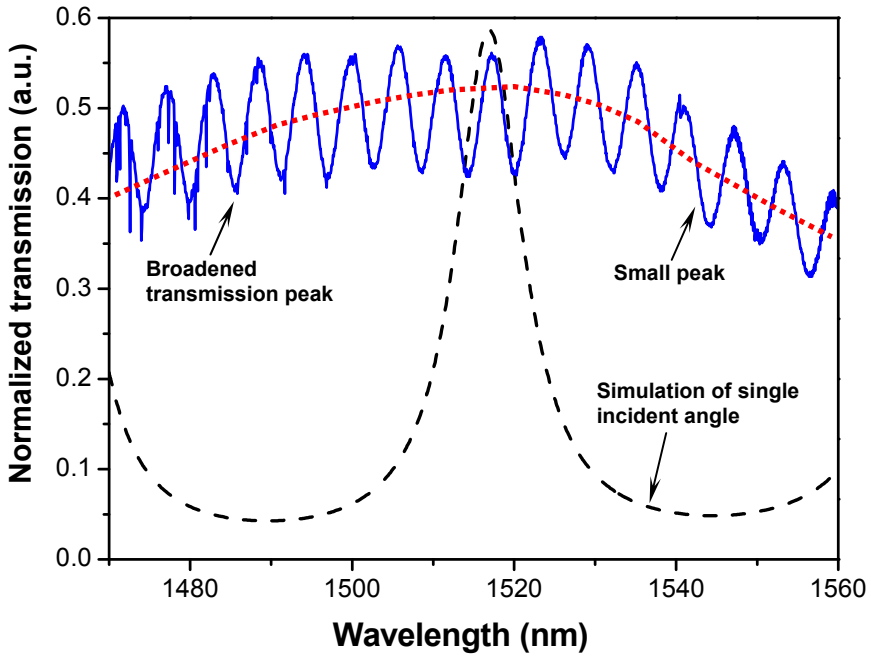

Fig. 5.14 Comparison of the simulated and the measured transmission spectra of the ROTE sensor.

To introduce the RI change, a slim glass slide loaded with the analyte is initially used to immerse the two angled fibers and thus to fill the gap between the fibers with the analyte. However, the surface tension of the analyte would cause a drift of the fiber position and misalign the two fibers slightly, making it difficult to

stabilize and repeat the tests. Theoretically, changing the geometrical separation between fiber tips, causes a variation of the effective optical length of the separation and plays the same role as changing the RI of analyte. For the convenience of testing, the experiments make use of the change of the fiber separation to mimic the change of the RI. The measured transmission spectra at different fiber tip separations are plotted in Fig. 5.15 (a). After signal processing to remove the fast varying components, the spectra are shown in Fig. 5.15 (b). From top to bottom, it can be observed, that the broad ROTE transmitted peak moves gradually towards the larger wavelength as the separation of fiber tips increases. Fig. 5.16 illustrates the shift of ROTE peak as a function of the separation between the fiber tips. The increase of the separation causes a red shift of the ROTE peak, and its linear trend matches well with the theoretical prediction (see Fig. 4.15). By converting the change of the fiber separation into the equivalent change of the RI, the equivalent sensitivity of the sensor is calculated to be 3,500 nm/RIU. Because the aim of this sensor is to verify the ROTE, so the performance of sensor is not put in the first place. The incident angle, the thickness of coated metal layer are all smaller than the design parameters presented in section 4.3.2, so that the sensitivity obtained is much smaller than the

predicted value 81,000 nm/RIU. As investigated in section 3.2, the ROTE is ultra-sensitive to the change of design parameters, so it has great chance to achieve the designed performance after further optimizing the sensor structure.

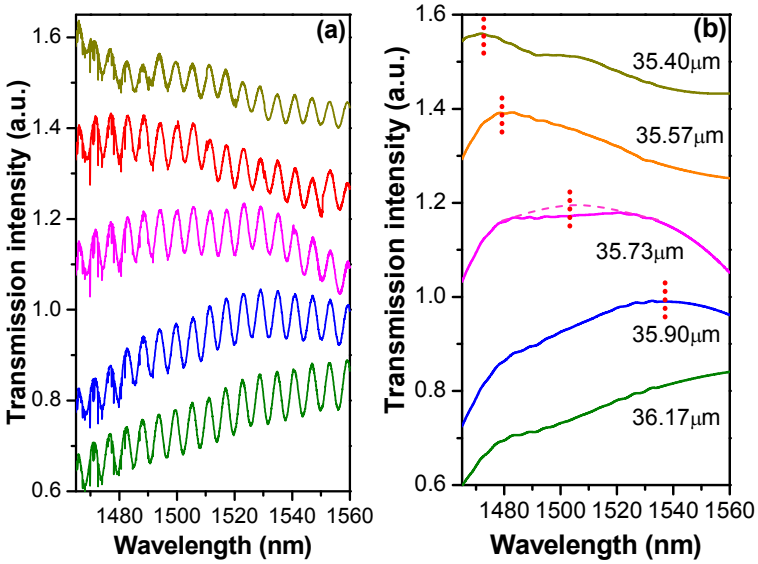

Fig. 5.15 Change of the transmission spectrum with the change of the separation of fiber tips. (a) Experimental data, (b) experimental data after smoothening.

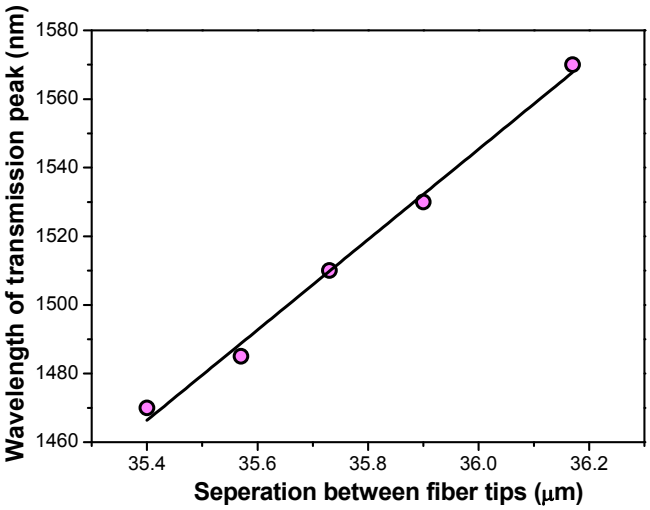

Fig. 5.16 The shift of ROTE peak with respective to the separation of optical fiber tips.

Since the ROTE is related to the polarization state of the incident light, changing the polarization state of incident light is another effective way to verify the ROTE. In the following experiment, the initial polarization state of light source is hard to restrict controlled, thus the polarization state of incident light is varied by adjusting the polarization controller, and other parameters remain unchanged. The transmission spectra with different polarization states of incident light are recorded in Fig. 5.17(a) and (b). Comparing Fig. 5.17 (a) with (b), the appeared peaks have different widths and central wavelengths, and the transmission peak in the (b) drops to only one sixth of the intensity of peak in the (a), This possibly because, the P-polarization state incident light is dominant in the curve of Fig.5.17 (a), however, the S-polarization state incident light is dominant in the curve of Fig.5.17 (b), with sharper peak and lower intensity.

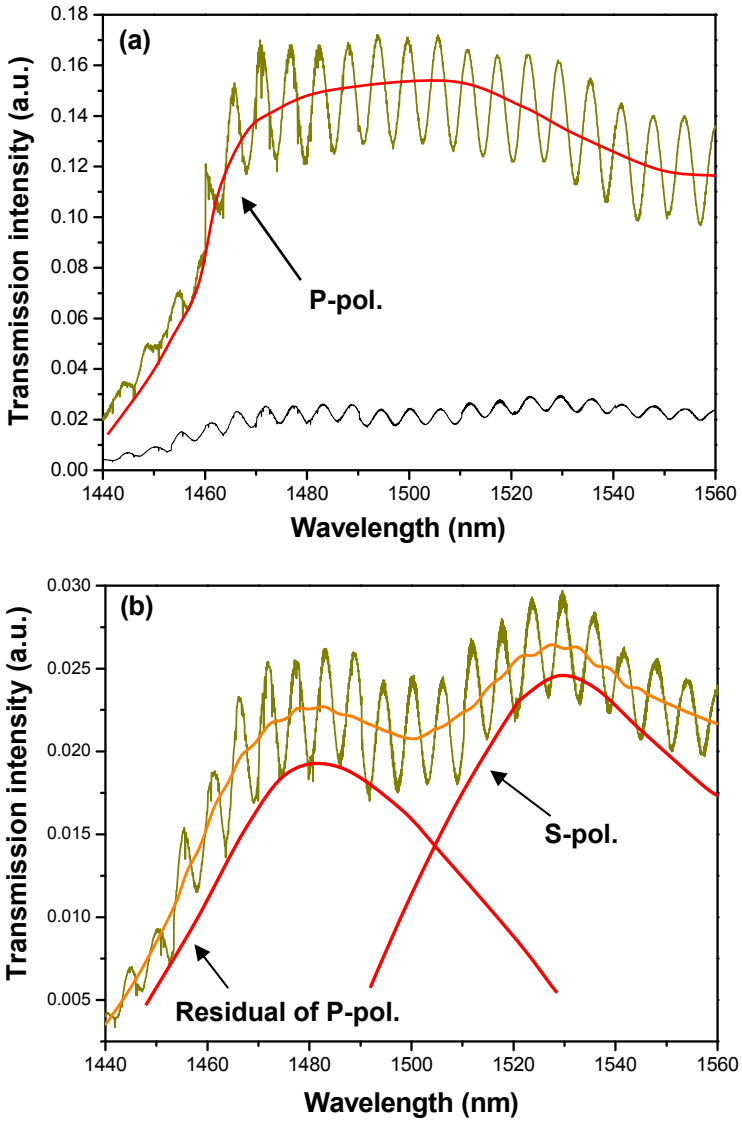

Fig. 5.17 The change of peak shapes and transmitted intensity when the polarization states of incident light changes.

5.4 Summary

This chapter carried out the experimental investigation of the SPR sensor and the ROTE sensor using the angled fibers.

First, the fabrication method of the sensing probe has been presented, covering mainly the procedures of the angled fiber polishing. The measurement of 3-D profilometer, shows that the fluctuation of core part of optical fiber is within 100 nm. For metal coating, the metal deposition methods have also been studied, and their advantages and drawbacks have been discussed for different angled fiber based RI sensors. For instance, the SPR sensor can use the magnetic sputtering, whereas the ROTE sensors have to utilize the thermal evaporation method.

Next, the performance of the angled fiber based SPR sensor has been investigated. This is for verifying the fabrication method and the experimental setup. It seems also to the technical basis for the ROTE sensors in the next step. In the SPR reflection spectrum, a series of absorption valleys have been observed, and the absorption valleys are broaden than the prediction. This attributed to the spreading of the incident angle in the range of ± 5 deg. When the RI of the analytes surrounding the sensing probe is increased, the SPR valley has shown a red shift, and the sensitivity is 7,650 nm/RIU, which agrees well with the theoretical value 8,300 nm/RIU.

Lastly, the ROTE sensors have been developed and characterized. Due to the spreading of the incident angle, the ROTE peak observed in the experiment is broader than the theoretical value. Because the change of analyte would alter the alignment of fiber tips, the fiber tip separation has been varied to obtain the same effect of changing the optical path length for the convenience of experiment. The ROTE transmission peak has shown a red shift as the separation of fiber tips increases. The obtained sensitivity of ROTE sensor (3,500 nm/RIU) is much lower than the predicted value 81,000nm/RIU. However, the incident angle and the thickness of metal layer could be further optimized. In another experimental study, the polarization state of the incident light in varied whereas all the parameters are kept constant. It is observed that the width and intensity of the ROTE peak are changed significantly, which agrees well with the theory. The experimental studies in this chapter have verified the important features of the ROTE in terms of the spectral shift in response to the fiber separation and the polarization state. Although the sensitivity of 3,500 nm/RIU is below the expectation, this is the first experimental effort of ROTE for RI sensing and paves the way to further enhancement and optimization.

Chapter 6 Conclusions and Future Work

6.1 Conclusions

The present research focuses on the theoretical and experimental studies of the ROTE, covering mainly the physical concepts, the sensor designs, the parametric studies and the performance characterization. The main conclusions can be summarized as follows:

(1) In the theoretical study of ROTE, two interpretations-nano-optics interpretation and quantum mechanism interpretation have been presented to build up the physical bases for analytical modeling. In the nano-optics interpretation, transfer matrix model (TMM) has been developed, and based on which, extensive parameter studies have been carried out. It is found that the maximum of transmission intensity can be obtained with a specific set of incident angle, tunneling gap, central slab and incident wavelength. For different polarization states, the characteristics are similar but at different sets of values. If only one of parameters such as the incident angle, the central slab

width and the incident wavelength is changed within a small range (within one period) and other parameters are kept constant, the transmittance would vary dramatically and show a sharp peak; if the parameter varies in a large range (covering several periods), the transmittance peak will distributed periodically. In case of the tunneling gap, the variation of transmittance peak is dependent on the value of central slab width and the transmission peak shifts in different directions for different polarization states.

(2) In the quantum mechanics interpretation, the analogical relationship between the photon tunneling and electron tunneling has been derived based on the single barrier structure, and the analytical results match well with the TMM. The analogical relationship is then extended to the ROTE structure to build up the potential barrier model (PBM). It shows that the transmittance curves from the quantum mechanics interpretation and the nano-optics interpretation have the same period, but experiences a phase difference, which can be compensated by considering the phase shift in the vertical direction.

(3) To build up the technical base of the ROTE and a comparing method for the ROTE, the SPR has been investigated briefly. The working ranges of the

incident angle and the wavelength have been determined using the simulation. To achieve a sharper SPR valley, a new design was proposed using the angled single mode fiber tip instead of the multi-mode fiber taper. Based on the simulation, the sensitivities of the sensor obtained are 2,550 nm/RIU for the gas RI sensing and 8,300 nm/RIU for the liquid RI sensing, respectively.

(4) Two designs of ROTE sensors, microfluidic chip based design and angled optical fiber based design have been proposed. For each design, two independent sensing methods, intensity-based method and spectrum-based method, have been adopted to measure the RI change of liquid analytes. For the microfluidic chip based design, a reduction of the transmission intensity by 42.4 dB can be expected in respect to a RI change of 10^{-3} RIU using the intensity-based method (corresponding to a detection limit of 10^{-7}–10^{-9} RIU), and the sensitivity of sensor could achieve 760 nm/RIU using the spectrum-based method. In case of the angled fiber based design, the transmission will drop -37.5 dB due to the RI change of 10^{-3} RIU (corresponding to a detection limit of 10^{-7} – 10^{-9} RIU), and the sensitivity is expected to reach 81,000 nm/RIU (corresponding to 1.2×10^{-10} RIU in the ideal case). The sensitivities

of both ROTE sensors are about three orders larger than that of the FP etalon in the intensity-based method, and are larger than the FP etalon and comparable with the SPR sensor in the spectrum-based method. However, the ROTE sensors have much higher detectivity than these of the FP etalons and the SPR sensors.

(5) In the experimental study of the angled fiber based SPR sensor, the SPR valley exhibits a red shift when the RI of analyte goes up, and the sensitivity reaches 7,700 nm/RIU, which agrees well with the theoretical value. However, due to the spreading of the incident angle, the SPR absorption valley is much broader than the predicted.

(6) In the experimental study of the ROTE RI sensor, the shift of the transmission spectrum as a function of the fiber separation has been measured. The ROTE transmission peak shows a red shift as the fiber tips move apart. The corresponding sensitivity is 3,500 nm/RIU. Although it is below the expected 81,000 nm/RIU due to the spreading of the incident angle in the end of the optical fiber and the non-ideal film thickness, the performance is already comparable to the SPR sensors and this experimental study paves the way to

further enhancement of the ROTE. To verify the ROTE, the polarization state of incident light has been changed by the polarization controller. The width and intensity of the ROTE peak change significantly, which matches qualitatively the response to the change from the P-polarization to the S-polarization state.

6.2 Future work

The suggestions for the future research are summarized as below.

(1) In the experimental study of the SPR RI sensor, as the core diameter of visible band single mode fiber is very small, it is a great challenge to couple the light into the optical fiber and to get strong reflected signal. Therefore, in the experiment, the near-infrared band single mode fiber is used. However, the larger core size broadens the SPR absorption valley broader. In the future, it is possible to use the visible band single mode fiber as the sensing probe and high-power fiber-coupled light source to obtain sharper SPR valley and thus better sensor performance.

(2) In the experimental study of the ROTE RI sensor, the shift of ROTE peak as a function of the fiber separation has been measured. Although the separation of

the fiber tips has the same effect on the transmittance as the change of the RI of the analyte, the final goal to directly measure the RI of analyte has not been achieved. In the future, a silicon chip with an open micro-channel square microchannel intersecting with a V-groove could be applied in the experiment. The optical fibers into the V-grooves can be pressed for self-alignment, and the fiber tips can be immersed by the analytes running through the microchannel.

(3) In the experimental study of ROTE RI sensor, it has focused on the verification of the ROTE, and thus the sensor is not as sensitive as predicted. In the future, the structure of sensor should be optimized and the sensor with a larger incident angle and a thicker metal layer will be tested.

(4) The SPR is one of the most widely used technologies for biomolecular interaction monitoring. For this application, a layer of chemical ligand could be fixed to the surface of the metal layer, and the biological targets could be transported by a microfluidic system. The binding of the target molecules to the ligands could be indicated by the change in the RI near the metal layer. Thanks to the potential of ultra-high sensitivity, the ROTE sensors could be used to monitor the real-time biomolecular interaction and could provide a

useful tool for biomedical studies. The integration of the optical fiber and the microfluidic system makes it more convenient to the biochemical sensing. This is worth further research efforts in the future.

References

[1] F. Vollmer and S. Arnold, Nature Methods, 5 (2008) 591.

[2] G. Mazarevica, T. Freivalds, and A. Jurka, J. Biomed. Opt.,7 (2002) 244.

[3] V. S. –Y. Lin, K. Motesharei, K-P S. Dancil, M. J. Sailor, and M. R. Ghadiri, Science, 278 (1997) 840.

[4] T.P. Burg, M. Godin, S. M. Knudsen, W. Shen, G. Garlson, J. S. Foster, K. Babcock, and S. R. Manalis, Nature, 446 (2007) 1066.

[5] J. Rheims, J. KÖser, and T. Wriedt, Meas. Sci. Technol., 8 (1997) 601.

[6] J.R. Majer, Talanta, 23 (1976) 747.

[7] F. Samedov, Opt. Laser Technol., 38 (2006) 28.

[8] D. Brennan, P. Lambkin and P. Galvin, Meas. Sci. Technol., 19 (2008) 1.

[9] C.B. Kim and C.B. Su, Meas. Sci. Technol., 15 (2004) 1683.

[10] A. Sabatyan and M.T. Tavassoly, Opt. Laser Technol., 41 (2009) 892.

[11] N. Burggraf, B. Krattiger, A.J. de Mello, N.D. de Rooij and A. Manz, Analyst, 123 (1998) 1443.

[12] D. Markov, D. Begari and D.J. Bornhop, Anal. Chem., 74 (2002) 5438.

[13] W.Z. Song, X.M. Zhang, A.Q. Liu, C.S. Lim, P.H. Yap and Habib Mir M. Hosseini, Appl. Phys. Lett., 89 (2006) 20390.

[14] L.K. Chin, A.Q. Liu, C.S. Lim, C.L. Lin, X. M. Zhang, J. H. Ng, J. Z. Hao, and S. Takahashi, Appl. Phys. Lett., 91 (2007) 243901.

[15] L.K. Chin, A.Q. Liu, C.S. Lim, C.L. Lin, T.C. Ayi and P.H. Yap, Biomicrofluidics, 4 (2010) 0241071.

[16] Z. Tian, S. S.-H. Yam, J. Barnes, W. Bock, P. Greig, J. M. Fraser, H-P. Loock, and R. D. Oleschuk, IEEE Photon. Technol. Lett., 20 (2008) 626.

[17] D. Wu, T. Zhu, M. Deng, D. W. Duan, L. L. Shi, J. Yao, and Y. J. Rao, Appl. Opt., 50 (2011) 1550.

[18] R.G. Heidema and P. V. Lambeck, Sens. Actuators B Chem., 61 (1999) 100.

[19] T. H. Xia, A. P. Zhang, B. Gu, J. J. Zhu, Opt. Commun., 283 (2010) 2136.

[20] Z. Tian, S.S-H. Yam and H-P. Loock, Opt. Lett., 33 (2008) 1105.

[21] J. Villatoro and D. Monzón-Hernández, J. Lightw. Technol., 24 (2006) 1409.

[22] P.H. Tomlins, P. Woolliams, C. Hart, A. Beaumont and M. Tedaldi, Opt. Lett., 33 (2008) 2272.

[23] W. Liang, Y. Huang, Y. Xu, R.K. Lee and A.Yariv, Appl. Phys. Lett., 86 (2005) 151122.

[24] G.M. Rego, J.L. Santos, H.M. Salgado, Opt. Commun., 259 (2006) 598.

[25] T. Allsop, R. Reeves, D. J. Webb, I. Bennion, and R. Neal, Rev. Sci. Instrum., 73 (2002) 1704.

[26] B. Lee, S. Roh and J. Park, Opt. Fiber Technol., 15 (2009) 209.

[27] J. Homola, Anal Bioanal Chem, 377 (2003) 528.

[28] D. Monzón-Hernández, J. Villatoro, Sens. Actuators B, 115 (2006) 227.

[29] J. Homola, R. Slavik, J. Ctyroky, Opt. Lett., 22 (1997) 1403.

[30] R. Slavik, J. Homola, J. Ctyroky, E. Brynda, Sens. Actuators B, 74 (2001) 106.

[31] Y.-J. Chang, Y.-C. Chen, H.-L. Kuo, P.-K. Wei, J. Biomed. Opt., 11 (2006) 014032.

[32] M.-H. Chiu, C.-H. Shih, M.-H. Chi, Sens. Actuators B, 123 (2007) 1120.

[33] T. Allsop, R. Neal, S. Rehman, D.J. Webb, D. Mapps, I. Bennion, J. Opt. Soc. Am. B, 25 (2008) 481.

[34] J.-L. Tang, S.-F. Cheng, W.-T. Hsu, T.-Y. Chiang, L.-K. Chau, Sens.

Actuators B, 119 (2006) 105.

[35] G. Nemova, R. Kashyap, Opt. Lett., 31 (2006) 2118.

[36] C. Ronot-Trioli, A. Trouillet, C. Veillas, H. Gagnaire, Sens. Actuators A, 54 (1996) 589.

[37] A.K. Sharma, B.D. Gupta, Nanotechnol., 17 (2006) 124.

[38] R.K. Verma, A.K. Sharma, B.D. Gupta, Opt. Commun. 281 (2008) 1486.

[39] H. Suzuki, M. Sugimoto, Y. Matsui, J. Kondoh, Sens. Actuators B, 132 (2008) 26.

[40] M. Piliarik, J. Homola, Z. Manikova, J. Ctyroky, Sens. Actuators B, 90 (2003) 236.

[41] N. M. Hanumegowda, C. J. Stica, B. C. Patel, I. M. White, and X. Fan, Appl. Phys. Lett., 87 (2005) 201107.

[42] F. Xu and G. Brambilla, Appl. Phys. Lett., 92 (2008) 101126.

[43] H. J. Moon, G. W. Park, S. B. Lee, K. An, and J. H. Lee, Appl. Phys. Lett., 84 (2004) 4547.

[44] V. Zamora, A. Díez, M. V. Andrés, and B. Gimeno, Opt. Express, 15 (2007) 12011.

[45] Y. -F. Xiao, V. Gaddam, and L. Yang, Opt. Express, 16 (2008) 12538.

[46] M. L. Gorodetsky, A. A. Savchenkov, and V. S. Ilchenko, Opt. Lett., 21 (1996) 453.

[47] F. Luan, J. C. Knight, P. St.J. Russell, S. Campbell, D. Xiao, D. T. Reid, B. J. Mangan, D. P. Williams, and P. J. Roberts, Opt. Express, 12 (2004) 835.

[48] D. G. Ouzounov, F. R. Ahmad, D. Muller, N. Venkataraman, M. T. Gallagher, M. G. Thomas, J. Silcox, K. W. Koch, and A. L. Gaeta, Science, 301 (2003) 1702.

[49] P. St. J. Russell, E. Marin, A. Diez, and A. B. Movchan, Opt. Express, 11 (2003) 2555.

[50] S. Guenneau and A. B. Movchan, Arch. Ration. Mech. Anal., 171 (2004) 129.

[51] V. Laude, A. Khelif, S. Benchabane, M. Wilm, T. Sylvestre, B. Kibler, A. Mussot, J. M. Dudley, and H. Maillotte, Phys. Rev. B, Condens. Matter, 71 (2005) 045107.

[52] P. J. Roberts, F. Couny, H. Sabert, B. J. Mangan, D. P. Williams,L. Farr, M. W. Mason, A. Tomlinson, T. A. Birks, J. C. Knight, and P. St.J. Russell, Opt. Express, 13 (2005) 136.

[53] K. Nakajima, K. Hogari, J. Zhou, K. Tajima, and I. Sankawa, IEEE Photon. Technol. Lett., 15 (2003) 1737.

[54] L. Michaille, C. R. Bennett, D. M. Taylor, T. J. Shepherd, J. Broeng, H. R. Simonsen, and A. Petersson, Opt. Lett., 30 (2005) 1668.

[55] W. J. Wadsworth, R. M. Percival, G. Bouwmans, J. C. Knight, T. A. Birks, T. D. Hedley, and P. St.J. Russell, IEEE Photon. Technol. Lett., 16 (2004) 843.

[56] J. Limpert, T. Schreiber, S. Nolte, H. Zellmer, A. Tünnermann, R. Iliew, F. Lederer, J. Broeng, G. Vienne, A. Petersson, and C. Jakobsen, Opt. Express, 11 (2003) 818.

[57] W. N. MacPherson, M. J. Gander, R. McBride, J. D. C. Jones, P.M. Blanchardb, J.G. Burnettb, A.H. Greenawayb, B. Manganc, T.A. Birksc, J.C. Knightc, P.St.J. Russell, Opt. Commun., 193 (2001) 97.

[58] P. M. Blanchard, J. G. Burnett, A. H. Greenaway, B. J. Mangan, T. A. Birks, J. C. Knight, and P. St.J. Russell, Opt. Commun., 193 (2001) 97.

[59] M. T. Myaing, J. Y. Ye, T. B. Norris, T. Thomas, J. R. Baker, W. J. Wadsworth, G. Bouwmans, J. C. Knight, and P. St.J. Russell, Opt. Lett., 28

(2003) 1224.

[60] P. M. Blanchard, J. G. Burnett, G. R. G. Erry, A. H. Greenaway, P. Harrison, B. J. Mangan, J. C. Knight, P. St.J. Russell, M. J. Gander, R. McBride, and J. D. C. Jones, Smart Mater. Struct., 9 (2000) 132.

[61] P. St. J. Russell, J. Lightw. Technol., 24 (2006) 4729.

[62] J. Sun and C. C. Chan, Sens. Actuators B, 128 (2007) 46.

[63] L. Rindorf and O. Bang, Opt. Lett., 33 (2008) 563.

[64] D. K. C. Wu, B. T. Kuhlmey and B. J. Eggleton, Opt. Lett., 34 (2009) 322.

[65] C. Monat, P. Domachuk, and B. J. Eggleton, Nature Photon, 1 (2007) 106.

[66] Y.L. Hoo, W. Jin, L. Xiao, J. Ju, and H.L. Ho, Sens. Actuators B, 136 (2009) 26.

[67] L. J. Kauppinen, H. J. W. M. Hoekstra, and R. M. de Ridder, Sens. Actuators B, 139 (2009) 194.

[68] G. J. Veldhuis and P. V. Lambeck, Appl. Phys. Lett., 71 (1997) 2895.

[69] B. You, J.-Y. Lu, C.-P. Yu, T.-A. Liu, and J.-L. Peng, Opt. Express, 20 (2012) 5858.

[70] Y. Wang and X. G. Huang, Opt. Laser. Technol., 42 (2010) 1312.

[71] L. M. Brekhovskikh, Wave in layered media, Chapter 3, Academic, New York, 1960.

[72] K. T. V. Garttan, A. W. Palmer, and D. P. S. Saini, J. Lightw. Technol., LT-3 (1985) 1130.

[73] W. B. Spillman, Jr., and D. H. McMahon, Appl. Opt., 19 (1980) 113.

[74] J. Kameoka and H. G. Craighead, Sens. Actuators B, 77 (2001) 632.

[75] E. Yablonovitch, Phys. Rev. Lett., 58 (1987) 2059.

[76] S. John, Phys. Rev. Lett., 58 (1987) 2486.

[77] E. Yablonovitch, J. Opt. Soc. Am. B, 10 (1993) 283.

[78] W. M. Zhu, T. Zhong, A. Q. Liu, X. M. Zhang and M. Yu, Appl. Phys. Lett., 91 (2007) 261106.

[79] S. Zhu, A. W. Yu, D. Hawley, and R. Roy, Am. J. Phys., 54 (1986) 601.

[80] R. Y. Chiao, P.G. Kwiat, and A. M. Steinberg, Physica B, 175 (1991) 257.

[81] A. M. Steinberg and R. Y. Chiao, Phys. Rev. A, 49 (1994) 3283.

[82] B. Lee and W. Lee, J. Opt. Soc. Am. B, 14 (1996) 777.

[83] M. Deutsch and J. E. Golub, Phys. Rev. A, 53 (1996) 434.

[84] I. R. Hooper, T. W. Preist, and J. R. Sambles, Phys. Rev. Lett., 97 (2006)

053902.

[85] P. Yeh, Optical waves in layered media, Chapter 5, Wiley, New York, 1988.

[86] P. Yeh, A. Yariv, and C. –S. Hong, J. Opt. Soc. Am., 67 (1977) 423.

[87] P. Yeh, J. Opt. Soc. Am. A, 2 (1985) 568.

[88] J. M. Vigoureux and F. Baïda, Opt. Commun., 101 (1993) 297.

[89] S. Hayashi, H. Kurokawa and H. Oga, Opt. Rev., 6 (1999) 204.

[90] N. Yamamoto, K. Akahane and Shin-Ichirou Gozu, Appl. Phys. Lett., 87 (2005) 231119.

[91] N. Yamamoto and N. Ohtani, Jpn. J. Appl. Phys., 43 (2004) 1393.

[92] J. Li, A. Q. Liu, X. M. Zhang, and T. Zhong, Appl. Phys. Lett., 88 (2006) 243501.

[93] T. Zhong, X. M. Zhang, A. Q. Liu, J. Li, C. Lu, and D. Y. Tang, IEEE J. Sel. Top. Quant., 12 (2007) 348.

[94] W. M. Zhu, T. Zhong, A. Q. Liu, X. M. Zhang and M. Yu, Appl. Phys. Lett., 91 (2007) 261106.

[95] W. M. Zhu, X. M. Zhang, A. Q. Liu, H. Cai, T. Jonathan, and T. Bourouina, Appl. Phys. Lett., 92 (2008) 251101.

[96] Sh. A. Furman and A.V. Tikhonravov, Basics of Optics of Multilayer Systems, Chapter 1, World Scientific Publishing Co Pte Ltd, Singapore, 1996.

[97] T. K. Gaylord, G. N. Henderso, and E. N. Glytsis, J. Opt. Soc. Am. B, 10(1993) 333.

[98] A. Q. Jian, X. M. Zhang, W. M. Zhu, and Miao Yu, Biomicrofluidics, 4 (2010) 043008.

[99] A. Q. Jian, X. M. Zhang, W. M. Zhu, and A. Q. Liu, Sens. Actuators A, 169 (2011) 347.

[100] T. E. Hartman, J. Appl. Phys., 33 (1962) 3427.

[101] D. Bartolo, G. Degre, P. Nghe, and V. Studer, Lab Chip, 8 (2008) 274.

[102] E. D. Palik, Handbook of Optical Constants of Solids, Chapter 3, Academic Press, Boston, 1985.